

# **The Effects of Sulphide Oxidation on the Preservation of Hydrothermal Chimneys from the Endeavour Segment, Juan de Fuca Ridge**

By © Euripidis Alexander Papanicolaou

A Thesis submitted to the School of Graduate Studies

In partial fulfilment of the requirements for the degree of

**Master of Science, Department of Earth Sciences**

Memorial University of Newfoundland

**October 2020**

St. John's, Newfoundland and Labrador

## Abstract

Inactive seafloor hydrothermal vents on the seafloor are continuously exposed to oxygen-rich seawater and subjected to oxidative processes. These processes result in mineral breakdown, structural instability, and eventual collapse of the vents. Rates and timing of these processes are largely unconstrained, despite laboratory experiments using combinations of oxidizing agents, environmental conditions, and reacting mineral species. Here, sixteen sulfide- and oxyhydr(oxide)-rich samples were collected from inactive hydrothermal vents along the Endeavour Segment of the Juan de Fuca Ridge to document natural oxidative processes. Petrographic observations indicate preferential oxidation of low rest potential minerals due to the formation of galvanic cells between polymetallic sulfide minerals. Under ambient seawater conditions, sulphide-rich samples demonstrate dual production of iron oxide and oxyhydroxide precipitates produced by abiotic oxidation of sulfide minerals or microbially-mediated precipitation of Fe-oxyhydr(oxide) on exterior surfaces. The results suggest that dissolution of minerals hosting valuable metals like Cu and Zn will occur more rapidly than Fe-bearing minerals. Radiometric  $^{226}\text{Ra}/\text{Ba}$  ages were determined from a subset of the collected samples. This subset increases in age with distance from the current spreading center, supporting previous results indicating progressive aging of hydrothermal vents from the axial spreading center.

## **General Summary**

Hot water springs on the ocean floor form chimney-like structures composed primarily of minerals made of sulfur and metals such as iron, copper and zinc. Over time, these vents stop discharging fluids, and the minerals oxidize (i.e. rust) or dissolve back into seawater, and the chimneys eventually collapse. This thesis examines the chemical and mineralogical changes that occur, and the rates of these changes. Rock samples from extinct vents were collected from the Endeavour Vent Field, a cluster of active and inactive vents on a volcanic ridge off the west coast of British Columbia. We note that specific combinations of sulphide minerals will increase the rate of dissolution of Cu and Zn bearing minerals, potentially reducing the viability of old inactive deposits as an economic resource. We also note that mineralogical changes are driven by both chemical and microbial processes. These results have implications for understanding the long-term preservation potential for these chimneys.

## **Acknowledgments**

Thank you to John Jamieson for designing and guiding me throughout this project and for your abundant wealth of both critical feedback and patience. I would also like to thank my committee member, Steve Piercy for his critiques and comments during the writing and editorial processes. Thank you to the Canada Research Chair Program, Research & Development Corporation of Newfoundland (now InnovateNL), and Fisheries and Oceans Canada for their financial support. I would like to thank the crew and scientists aboard the John P. Tully in summer 2016 for their essential work collecting the samples for this project from the seafloor; Wanda Aylward for her support and instruction in using the scanning electron microscope. Finally, thank you to my lab group members Ben Peterkin and Dennis Sanchez-Mora; my friends from all over; and my family for their patience and continual support throughout the thesis.

# Table of Contents

<u>Abstract</u> .....	ii
<u>General Summary</u> .....	iii
<u>Acknowledgments</u> .....	iv
<u>List of Tables</u> .....	vii
<u>List of Figures</u> .....	viii
<u>List of Symbols and Abbreviations</u> .....	xiv
<u>List of Appendices</u> .....	xvi
<b><u>Chapter 1 Introduction and purpose of study</u></b> .....	17
<u>1.1 Introduction:</u> .....	17
<u>1.1.1 Thesis Objectives</u> .....	17
<u>1.1.2 Regional Geology and Tectonic Setting</u> .....	18
<u>1.1.3 Discovery and Exploration of the Endeavour vent fields</u> .....	21
<u>1.2 Seafloor Hydrothermal Systems</u> .....	22
<u>1.2.1 Hydrothermal Fluid Circulation</u> .....	22
<u>1.2.2 Seafloor Massive Sulphide Deposits</u> .....	24
<u>1.2.3 Oxidation of Sulphides</u> .....	31
<u>1.2.4 Galvanic Interactions between Sulphide Minerals</u> .....	39
<u>1.3 Methods</u> .....	42
<u>1.3.1 Sampling</u> .....	42
<u>1.3.2 Petrography</u> .....	43
<u>1.3.3 Scanning Electron Microscope (SEM)</u> .....	44
<u>1.3.4 Whole Rock Geochemistry</u> .....	44

1.3.5 Geochronology .....	44
1.4 Co-Authorship Statement .....	45
1.5 Thesis Presentation .....	46
1.6 References .....	47
<b>Chapter 2</b> .....	58
2.1 Abstract .....	58
2.2 Introduction .....	59
2.3 Geological Setting .....	63
2.4 Methodology .....	64
2.4.1 Petrography .....	66
2.4.2 Scanning Electron Microscopy (SEM) .....	67
2.4.3 Whole Rock Geochemistry .....	67
2.4.4 Geochronology .....	67
2.5 Results .....	68
2.5.1 Mineralogy of samples collected from extinct chimneys .....	68
2.5.2 Scanning Electron Microscope- Energy Dispersive Spectroscopy Analysis ....	80
2.5.3 Major and Trace Element Litho geochemistry .....	81
2.5.4 Geochronology .....	85
2.6 Discussion .....	87
2.6.1 Oxidation of sulphide minerals .....	87
2.6.2 Seafloor Massive Sulphide Site Characteristics use as a Vector for Time .....	98
2.6.3 Implications of New <sup>226</sup> Ra/Ba Age Data for the Endeavour Segment .....	100
2.7 Conclusions .....	103
2.8 References .....	105

<b><u>Chapter 3 Summary</u></b> .....	117
<u>3.1 Findings</u> .....	117
<u>3.2 Recommendations</u> .....	118
<u>3.3 Future work</u> .....	118
<u>3.4 Conclusions</u> .....	119
<u>3.5 References</u> .....	121
<b><u>Appendices</u></b> .....	122
<u>Appendix 1 – Sample Site Coordinate List</u> .....	122
<u>Appendix 2 – Whole Rock Geochemical Results</u> .....	124
<u>Appendix 3 – Detailed Petrographic Results</u> .....	127
<u>Appendix 4 – Hand sample Descriptions</u> .....	155

## List of Tables

Table 1.1 Resting potential of various sulphide minerals commonly found within seafloor massive sulphide deposits. Modified from Mehta and Murr, 1983. ....	41
Table 2.1: Rest potential of various sulphide minerals commonly found within seafloor massive sulphide deposits. ....	62
Table 2.2: Modal mineral abundances present in sampled seafloor massive sulphide divided by sample location. *** = An abundant mineral content, ** = minor mineral content, * = trace mineral content. ....	74
Table 2.3: Whole rock geochemical analysis of seafloor samples collected throughout the Endeavour vent fields. ....	84
Table 2.4: $^{226}\text{Ra}/\text{Ba}$ Geochronology results of massive sulphide samples collected from inactive locations along the Endeavour Segment. ....	86
Table 2.5: Mineral abundance variation of massive sulphide samples grouped by primary and secondary mineral phases and compared by estimated ages. ....	90
Table 2.6: Ages and estimated ages of seafloor massive sulphide samples. ....	92

## List of Figures

- Figure 1.1: Regional Map of the west coast of Canada and the United States, with the Juan de Fuca Ridge and its component segments. Bathymetric map from <http://www.geomapapp.org>; (Ryan *et al.*, 2009). ..... 19
- Figure 1.2: One-meter resolution bathymetric map created in ArcGIS of the Endeavour Segment (bathymetric data courtesy of MBARI) with major vent fields marked with black stars (Beaulieu, 2015). Plotted samples marked with coloured triangles were studied as part of this research. .... 20
- Figure 1.3: Schematic representation of a high temperature “black smoker” chimney, and low-temperature diffuse venting massive sulphide mound, showing mineralogical zonation due to variation in temperature and pH associated with seawater mixing. (Modified from Tivey, 2007) ..... 25
- Figure 1.4: Experimental run demonstrating variations in the mineral assemblage of the Cu-Fe-S system with temperature constant at 200°C and pH ranging from 0.8 to 7. Modified from Reed and Palandri, 2006. .... 26
- Figure 1.5: Experimental constant cooling run of a 1m NaCl fluid with a constant composition and  $\Delta\text{pH}$  of 0.5 less than neutral. The fluid was initially saturated with sphalerite, chalcopyrite, galena, pyrite, magnetite, and electrum ( $X_{\text{Au}} = 0.69$ ) and was cooled from 300 to 25°C. (Modified from Reed and Palandri, 2006). ..... 27
- Figure 1.6: Breakdown of the three steps pyrite undergoes for electrochemical oxidative dissolution (Rimstidt & Vaughan, 2003). ..... 35
- Figure 1.7: Possible phase relations at 25 °C (atom %) of Cu-Fe-S system, after Vaughan and Craig (1997, their Figs. 8.17 and 8.21) (Modified by Hannington, 1993). Arrow indicates the progressive removal of Fe and Cu due to late stage weathering of sulphide ore. Abbreviations: al = anilite; bn = bornite; cb = cubanite; cc = chalcocite; cp = chalcopyrite; cv = covellite; di = digenite; dj = djurleite; fk = fukuchilite; gr = greigite; hc = haycockite; hpo = hexagonal po; id = idaite; mh = mooihoekite; mpo = monoclinic po = pyrrhotite; py = pyrite; sm = smythite; ta = talnakhite; tr = troilite. 38

Figure 1.8: Comparison of Cu dissolution rates between isolated Chalcopyrite ( $\text{CuFeS}_2$ ), galvanically coupled chalcopyrite-pyrite ( $\text{CuFeS}_2\text{-FeS}_2$ ), and chalcopyrite-pyrite-sphalerite ( $\text{CuFeS}_2\text{-FeS}_2\text{-ZnS}$ ). Comparison with the presence and absence of (a) T. ferrooxidans at 30°C (b) thermophilic bacteria at 55°C. T.F. = T. ferrooxidans, TH = thermophilic bacteria. ....43

Figure 2.1: Autonomous undersea vehicle (AUV) 1-meter resolution bathymetric map of the Endeavour Segment. Indicated samples were collected for the purpose of this study. Data courtesy of the Monetary Bay Research Institute (MBARI). Inset: Regional tectonic setting of the Juan de Fuca Ridge along the west coast of North America.....65

Figure 2.2: Autonomous undersea vehicle (AUV) 1-meter resolution bathymetric data 3-dimensional render of the seafloor north of Main Endeavour Field. Purple flags indicate dive R1940 sample collection transect. Data courtesy of the Monetary Bay Research Institute (MBARI). Inset: Depths of sample sites measured in meters below sea level (mbsl) and the relative distance between sites measured in meters and indicated by purple marker lines. ....66

Figure 2.3: a) Zero age sample collection site north of the Endeavour vent fields; b) inactive chimney located along the western valley wall north of Main Endeavour with an estimated age of 3,000 years; c) inactive chimney located at the western rim of the axial estimated age of 5,800 years; d) inactive chimney located outside the Endeavour axial valley, sampled by Jamieson et al. (2013) using ROV Doc Ricketts, and dated to be ~5,850 years old; e) inactive chimney from the eastern half-graben with significant Fe-Mn coating, and dated to be 5,750 years old.....73

Figure 2.4: Characteristic sulphide mineral assemblages observed in plane and cross-polarized reflected light photomicrographs; (A) Euhedral-subhedral cubic pyrite (py) crystal aggregates commonly containing blebs of sphalerite (sp), with subhedral massive chalcopyrite (ccp); (B) Massive pyrite with subsequent colloform pyrite growth and further late-stage massive pyrite; (C) Framboidal pyrite (py) with later stage massive pyrite growth; (D) Exterior margin of massive sulphide composed of massive pyrite (py) with a void space lining of marcasite (mrc), and exterior surface

composed of goethite (gth) and Fe-oxyhydr(oxide); (E) Dendritic marcasite (mrc) with minor colloform banding, Fe-oxide replacement at crystal edges by goethite (gth); (F) Massive chalcopyrite (ccp) with intermixed solid solution of isocubanite (isoc) altering into secondary covellite (cv) (dark blue)/chalcocite(cct) (light blue) and oxidized into Fe- oxyhydr(oxide) precipitates.....76

Figure. 2.5: Plain and cross-polarized photomicrographs of characteristic Fe-oxides and oxyhydroxides. (A) Goethite (gth) replacing massive anhedral chalcopyrite (ccp) with interstitial pyrite (py) and sphalerite (sp); (B) Plain polarized reflected light photomicrograph of euhedral cubic pyrite partially replaced by goethite (grey-blue) from both at grain rims, along grain boundaries, and internally forming atoll textures; (C-D) Plan and cross-polarized reflected light photomicrographs of goethite replacement of pyrite in addition to Fe-oxyhydr(oxide) (FeO) precipitate forming along the remnant sulphide grain boundaries; (E) Plain-polarized reflected light micrograph of dendritic marcasite (mrc) partially replaced by goethite with late-stage Fe-Mn crust precipitation (Fe-Mn ox) formed along exterior boundary; (F) Fe-oxyhydr(oxide) concretions acting as nucleation points for intermingling bands of abiotic Fe-oxyhydr(oxide) and Mn oxide (MnO).....78

Figure 2.6: (A) Millimetre scale image of Fe-oxyhydr(oxide) on the exterior surface of a massive sulphide sample; (B) Plain polarized transmitted light photomicrograph of a pristine bacterial generated goethite (gth) filament network at the outer surface of a heavily oxidized sample; (C) Scanning electron microscope backscatter image of goethite Fe-oxyhydroxide filaments and concretions with abiotic Fe-oxyhydr(oxide) precipitates (FeO); (D) Scanning electron microscope image of amorphous Fe-oxide precipitate developing along the surface of goethite filament structures. ....80

Figure 2.7: Graphic representation of the average mineral composition for the two sample sub-sets, based on petrographic observations. Group 1 is relatively enriched in Al, Ba, Mg, Mn, Ni, Pb, Si, Sm, U, and V, whereas group 2 is relatively enriched in Co, Cu, Fe, and Mo. Mineral abbreviations: Anh = Anhydrite, Mn Oxide = Manganese Oxide mineral, Py = Pyrite, Mc = Marcasite, Fe-Oxyhydr(oxide) = Iron-Oxyhydr(oxide), Brt = Barite, Si = Amorphous Silica, Ccp = Chalcopyrite, Cv =

Covellite, Cct = Chalcocite, Isoc = Isocubanite, Atac = Atacamite, and Sp = Sphalerite. ....80

Figure 2.8: SEM-EDS analysis of massive sulphide, oxide, and oxyhydroxide samples from the Endeavour Segment (A) Massive pyrite with sphalerite (sph) bleb intergrowths. Oxide dissolution/oxidation (gth) of pyrite (py) forming "atoll" textures; (B) Alteration of chalcopyrite (ccp) into covellite (cv) (loss of Fe, S; increase in Cu) to Cu-containing Fe-oxyhydr(oxide); (C) Pyrite replacement by goethite, in addition to replacement of the Fe<sup>3+</sup> cation Al<sup>3+</sup> forming AlO(OH); (D) Iron-oxyhydr(oxide) of microbial origin, with composition ranging from massive to porous and branching, in addition to a defined band of manganese oxide (MnO); (E) Iron-oxyhydr(oxide) exterior of a massive sulphide sample with an isolated chalcopyrite grain with high relief FeO boundary; (F) Detailed perspective of Fe-oxyhydr(oxide) armouring isolated chalcopyrite grain, confirming that it is compositionally similar but texturally varied from surrounding oxides. ....82

Figure 2.9: Box and whisker plot of contrasting seawater sourced elemental abundances between heavily oxidized (group 1 - red symbols) and typical seafloor massive sulphide (group 2 – purple symbols) samples. Boxes represent the middle 50% of data, box shading indicates median value, and the whiskers represent 1.5 times the interquartile range. ....85

Figure 2.10: Age distribution of hydrothermal sulphide samples from the Endeavour Segment, divided into active vent field samples (top) and inactive vent site samples (bottom). Samples introduced in this study are represented by star markers and previous data collected by Jamieson et al. (2013) are represented by circle markers. Of the four new samples introduced to this dataset one sample is a new “zero-age” sample. Two samples collected from inactive structures within active venting fields are relatively young (<3,000 years), and one sample, collected from an inactive sulphide mound on the eastern half-graben, is relatively old (~5,500 years). Figure modified from Jamieson et al. (2013). ....86

Figure 2.11: Plot of  $^{226}\text{Ra}/\text{Ba}$  activity vs. Ba wt.% from collected “zero-age” samples from the Endeavour Segment. Samples collected by Jamieson et al. (2013) are denoted by blue markers; this study denoted with an orange marker. A correlation line is plotted for all existing data maintaining an  $r^2$  value of 0.9965 denoting a statistically significant correlation. ....87

Figure 2.12: Plain polarized reflected light photomicrograph of the progressive galvanic interactions between polymetallic sulphide minerals. A) Cathodically protected euhedral cubic pyrite (py) galvanically reacting with intergrown subhedral chalcopyrite (ccp) forming secondary covellite (cv) along crystal fractures, and boundaries, B) progressed galvanic interaction of cathodically protected cubic euhedral pyrite and anodic preferentially oxidized subhedral chalcopyrite, and anhedral sphalerite (sp). C) Extensive preferential oxidative dissolution of chalcopyrite releasing copper ions into seawater precipitating covellite from pyrite with sphalerite blebs. D) Nearly complete oxidative dissolution and replacement of chalcopyrite into covellite no longer cathodically protecting pyrite and forming cubic remnant cubic goethite (gth) pseudomorphs.....94

Figure 2.13: Galvanic interaction variation photomicrographs under reflected light. A. Intermingling euhedral massive pyrite (py) with chalcopyrite (ccp), B. Euhedral pyrite crystal aggregate in proximity but not in contact with subhedral chalcopyrite-sphalerite (sp), C. Anhedral chalcopyrite rimmed by banded marcasite (mrc) and massive subhedral pyrite, D. Late stage oxidation of chalcopyrite resulting in the release of copper ions into solution allowing for the secondary precipitation of covellite (cv) and the iron released into solution is oxidized to form an amorphous Fe-oxide. Pyrite replacement by goethite (gth) as it is not galvanically protected by another metal sulphide, E. massive chalcopyrite, isocubanite (isoc) solid solution with oxidation along chalcopyrite grain boundaries forming covellite and chalcocite (cct). No visible galvanic interactions are occurring between isocubanite and chalcopyrite, F. euhedral pyrite interacting with intermixed chalcopyrite forming secondary covellite and chalcocite. ....96

Figure 2.14: Orifice and massive sulphide wall perspectives of surface manganese precipitation, sulphide oxidation, and the original massive sulphide. Colour coordinated polylines indicate respective boundaries. .... 101

Figure 2.15: Map of samples from this and other studies with associated  $^{226}\text{Ra}/\text{Ba}$  age data (Jamieson et al., 2013). This figure shows the relative distances of the collected samples from a graphical estimate of the location of the spreading axis. Figure inset is defined by the cross-section A to A' providing depth of sample collection in meters below sea level (mbsl). All sample points follow the same colour trend defined in the legend..... 102

Figure 2.16 Biplot of age versus distance from the graphical estimation of the spreading center axis for all collected seafloor massive sulphide deposit samples with associated  $^{226}\text{Ra}/\text{Ba}$  barite dates. The trend line defined for the data series has a positive trend with a slope of  $\sim 6$  years/m ( $r^2 = 0.63$ ). ..... 103

## List of Symbols and Abbreviations

Anh	Anhydrite
AMD	Acid Mine Drainage
Atac	Atacamite
AUV	Autonomous Undersea Vehicle
Brt	Barite
Cct	Chalcocite
Ccp	Chalcopyrite
Cv	Covellite
CCGS	Canadian Coast Guard Ship
DFO	Department of Fisheries and Oceans
EDS	Electron Dispersive Spectroscopy
Eh	Measurement of the electrical potential
$fO_2$	Oxygen fugacity
$fS_2$	Sulphur fugacity
GIS	Geographic Information Systems
Gth	Goethite
ICP-MS	Inductively Coupled Plasma Mass Spectrometry
INAA	Instrumental Neutron Activation Analysis
Isoc	Isocubanite
JDF	Juan de Fuca
NEPTUNE	Northeast Pacific Time-Series Underwater Experiment
Mrc	Marcasite
MBARI	Monterey Bay Aquarium Research Institute
Mbsl	Meters below sea level
MEF	Main Endeavour Field
mol	Measurement of the molar concentration of a chemical compound

ONC	Ocean Networks Canada
Py	Pyrite
Po	Pyrrhotite
REE	Rare Earth Elements
ROV	Remotely Operated Vehicle
SEM	Scanning Electron Microscope
SMS	Seafloor Massive Sulphide
SOSUS	United States Navy's Sound Surveillance System
Sp	Sphalerite
XPS	X-ray photoelectron spectroscopy

## **List of Appendices**

<b>Appendix 1</b> – Sample Site Coordinate List .....	120
<b>Appendix 2</b> – Whole Rock Geochemical Results .....	122
<b>Appendix 3</b> – Detailed Petrographic Results .....	125
<b>Appendix 4</b> – Handsample Descriptions .....	153

# **Chapter 1 Introduction and purpose of study**

## **1.1 Introduction:**

Seafloor massive sulphide (SMS) deposits are modern analogues of ancient volcanogenic massive sulphide (VMS) deposits (Hannington et al., 2005). These products of hydrothermal venting at the seafloor result from the release of hot, reducing, metal-rich, and sulfate-poor hydrothermal fluids, which mix with cold, sulphate-rich, alkaline seawater to precipitate sulphide minerals that accumulate to form SMS deposits (Tivey, 1995). The thermal buoyancy of vented fluids results in a hydrothermal plume that may rise several tens to hundreds of meters in the water column and disseminate micron-scale metal-rich sulphide and oxide particles (Feely et al., 1990). Sulphide-rich structures forming on the seafloor develop in accordance with both the environmental conditions they are subject to, including magmatic and seismic activity, and the composition and temperature of the ascending vent fluids (Tivey, 2007). Upon termination of hydrothermal activity, ambient seawater infiltrates the vent deposits and oxidizes the sulphide minerals. Oxidation and dissolution of sulphide minerals and dissolution of anhydrite create structural instability, and eventual collapse of vents, forming talus piles on the seafloor (Hannington et al., 1995 ;Jamieson et al., 2013). The goals of this project are to investigate the physical, chemical, and biological processes that result in the degradation of hydrothermal vents once venting ceases, and the rates at which these processes occur. Understanding these processes will provide insight into the mineralogical evolution of extinct deposits and the factors that control the preservation potential of base metal-rich sulphide mineral deposits on the seafloor. The goals of this project will be accomplished by investigating a suite of extinct hydrothermal vents of various ages and documenting the changes in mineralogical and textural features of the deposits.

### **1.1.1 Thesis Objectives**

This study aims to describe the morphological, mineralogical, and textural changes associated with aging and degradation of extinct hydrothermal vents on the seafloor. These observations will support previous experimental work on sulfide oxidation in ambient seawater conditions (Lowson, 1982; Janecky & Seyfried, 1984; Bierens de Haan, 1991; Rimstidt &

Vaughan, 2003; Fallon et al., 2017; Knight et al., 2017). Data for this study are derived from observations recorded directly at the seafloor, hand-samples, and thin-sections. This work is further supplemented by whole rock geochemical data and analysis by scanning electron microscopy/energy dispersive spectroscopy (SEM/EDS). This study provides new data on the fate of extinct hydrothermal systems and in situ evidence of chemical interactions that take place on the seafloor.

### **1.1.2 Regional Geology and Tectonic Setting**

The Endeavour vent fields occur along the Endeavour Segment of the Juan de Fuca Ridge (Fig. 1.1). The Juan de Fuca Ridge, located off the west coast of Canada and the United States, is spreading at a full spreading rate of ~6 cm/year, separating the Pacific Plate from the Juan de Fuca plate (Goldstein et al., 1991). The 90 km Endeavour Segment is one of seven ridge segments that make up the Juan de Fuca Ridge and is bound by the Cobb Segment to the south and by Middle/West Valley to the north (Kelley et al., 2012; Clague et al., 2014). The Endeavour Segment has a full spreading rate of 5.2 cm/year, defined by seafloor magnetism and U-Th dating of basalt (Riddihough, 1984; Goldstein et al., 1991). The central region of the segment reaches a minimum depth of 2,050 meters below sea level (mbsl) with the overall depth increasing to more than 2,700 m below sea level to both the north and south of the central topographic high (Jamieson et al., 2013).

Along the spreading axis of the Endeavour Segment is an axial valley that ranges from 1.2 to 1.7 km wide at the upper valley rim and 400 to 1,200 m wide on the axial valley floor (Clague et al., 2014). The central axial graben walls range from 130 to 180 m high. The axial valley is shallowest near to the center of the segment (Clague et al., 2014). It represents the neovolcanic zone of the ridge segment and is made up of a series of faulted terraces which are interpreted to be a normally faulted half grabens that form stepwise valley walls. The axial valley floor consists of basaltic flows, collapsed lava lakes, and fissures (Jamieson et al., 2013).

Two primary hypotheses describe the development of the axial rift zone of the Endeavour Segment. These two contrasting hypotheses focus on the central axial valley graben and whether alternating episodes of magmatism and tectonism drive the axial valley development or whether the axial valley formed as a result of crustal buoyancy associated with the magmatic evolution of

the ridge (Kappel & Ryan, 1986; Carbotte et al., 2006; Jamieson et al., 2013; Clague et al., 2014). Kappel and Ryan (1986) provide evidence for episodic rifting and volcanism, based on a series of symmetric, ridge-parallel ridges and valleys that represent alternating episodes of tectonic extension and volcanic activity. Carbotte et al. (2006) used data from seismic surveys to locate and determine the depth of the axial magma chamber beneath the central axial graben and correlate these features to crustal thermal buoyancy. Further details of the axial magma chamber have been subsequently established by Van Ark and others (2007), who imaged a thin magma sill 2.2 to 3.3 km beneath the seafloor.

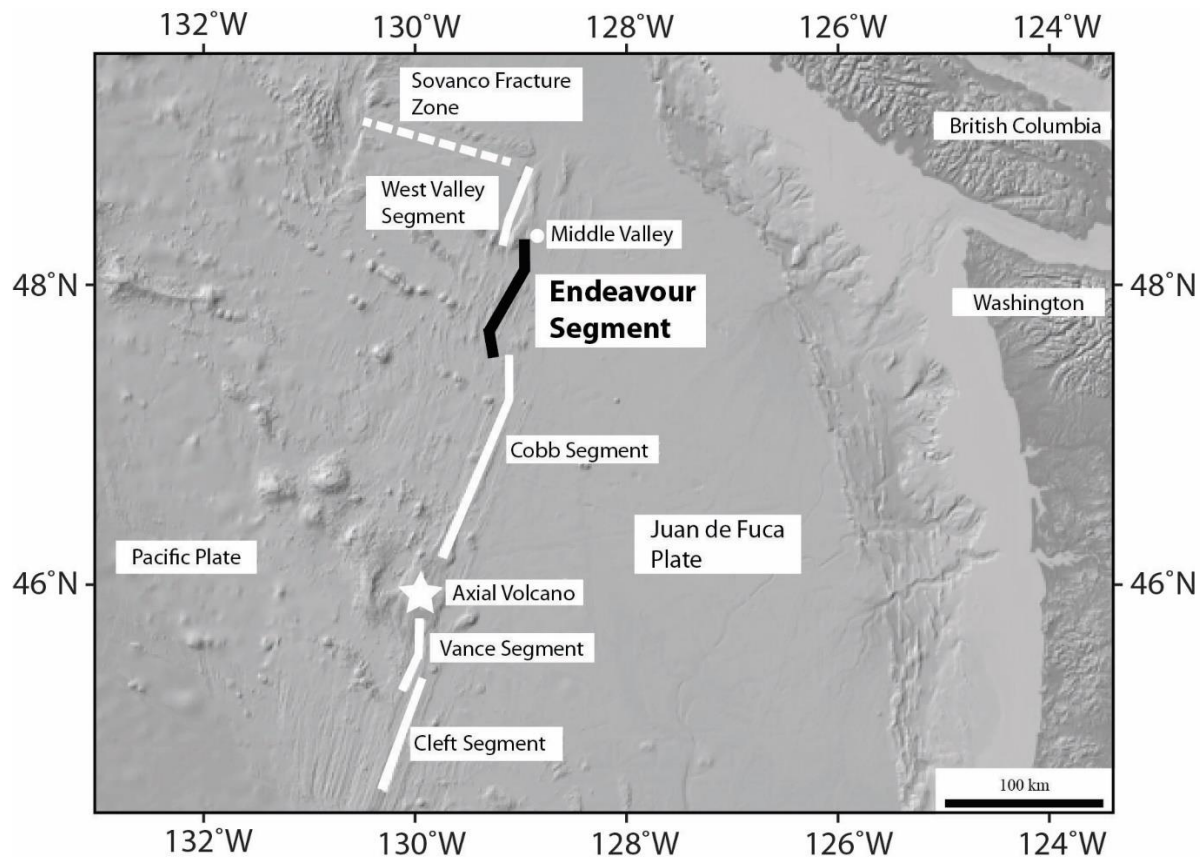


Figure 1.1: Regional Map of the west coast of Canada and the United States, with the Juan de Fuca Ridge and its component segments. Bathymetric map from <http://www.geomapapp.org>; (Ryan et al., 2009).

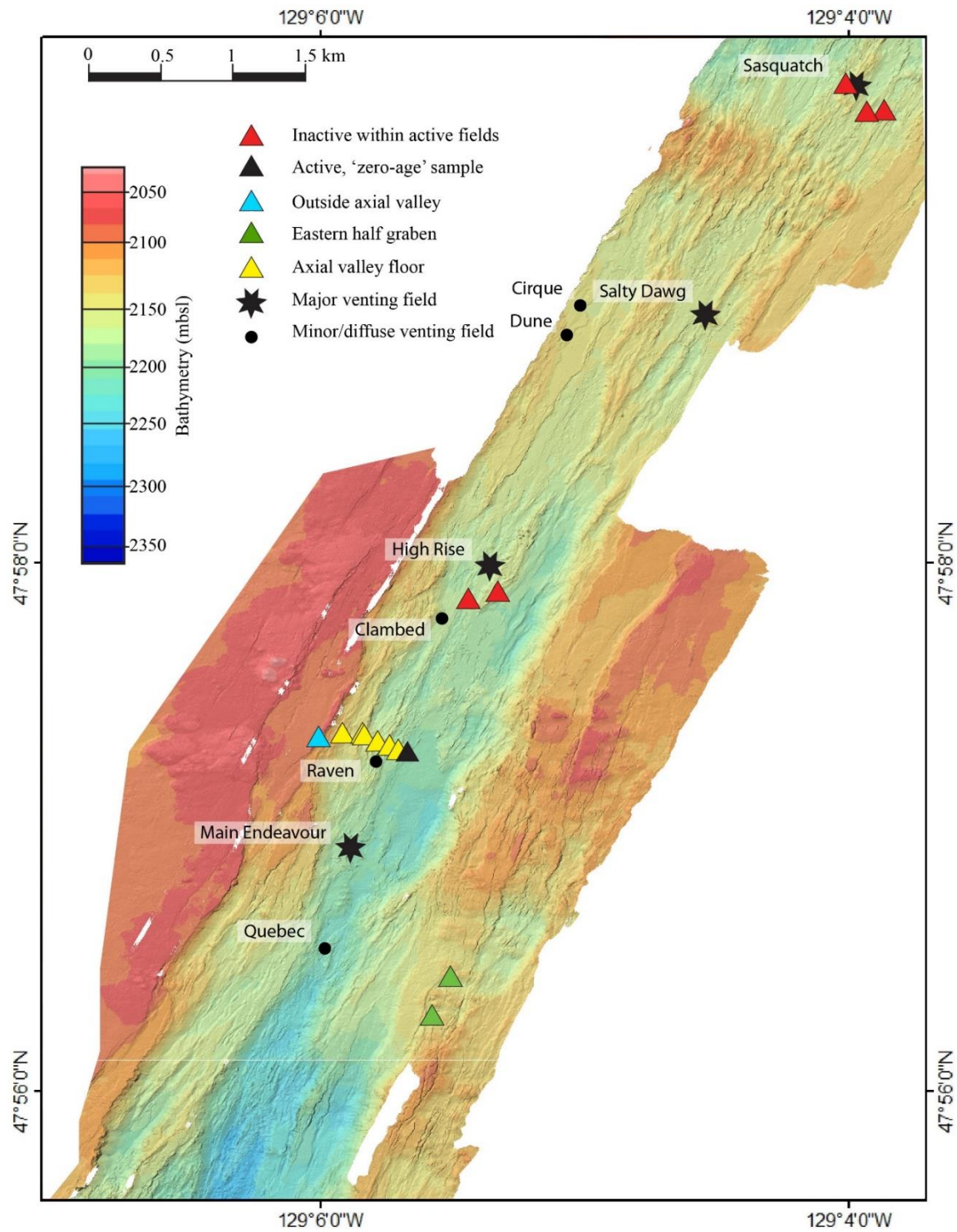


Figure 1.2: One-meter resolution bathymetric map created in ArcGIS of the Endeavour Segment (bathymetric data courtesy of MBARI) with major vent fields marked with black stars (*Beaulieu, 2015*). Plotted samples marked with coloured triangles were studied as part of this research.

Along the Endeavour Segment, there are five major active high-temperature vent fields (from south to north): Mothra, Main Endeavour, High Rise, Salty Dawg, and Sasquatch (Figure 1.2), with two smaller fields: Raven and Clam Bed (Kelley et al., 2012). The regions between both major and minor vent fields contain low-temperature (<150°C) diffusely venting sites, such as Cirque, Dune, and Quebec, and an abundance of extinct chimneys that were identified via high-resolution bathymetry (Fig. 1.2; Kelley et al., 2012; Jamieson et al., 2014). Based on geochronological studies of hydrothermal barite, active venting along the axial valley has been occurring for a minimum of 3,000 years (Jamieson et al., 2013).

### **1.1.3 Discovery and Exploration of the Endeavour vent fields**

The Endeavour vent fields were designated as Canada's first Marine Protected Area in March of 2003, and the ridge segment was also one of three Integrated Study Sites as a part of the U.S. National Science Foundation's Ridge 2000 program (Kelley et al., 2012). The initial discovery of the Main Endeavour Field (MEF), in 1982, occurred when two blocks of massive sulphide material were dredged from the seafloor (Tivey & Delaney, 1986; Stakes & Moore, 1991). This discovery led to researchers returning in 1983, and with the use of ship multibeam bathymetry, side-scan sonar, and a deep-towed camera, they identified morphologic variations along the spreading center, and generated a bathymetric map of the Endeavour Segment at a 50-meter contour interval scale (Karsten et al., 1986). In 1984, the Endeavour segment was first explored using the *Alvin* submersible to survey the area further and collect additional samples (Tivey & Delaney, 1986). Progressively over the next two decades, more and more of the Endeavour Segment was explored. High Rise, Salty Dawg, Mothra, Sasquatch, and Stockwork fields were discovered in 1988 (Robigou et al., 1993; Kelley et al., 2001; Kellogg & McDuff, 2010;), 1995 (Glickson et al., 2006), 1996 (Delaney et al., 1992; Kelley et al., 2001), 2000 (Glickson et al., 2006), and 2005 (Kelley et al., 2012), respectively. Recently, interpretation of volcanic and hydrothermal features within the axial valley, based on meter-resolution autonomous underwater vehicle (AUV) mapping, combined with radiogenic  $^{226}\text{Ra}/\text{Ba}$  dating of hydrothermal deposits, have refined our understanding of the magmatic and tectonic evolution of the axial valley (Jamieson et al., 2013; Clague et al., 2014). Currently, the Northeast Pacific Time-Series Underwater Experiment (NEPTUNE Canada), developed by Ocean Networks Canada (ONC) and

installed in 2009, provides continuous temperature, salinity, direction and intensity of water currents, dissolved oxygen, pH and pCO<sub>2</sub> data. Seismic monitoring, using the United States Navy's Sound Surveillance System (SOSUS), have allowed researchers like Johnson and others (2000) to document a 1999 seismic disturbance which induced a segment-wide increase in both vent fluid temperature and output for at least 80 days.

## **1.2 Seafloor Hydrothermal Systems**

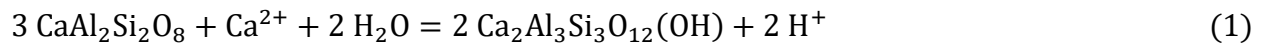
Seafloor massive sulphide deposits form on and below the seafloor at sites of high-temperature hydrothermal venting (Baker & Massoth, 1987). The minerals that form these deposits can contain elevated concentrations of valuable elements such as Cu, Zn, Au and Ag, and SMS deposits are increasingly being targeted by national governments and mineral exploration companies as an alternative source to land-based mines for these metals (Hannington et al., 2010). Much of the research associated with the formation of SMS deposits has focused on actively forming deposits, as opposed to extinct hydrothermal systems on the seafloor (Delaney et al., 1992a). This scientific bias is largely due to the ease with which active systems can be detected relative to inactive systems. Hydrothermal plumes, which form in the water column above active vents, are a convenient marker of active venting on the seafloor. The fine, rapidly precipitated sulphide particles rise hundreds of meters into the water column, slowing their ascent only once they reach a state of neutral buoyancy create broad thermal, chemical, and physical anomalies in the water column (Baker & German, 2004; Jamieson & Petersen, 2015). The scientific bias towards active vents is further compounded by the wide scientific audience for colonies of unique organisms that are endemic to active vents, and because active vents provide an opportunity for direct sampling of hydrothermal fluids (Kelley et al., 2012). As a result, little is known about inactive or extinct hydrothermal systems.

### **1.2.1 Hydrothermal Fluid Circulation**

The high-temperature hydrothermal vent fluids that form SMS deposits are commonly sulphur and metal-rich, reduced, and acidic (Alt, 1995). This fluid composition is the result of the evolution of cold seawater infiltrating into the oceanic crust, where it is progressively heated to temperatures of ~400°C, and reacts with the surrounding country rock in a series of alteration

reactions (Alt, 1995). The circulation of seawater within oceanic crust is responsible for ~30% of oceanic crustal cooling, and the fluid-rock reactions result in an important sink for dissolved Mg, and a source of Fe, Mn, Li, Rb, and Cs for seawater (Von Damm et al., 1985). Hydrothermal circulation of seawater requires two major components: a heat source such as a magma body, and a permeable medium such as faults or fissures within the oceanic crust (Tivey, 2007).

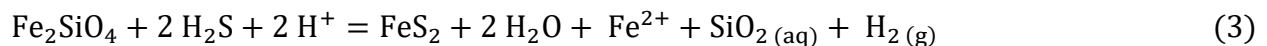
The evolution of hydrothermal fluid from a starting seawater composition is the result of a series of water-rock interactions that occur at progressively higher temperatures as the fluid circulates within oceanic crust. As seawater enters the seafloor at the recharge zone and descends into the crust, and temperatures reach 40-60°C, basaltic glass, olivine, and plagioclase react to produce Fe-rich micas and clay minerals such as smectite and chlorite (Alt, 1995). As fluids progress deeper within the crust temperatures continue to increase and magnesium is quantitatively removed from the fluids due to clay precipitation. Above 150°C, much of the Ca and SO<sub>4</sub> are removed from the fluid due to precipitation of anhydrite (CaSO<sub>4</sub>) and smectite minerals [e.g., Ca<sub>2</sub>Al<sub>3</sub>Si<sub>3</sub>O<sub>12</sub>(OH)], which simultaneously increases fluid acidity (Eq. 1; Seyfried & Janecky, 1985):



Iron-bearing minerals such as olivine, pyroxene, and pyrrhotite react with the hot, acidic fluids, producing H<sub>2</sub>, thereby further enhancing the reducing potential of the fluid (Eq. 2 and 3) (Seyfried & Janecky, 1985).



Pyrrhotite



Fayalite

Pyrite

In the high-temperature reaction zone, fluids reach temperatures of around 400°C, pH can range from 2 - 5.9 (Table 3 - Von Dam, 1995), and the fluids, now anoxic, alkali-rich, and Mg-poor can readily leach sulphur and metals such as Cu, Fe, Mn and Zn from the rock (Alt, 1995).

### 1.2.2 Seafloor Massive Sulphide Deposits

Hydrothermal fluids can form several different types of vent-related features on the seafloor, depending on the fluid's composition, temperature, discharge rate, presence of sediments, and the permeability of the host rock at the venting site (Alt, 1995; Tivey, 2007). Hydrothermal fluids that ascend through a more permeable substrate will begin mixing with seawater at a greater depth, resulting in clear (non-smokey), lower temperature (e.g.,  $< \sim 100^{\circ}\text{C}$ ) fluids that are commonly associated with diffuse venting (Bemis et al., 2012). The clear appearance of diffuse fluids, relative to black smoke associated with high-temperature ( $> 300^{\circ}\text{C}$ ) fluids, is due to the precipitation of metal sulphides at the location of initial fluid mixing at depth (Hannington et al., 1995). Diffuse vents have been observed to form at sulphide mounds, fractured lava flows, and at the bases of high-temperature black smoker chimneys (Bemis et al., 2012).

High-temperature vents on the seafloor are often readily recognizable as prominent spires discharging black smoke composed of sulphide mineral particles. Over time, the permeable fluid pathways that control the high-temperature circulation may be sealed by the precipitation of hydrothermal minerals, resulting in the development of more focused fluid pathways (Hannington et al., 1995). Endmember hydrothermal fluids venting onto the seafloor mix rapidly with seawater, causing precipitation of fine-grained sulphate and sulphide minerals, and amorphous silica that together result in the construction of vent edifices (Tivey, 1995). Development of a chimney structure further isolates the upflowing hydrothermal fluids and creates a temperature and pH gradient between hydrothermal fluids and seawater within the chimney walls (Hannington et al., 1995). Isolation of the hydrothermal fluids allows for the development of temperature- and pH-dependent mineral assemblages within a chimney, commonly represented by an inner high-temperature suite of Cu-Fe sulphides (e.g., chalcopyrite, pyrrhotite, and isocubanite) and anhydrite, and a lower temperature mineral suite composed of pyrite, sphalerite, and barite, and amorphous silica (Fig. 1.3; Haymon & Kastner, 1981; Tivey, 1995). Precipitation of the lower temperature minerals into wall pore spaces progressively increases the density and insulative capacity of a chimney. Once established, low permeability chimneys replace early stage mineral precipitates with new sulphide minerals (Tivey, 1995).

The exterior walls of mature chimneys are composed of anhydrite, barite, silica, and lower-temperature sulphide minerals (Hannington et al., 1995). However, due to the retrograde solubility

of anhydrite in ambient seawater conditions, chimneys with an abundance of anhydrite will become unstable and eventually collapse when no longer exposed to high temperature fluids (Hannington et al., 1995).

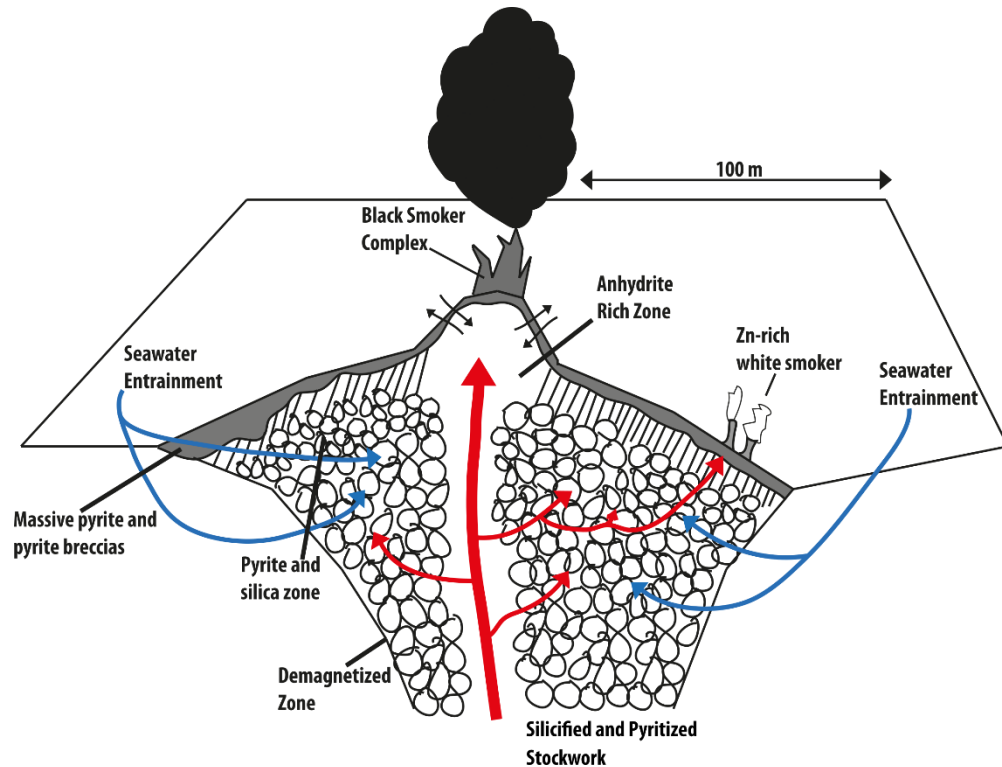


Figure 1.3: Schematic representation of a high temperature “black smoker” chimney, and low-temperature diffuse venting massive sulphide mound, showing mineralogical zonation due to variation in temperature and pH associated with seawater mixing. (Modified from Tivey, 2007)

### 1.2.2.1 Formation Conditions for Hydrothermal Minerals

The first stage of chimney development is thought to be linked to discrete volcanic activity, displacing large volumes of hydrothermal fluids, initiating widespread diffuse venting on the seafloor (Butterfield et al., 1994). This is followed by sealing and focusing of low-temperature venting, eventually forming more focused, higher temperature fluid discharge sites (Hannington et al., 1995). The precipitation of minerals at or near the seafloor result from changes in the physicochemical properties of the hydrothermal fluid that result from mixing with seawater or conductive cooling proximal to the seafloor. In an experimental setting, Reed and Palandri (2006) investigated the effects of changes in pH, temperature, and redox conditions on the precipitation

of common sulphide minerals found in hydrothermal vents. The Cu-Fe-(Zn,Pb)-S system was assessed with a change in pH from acidic (pH 0.8) to neutral (pH 7) conditions while maintaining a constant temperature of 200°C. The mineralization sequence covellite, chalcocite, bornite, chalcopyrite, galena, sphalerite, with pyrite accompanying all other minerals was observed (Fig. 1.4). Factors affecting the pH of hydrothermal fluids thus have a critical role in the mineral assemblage formed on the seafloor. The pH of circulating fluids can be influenced by several factors such as magmatic volatile input (e.g., SO<sub>2</sub>), wall-rock interactions, the presence of carbonate, or the presence of organic matter (Ohmoto, 1996; Tivey, 2007).

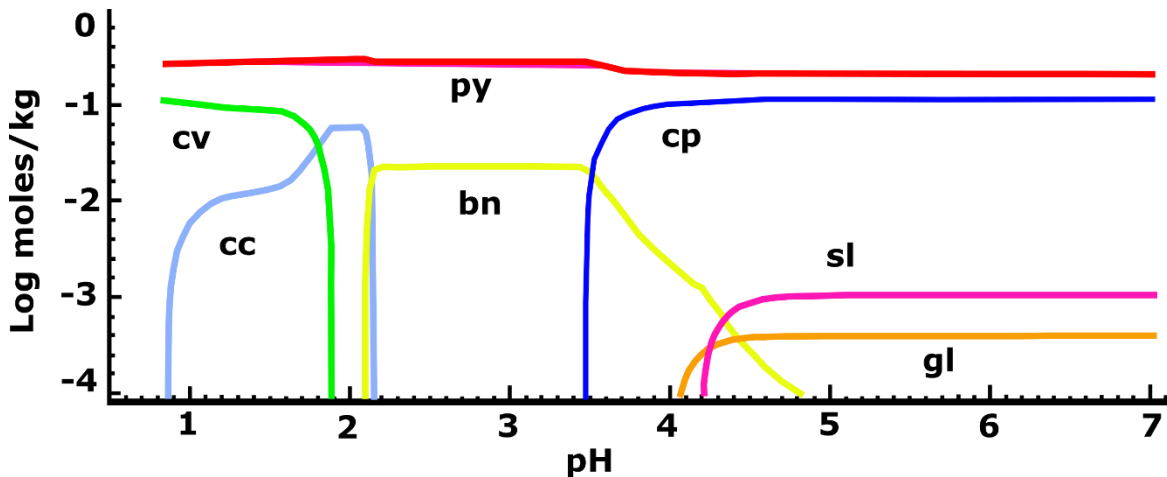


Figure 1.4: Experimental run demonstrating variations in the mineral assemblage of the Cu-Fe-S system with temperature constant at 200°C and pH ranging from 0.8 to 7. Modified from Reed and Palandri, 2006.

Analysis of sulphide precipitation was also done focusing on the cooling of hydrothermal fluids under static pH and salinity conditions (pH 6.5, 1 mol NaCl). This experiment indicated that, as temperatures decrease below 300°C, all aqueous metal sulphides present would become saturated and precipitate due to the breakdown of each metal's respective chloride complex (Fig. 1.5; Lydon et al., 1985; Reed & Palandri, 2006).

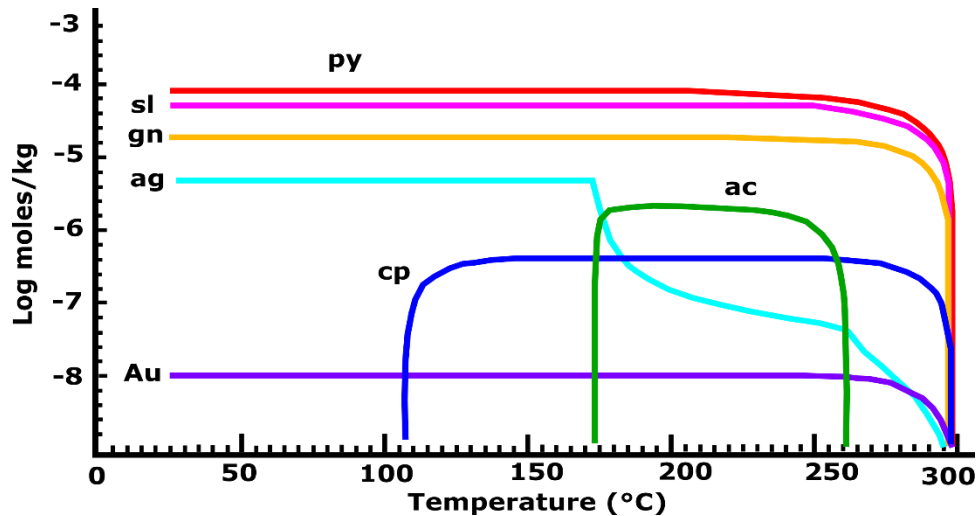


Figure 1.5: Experimental constant cooling run of a 1m NaCl fluid with a constant composition and  $\Delta\text{pH}$  of 0.5 less than neutral. The fluid was initially saturated with sphalerite, chalcopyrite, galena, pyrite, magnetite, and electrum ( $X_{\text{Au}} = 0.69$ ) and was cooled from 300 to 25°C. (Modified from Reed and Palandri, 2006).

#### *High-Temperature Black Smoker Venting Sites:*

In addition to pH-controlled mineral formation at vent deposits, seafloor sulphide mineralization is also largely controlled by the temperature,  $f\text{O}_2$ , and concentration of dissolved ions of the ascending fluids (Tivey & McDuff, 1990). The mixing of hydrothermal fluids with seawater creates concentric zones of mineralization, with variation in different mineral abundances dictated by the insulation provided by the chimney walls (Hannington et al., 1995). Chalcopyrite, anhydrite, pyrrhotite, sphalerite, and barite precipitate at progressively lower temperatures, respectively, due to increasing amounts of seawater and hydrothermal fluid mixing (Janecky & Seyfried, 1984). Pyrrhotite is abundant in high-temperature vent sites but rarely forms at a lower temperature, more diffuse vents (Hannington et al., 1995). Commonly, the hexagonal, non-magnetic variety of pyrrhotite is precipitated from hydrothermal fluids (Eq. 8) (Janecky & Seyfried, 1984). Due to its increased stability in high temperature and low  $f\text{O}-f\text{S}_2$  conditions, pyrrhotite is often the initial precipitate to form from undiluted hydrothermal fluids and makes up most of the particulate material found in the “black smoke” produced during active venting (Spiess et al., 1980; Zierenberg et al., 1984). Pyrrhotite is not often found as a major mineral phase in chimneys or mounds, however, as it tends to oxidize quickly compared to other seafloor sulphide



Other common iron-sulphide minerals present at black smoker venting sites are the iron-disulphide polymorphs pyrite and marcasite ( $\text{FeS}_2$ ). Both polymorphs precipitate from the  $\text{Fe}^{2+}$  ions present in the ascending hydrothermal fluids and are found within most black smoker mineral assemblages (Janecky & Seyfried, 1984). Pyrite begins to precipitate at  $\sim 295^\circ\text{C}$  in a wide range of pH conditions (Fig. 1.4; Bowers et al., 1985; Janecky & Seyfried, 1984). Marcasite, however, will only precipitate within a limited range of physicochemical conditions. It is dominant at relatively high temperatures (up to  $240^\circ\text{C}$ ) and in pH conditions of less than 5 (Murowchick & Barnes, 1986). The rate of pyrite precipitation (Eq. 7) is slow relative to pyrrhotite (Eq. 8) but occurs over a wider range of physiochemical conditions (Fig. 1.4 and Fig. 1.5) (Janecky & Seyfried, 1984).



The timing and amount of pyrite precipitation is important to note relative to pyrrhotite as it has been documented to have a significant impact on subsequent sulphide mineral precipitation (Janecky & Seyfried, 1984). For example, if pyrite is the primary iron sulphide mineral being precipitated, sphalerite will precipitate at  $180^\circ\text{C}$ . However, sphalerite will precipitate at  $255^\circ\text{C}$  when pyrrhotite is the dominant iron sulphide mineral (Janecky & Seyfried, 1984).

Sphalerite and wurtzite (both with the chemical formula  $(\text{Zn,Fe})\text{S}$ ) are the most abundant zinc sulphides minerals present at seafloor hydrothermal vents. These Zn-rich sulphide minerals are a solid solution, differentiated by their abundances of Fe and Zn. The relative Zn and Fe abundances are controlled by temperature and  $f\text{S}_2$  conditions, which are largely controlled by the insulating ability of the active chimney during mineralization (Scott & Barnes, 1972). Wurtzite is the high temperature (stable between  $600$  and  $1240^\circ\text{C}$  at 1 atm) hexagonal polymorph of isometric sphalerite (Scott & Barnes, 1972; Zierenberg et al., 1984); however, both minerals occur at higher temperature venting sites (Fouquet et al., 1993). The transition between the two Zn-sulphide minerals is gradational. Wurtzite is dominant within the high-temperature vent interior, decreasing in abundance as temperatures decrease, where sphalerite is more abundant (Scott & Barnes, 1972). The transition from sphalerite into wurtzite may occur under low  $f\text{S}_2$  conditions above  $150^\circ\text{C}$  (Scott & Barnes, 1972).

In addition to anhydrite, barite and amorphous silica are common non-sulphide minerals found at high-temperature black smoker chimneys (Tivey & Delaney, 1986). Barite ( $\text{BaSO}_4$ ) forms over a wide range of temperatures throughout the evolution of a chimney (Jamieson et al., 2016). The abundance of barite is largely controlled by the concentration of Ba within the underlying substrate (Hannington & Scott, 1988). Amorphous silica precipitates from the conductive cooling of hydrothermal fluids and is often responsible for the long-lasting stability of seafloor chimneys (Tivey & Delaney, 1986). It is estimated to precipitate out of solution as it cools below  $\sim 170^\circ\text{C}$  (Skirrow & Coleman, 1982).

#### *Low Temperature and Diffuse Venting:*

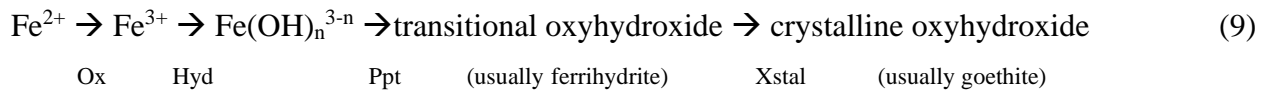
Low temperature (less than  $\sim 200^\circ\text{C}$ ) hydrothermal vents differ from traditional black smoker vents because they often lack the prominent upright chimney morphology and instead form bulbous mounds, with hydrothermal fluids being released through smaller interconnected pathways rather than a central conduit (Tivey, 1995). Low-temperature zinc sulphide-rich vent sites have been discovered at many of the major seafloor venting sites (e.g., East Pacific Rise, Juan de Fuca Ridge, TAG) where, due to lower temperature fluids, Zn-rich mineral assemblages are dominant rather than the Cu-rich assemblages associated with higher temperatures (Koski et al., 1984, 1994). The dominant minerals at these sites are anhydrite, sphalerite, pyrite, wurtzite, chalcopyrite, and minor amounts of pyrrhotite (Tivey, 1995). At these sites, sphalerite rather than anhydrite acts as the major mineral to make up the chimney interior “matrix.” A model has been developed for these specific venting sites (Koski et al., 1984; Paradis et al., 1988; Koski et al., 1994; Tivey, 1995), where the earliest Zn-rich hydrothermal fluids at the seafloor rapidly precipitate or quench to create the framework for subsequent sulphide mineral precipitation. Slow fluid flow generates a complex network of fluid pathways, and these pathways contain colloform sphalerite within rings of higher temperature chalcopyrite and pyrite that restrict and eventually block the fluid pathways. As fluid pathways are restricted and sealed, fluids are forced laterally towards the sulphide structure’s exterior to release pressure, generating a bulbous morphology.

Diffuse venting describes low temperature ( $10 - 50^\circ\text{C}$ ) fluids that are not associated with significant mineralization, as temperatures are too low to transport metals or sulphur. Minerals typically precipitated include iron-oxyhydroxides, Mn-oxides, authigenic clays, and silica (Hannington et al., 1995). Diffuse venting occurs over the full life span of a hydrothermal vent

system, associated with the earliest stages of hydrothermal venting while also commonly occurring at the fringes of high-temperature venting systems (Hannington et al., 1995). The waning of high-temperature venting also results in diffuse venting before the end of a venting system's lifecycle (Hannington et al., 1995).

*Fe-Oxides and Oxyhydroxides:*

Iron-oxides and oxyhydroxides form under oxidizing conditions on the exposed surfaces of hydrothermal structures. They are products of both biotic and abiotic processes that leach iron from Fe-bearing minerals (Barker et al., 1998). Goethite ( $\alpha$ -FeOOH) is one of the most abundant stable iron-oxyhydroxides. The formation of goethite is a multi-step process that begins with the initial precipitation of ferrihydrite ( $(\text{Fe}^{3+})_2\text{O}_3 \cdot 0.5\text{H}_2\text{O}$ ), a poorly ordered and relatively unstable oxyhydroxide, which converts into the more stable goethite (Blowes et al., 2003). A general formula for the formation of goethite is as follows:



where reactions occurring are Ox = oxidation of ferrous iron, Hyd = hydrolysis of a simple metal species, Ppt = precipitation of ferric iron, and Xstal = recrystallization of the transitional oxyhydroxide into a relatively stable crystalline phase (Grundl & Delwiche, 1993). If temperature conditions rise above 300°C goethite will dehydrate into hematite (Opdyke & Channell, 1996). Hematite ( $\text{Fe}_2\text{O}_3$ ) is an Fe-oxide mineral that is less abundant under aqueous conditions relative to goethite when compared to other minerals found in hydrothermal vent assemblages. Hematite's lower abundance is due to it needing to compete for  $\text{Fe}^{3+}$ , a by-product in the formation of the oxyhydroxide species ferrihydrite. Hematite can form from both the dehydration of goethite and at a pH ~8 where the concentration of monovalent  $\text{Fe}^{3+}$  is at its lowest (Schwertmann, 1983).

### 1.2.3 Oxidation of Sulphides

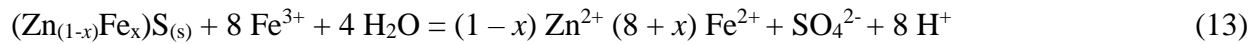
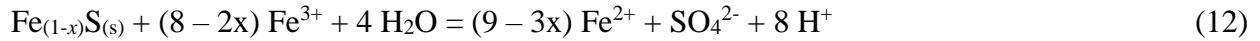
Seafloor massive sulfide deposits are subject to two major weathering processes. The first is dissolution, where material is converted from its original solid state into a solute, which then mixes with a solvent (in this case seawater) to form a solution. The second process is oxidation, where one half of a given redox reaction occurs through the transfer of electrons in a non-

equilibrated system (Moses et al., 1987). During periods of high-temperature hydrothermal activity, sulphide minerals exposed to the high temperatures on the seafloor are subject to reducing condition and no microbial influence and are thus relatively stable. However, if sulphide minerals are exposed to the combination of  $\text{Fe}^{2+}$  ions from hydrothermal fluids and  $\text{O}_2$  from seawater, they will readily oxidize (Lowson, 1982).

Rates of oxidation of sulfide minerals on the seafloor will vary depending on the environmental conditions present. Increases in temperature, acidity, and the presence of a more reactive oxidizer such as  $\text{Fe}^{3+}$  can greatly increase oxidation rates. In oxidizing conditions, pyrite releases  $\text{Fe}^{2+}$  ions, which are subsequently oxidized by available  $\text{O}_2$  to form  $\text{Fe}^{3+}$  (Eq. 10), which precipitates as Fe-oxyhydroxides (Eq. 11), mainly ferrihydrite and goethite (summarized by Eq. 9) (Belzile et al., 2004; Gartman et al., 2014; Singer & Stumm, 1970):



When present,  $\text{Fe}^{3+}$  can rapidly oxidize most sulphide minerals, such as pyrrhotite (Eq. 12) (Janzen et al., 2000) and sphalerite (Eq. 13) (Rimstidt et al., 1993):



Oxidation of sulphide minerals on the seafloor is not limited to iron reacting with oxic seawater in these environments. Within the microbial communities that develop at actively venting sites are microorganisms that utilize the oxidation of sulphide minerals and sulphur as a part of their lithoautotrophic metabolism (Konhauser et al., 2007). Influencing oxidation reactions in a catalytic capacity, autotrophic bacteria such as *Thiobacillus ferrooxidans* act as a catalyst to promote oxidative dissolution of sulphide minerals by oxidizing  $\text{Fe}^{2+}$  into  $\text{Fe}^{3+}$  and producing sulphuric acid from inorganic sulphur compounds, which creates localized acidic porewaters (Suzuki, 1974; Suzuki et al., 1994). Due to the generated acidity, the  $\text{Fe}^{3+}$  can remain in solution and has the potential to act as the primary oxidizing agent (Nordstrom & Southam, 1997).

### 1.2.3.1 *Sulphide Oxidation Mechanics*

Seafloor sulphide mineral oxidation produces metal oxides and oxyhydroxides. To quantify rates of sulphide mineral oxidation, there has been a significant number of experimental studies completed (e.g., ; Lawson, 1982; Moses et al., 1987; Bierens de Haan, 1991; Rimstidt & Vaughan, 2003; Belzile et al., 2004; Heidel et al., 2013a). Oxidation rates are typically calculated using the amount of metals released into solution. However, the sequestration capacity of oxyhydroxides within hydrothermal vents complicates these calculations, making it extremely difficult to determine accurate rates of oxidation (Knight et al., 2017). For example, the presence of Fe-oxyhydroxides make determining rates of dissolution for Cu or Zn sulphide minerals more difficult as they adsorb metals such as Cd, Cu, Zn, and Pb (Benjamin & Leckie, 1981). The preferential oxidation of polymineralic deposits, relative to monomineralic deposits (see Section 1.2.4), oxidation rates that have largely been calculated from experiments involving single phase sulphide oxidation may not reflect natural oxidation rates seen on the seafloor (Heidel et al., 2013b; Knight et al., 2017). Therefore, this section attempts to summarize the current understanding oxidation processes from experimentally determined single and multiphase experiments.

#### *Pyrite/ Marcasite:*

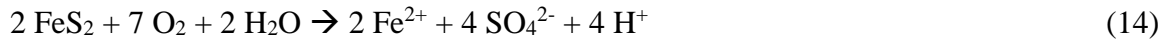
Pyrite ( $\text{FeS}_2$ ) is commonly the most abundant sulphide mineral in hydrothermal vents and is found within most mineral assemblages. Because of its abundance and its potential to generate acid mine drainage (AMD) in terrestrial settings, extensive work has focused on the oxidation of pyrite (Lawson, 1982; Bierens de Haan, 1991; Rimstidt & Vaughan, 2003; Chandra & Gerson, 2010).

Pyrite oxidation in oxygenated abiotic conditions has three major controlling factors: the amount of surface area exposed; concentration of the oxidizing medium present; and the initial pH of oxidizing conditions (Bierens de Haan, 1991). An additional reactivity factor noted by Lawson (1982) is the morphology and crystal structure of the reacted sulphide, where the most to least reactive morphologies were marcasite, framboidal pyrite, then euhedral pyrite. Oxidation of individual grains is often non-uniform, with initial reactions occurring at sites with higher surface area such as grain edges and corners, defects, pits, cleavage planes, or fractures (Bierens de Haan, 1991). There are three major reaction paths identified for the aqueous oxidation of pyrite by molecular oxygen: chemical, electrochemical, and bacterial (Lawson, 1982). Subsequently, a

review of sulphide oxidation literature by Chandra and Gerson (2010) has highlighted that there is a general acceptance of electrochemistry being the primary sulphide mineral oxidation process.

The chemical oxidation pathway is a sequence of three steps: (1) the oxidation of pyrite to sulphate and ferrous iron ( $\text{Fe}^{2+}$ ), (2) oxidation of  $\text{Fe}^{2+}$  into  $\text{Fe}^{3+}$ , and (3) further oxidation of pyrite to sulphate and  $\text{Fe}^{2+}$  using the generated  $\text{Fe}^{3+}$  as the electron acceptor (Lowson, 1982).

(1) The chemical oxidation of pyrite can be represented by the reaction:

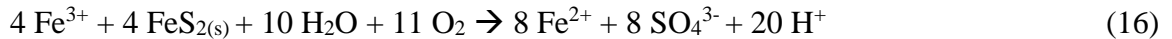


This reaction takes place at the surface of the reactive sulphide mineral and has a rate of reaction based upon the morphology, surface area, and pH. Oxidation rates increase nonlinearly as pH decreases from 1 to 10 (Lowson, 1982).

(2) The oxidation of  $\text{Fe}^{2+}$  into  $\text{Fe}^{3+}$  (Eq. 15) is controlled by pH,  $\text{Fe}^{2+}$  concentration, oxidizing agent concentration (i.e. dissolved  $\text{O}_2$  in seawater), temperature, and presence of catalytic materials:



(3) Oxidation of pyrite by  $\text{Fe}^{3+}$  (Eq. 16) is the last step and occurs heterogeneously at the reacting sulphide mineral's surface. The rate at which this occurs is based upon the amount of  $\text{Fe}^{2+}$ ,  $\text{Fe}^{3+}$ , surface area being reacted, and pH:



Nicholson and others (1988) demonstrated that pyrite oxidation under circumneutral conditions will form an Fe-oxyhydroxide product (Eq. 17):



The electrochemical oxidative pathway is made up of two half-cell reactions, one for a cathode and one for an anode (Lowson, 1982). The three processes that occur are: (1) a cathodic reaction, (2) the transport of electrons, and (3) an anodic reaction (Fig. 1.6) (Rimstidt & Vaughan, 2003).

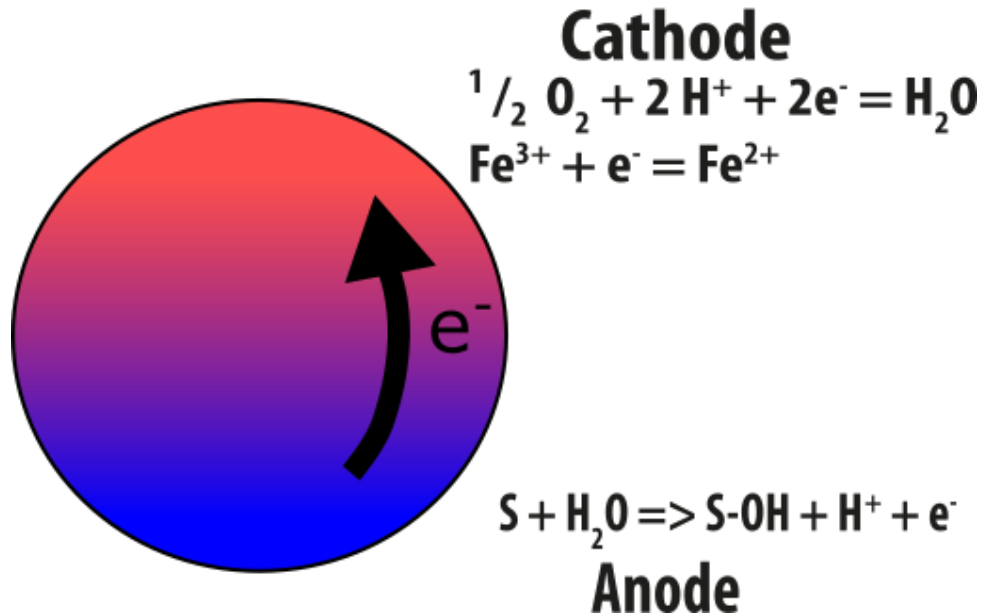


Figure 1.6: Breakdown of the three steps pyrite undergoes for electrochemical oxidative dissolution (Rimstidt & Vaughan, 2003).

Cathodic reaction: sulphur is oxidized in the presence of O<sub>2</sub>-rich seawater. Iron remains in its reduced state (Rimstidt & Vaughan, 2003):



The most prominent oxidant species occurring in nature are O<sub>2</sub> and Fe<sup>3+</sup> (Eq. 10 and 11). Here, the electron transfer from the sulphide to oxidant at the cathodic site is the rate determining step for sulphide oxidation (Brown & Jurinak, 1989) due to the dependence on the concentrations of Fe<sup>3+</sup> or O<sub>2</sub> (Rimstidt & Vaughan, 2003).

Electron transfer: transportation across a mineral that is acting as an electrochemical cell requires first transferring the electrons from the anodic site to the cathodic site, and then to the aqueous oxidant (Rimstidt & Vaughan, 2003).

Anodic reaction: removal of seven electrons from a di-sulphur species like pyrite, or eight electrons in the case of a single sulphur sulphide. The product in both circumstances is sulphate; however, the sulphur atoms must proceed through several oxidation states and potentially multiple intermediate sulphur compounds during the process (Anderson et al., 1989; Viravamurthy & Zhou, 1995).

Lastly, the bacterial pathway of oxidation has both a direct and indirect influence on oxidation rates. The direct approach taken by Fe leaching bacteria is to affix to the sulphur portion of a target sulphide mineral. The bacteria dissolve the sulphide's metal component, causing pitting across the surface of the afflicted sulphide (Lundgren & Silver, 1980). Bacteria may also accelerate the rates of sulphide oxidation by promoting the oxidation of  $\text{Fe}^{2+}$  to  $\text{Fe}^{3+}$ , which is otherwise a naturally slow reaction. Under ideal conditions, Fe-oxidizing bacteria can accelerate this reaction up to  $10^6$  times (Singer & Stumm, 1970). The Fe-oxidizing bacteria *Thiobacillus ferrooxidans* exist over a wide range of pH within the temperature range of 20°C to 55°C (Sullivan et al., 1980; Hutchins et al., 1986). However, they are most active in pH conditions where  $\text{Fe}^{3+}$  is stable in solution (pH 1 – 2.5) (Lundgren & Silver, 1980). *Thiobacillus ferrooxidans* are also able to create acidic conditions by acting as catalysts for the oxidation of elemental sulphur (Eq. 20) (Brierley, 1980):

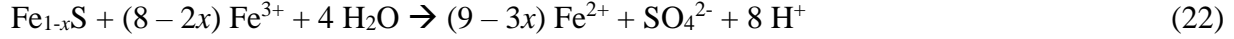


*Pyrrhotite:*

For pyrrhotite, the major oxidants are oxygen in circumneutral and alkaline pH, and ferric iron at low pH (Belzile et al., 2004). When oxygen is the dominant oxidizing agent, the reaction under which pyrrhotite undergoes oxidation is (Nicholson & Sharer, 1994):



If  $\text{Fe}^{2+}$  is oxidized to form  $\text{Fe}^{3+}$  in solution at low pH, the product  $\text{Fe}^{3+}$  can act as an oxidizing agent for pyrrhotite, creating an even more acidic environment (Belzile et al., 2004):



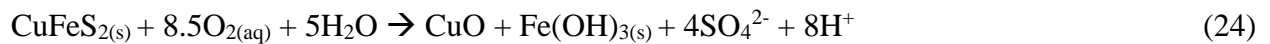
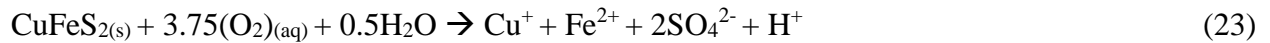
Under acidic conditions most of the product  $\text{Fe}^{3+}$  (Eq. 9) will remain in solution, driving equation (22). These two reactions, acting in a cyclic manner, will therefore sustain acidic conditions and, utilizing  $\text{Fe}^{3+}$  as the oxidizing agent, rapidly oxidize any existing sulphide minerals (Belzile et al., 2004).

The oxidation of pyrrhotite occurs via a series of Fe-deficient sulphide and metastable polysulphide intermediates. The resulting products generated by the oxidation of pyrrhotite is goethite and elemental sulphur (Steger & Desjardins, 1978). Both lab and field studies suggest that the generation of elemental sulphur is due to incomplete oxidation of pyrrhotite (Steger, 1982; Jambor, 1986; Ahonen & Tuovinen, 1994).

*Thiobacillus ferrooxidans* promotes the oxidation of pyrrhotite, producing native sulphur, acidic conditions, and precipitation of K-jarosite ( $\text{KFe}_3(\text{SO}_4)_2(\text{OH})_6$ ), goethite ( $\alpha\text{-FeOOH}$ ), and schwertmannite ( $\text{Fe}_8\text{O}_8(\text{OH})_6\text{SO}_4$ ) (Bhatti et al., 1993).

#### *Chalcopyrite:*

In ambient conditions, the rate of dissolution of chalcopyrite is slow relative to other sulphide minerals, with other Cu-rich minerals, such as covellite, reacting at a higher rate. In acidic (Eq. 23) and neutral to alkaline (Eq. 24) conditions were also performed, in which, like pyrite, oxidation under neutral to alkaline conditions resulted in the formation of iron-oxyhydroxide.



When chalcopyrite dissolution is occurring with  $\text{Cu}^{2+}$  ions available in solution the surface of chalcopyrite can be converted into covellite (Fig. 1.7), or at least become a surface with the anodic characteristics of covellite (Nicol et al., 2017):



Previous experiments have highlighted similarities between the dissolution rates and the activation energies required to initiate dissolution for a given mineral. This may imply that either covellite

and chalcopyrite dissolution reactions occur with similar kinetics, or covellite may be an intermediate product in the dissolution of chalcopyrite (Miki & Nicol, 2008a).

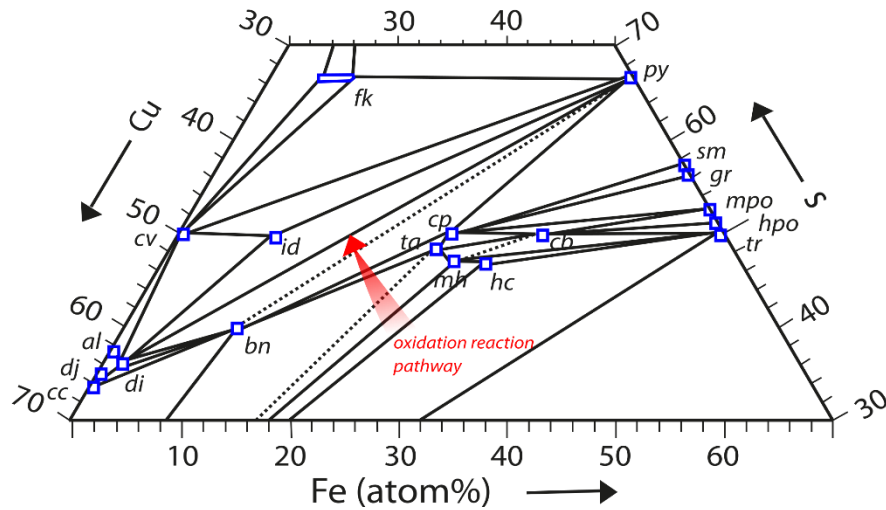


Figure 1.7: Possible phase relations at 25 °C (atom %) of Cu-Fe-S system, after Vaughan and Craig (1997, their Figs. 8.17 and 8.21) (Modified by Hannington, 1993). Arrow indicates the progressive removal of Fe and Cu due to late stage weathering of sulphide ore. Abbreviations: al = anilite; bn = bornite; cb = cubanite; cc = chalcocite; cp = chalcopyrite; cv = covellite; di = digenite; dj = djurleite; fk = fukuchilite; gr = greigite; hc = haycockite; hpo = hexagonal po; id = idaite; mh = mooihoekite; mpo = monoclinic po = pyrrhotite; py = pyrite; sm = smythite; ta = talnakhite; tr = troilite.

When chalcopyrite dissolution occurs in more acidic conditions (pH 1 – 3), the rate of dissolution is only partly dependant on the hydrogen ion activity, resulting in minimal change in the reaction rates (Acero et al., 2009). Additionally, when in acidic conditions the reactive surfaces of chalcopyrite preferentially release Fe into solution, resulting in the surface composition of chalcopyrite being enriched in S and Cu relative to Fe (Acero et al., 2009).

Oxidative reactions can alter the stoichiometry of chalcopyrite. Chalcopyrite-rich samples collected from the Mid-Atlantic Ridge by Mozgova and others (2005), showed evidence of stoichiometric variations to the amount of Cu in tarnished chalcopyrite. These variations are due to the valence states of chalcopyrite's elemental components ( $\text{Cu}^+\text{Fe}^{3+}\text{S}_2$ ), where Fe is already in its highest possible oxidation state. Copper, however, is in its monovalent state and can be oxidized to  $\text{Cu}^{2+}$  (Mozgova et al., 2005).

### *Sphalerite:*

Experimental work with synthetic seawater indicates that sphalerite has a relatively complex and unpredictable oxidation reaction series (Knight et al., 2017). Sphalerite will consistently oxidize rapidly until passivation or oxidative shielding is reached across the reacting mineral surface area (Knight et al., 2017). Following this period of stability or resistance to oxidation, more Zn is released into solution, indicating further oxidation, suggesting that surficial armouring is eventually breached, resulting in further rapid oxidation (Knight et al., 2017).

Sphalerite oxidation in an oxygen-rich environment is not affected by pH conditions, and oxidized zinc ions are released into solution (Eq. 26).



#### **1.2.4 Galvanic Interactions between Sulphide Minerals**

In experimental work centred upon oxidation reactions of polymetallic sulphide deposits, it was found that a greater quantity of oxide precipitates was produced in polymineralic experiments when compared to monomineralic experiments (Heidel et al., 2013b; Knight et al., 2017). Polymetallic sulfide-rich deposits are subject to nearly continuous electrochemical processes due to their mixed mineralogy, metallic content, and the constant presence of seawater. These interactions between sulphide minerals produce galvanic cells, which are electrochemical cells that derive energy from spontaneous redox reactions. Specific to the conditions of this study, a galvanic cell is the spontaneous flow of electrons between two conductive minerals with differing resting potentials (resting potential refers to the electric potential at which anodic and cathodic currents within a mineral are equal) that are in contact with one another in a conductive aqueous solution (seawater). Under these conditions, the difference in resting potential acts as the electrochemical driver (Table 1.1) (Mehta & Murr, 1983). The resting potential of individual minerals is not a static value but is influenced by a factors including the composition of the electrolyte, pH, temperature, and mineral impurities (Fallon et al., 2017).

Table 1.1 Resting potential of various sulphide minerals commonly found within seafloor massive sulphide deposits. Modified from Mehta and Murr, 1983.

Mineral	Resistivity ( $\Omega \cdot m$ )	Crystal Structure	Solution	Temperature
Pyrite ( $FeS_2$ )	$3 \times 10^{-2} - 1 \times 10^{-3}$	Cubic	1.0 M $H_2SO_4$	25°C
Chalcopyrite ( $CuFeS_2$ )	$2 \times 10^{-4} - 9 \times 10^{-3}$	Tetragonal	1.0 M $H_2SO_4$	25°C
Chalcocite ( $Cu_2S$ )	$3 \times 10^{-2} - 1 \times 10^{-3}$	Orthorhombic	1.0 M $H_2SO_4$	20°C
Covellite ( $CuS$ )	$8 \times 10^{-5} - 7 \times 10^{-6}$	Hexagonal	1.0 M $HClO_4$	25°C
Galena ( $PbS$ )	$1 \times 10^{-5} - 7 \times 10^{-6}$	Cubic	1.0 M $H_2SO_4$	20°C
Sphalerite ( $ZnS$ )	$3 \times 10^{-3} - 1 \times 10^{-4}$	Cubic	1.0 M $H_2SO_4$	20°C

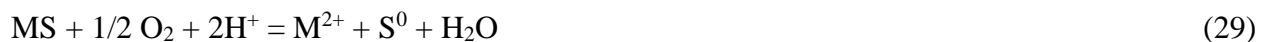
The difference in the resting potentials of two adjacent minerals result in the mineral with the higher resting potential acting as the cathodic endmember of the electrochemical cell, and is galvanically protected by contributing electrons electrochemical circuit (Mehta & Murr, 1983):



The opposing mineral with the lower resting potential acts as an anode:



Where MS = metal sulphide, and M = a bivalent metal. The complete galvanic reaction of mixed potential minerals under acidic conditions is as follows:



An example of one such mixed potential reaction, using pyrite as the catalytic cathode (driving the reaction without being itself reacting) and chalcopyrite as the anode is:



The direction of the redox reaction defines each mineral as either the cathode or anode. The site in which oxidation occurs is the anode, and the site where reduction of O<sub>2</sub> occurs is the cathode (Frankel, 2016). The specific site locations for the anode and cathode can be located at fixed locations on the reactive surfaces. Alternatively, the reactive surfaces may randomly move across surfaces, creating more localized corrosion patterns such as pitting, crevice corrosion, and intergranular corrosion. Initial studies of galvanic interactions between sulphide minerals observed that, when specifically studying chalcopyrite as the anode, it was possible to determine that variations in the cathode mineral would accelerate or retard the oxidation reactions (Mehta & Murr, 1983). In this example, rates of oxide dissolution of chalcopyrite were accelerated by the presence of pyrite, molybdenite, and stibnite, but was retarded by the presence of galena. This study highlights that the major variables influencing the rate of oxide dissolution within polymetallic sulphide ore deposits were pH, mineralogy, Fe content of the present minerals, the relative abundance of each mineral, and grain size (or surface area that is exposed to oxidation) while comparing and contrasting these results with the presence or lack of bacteria.

Bacteria have been observed to have a direct impact on the reactive efficiency of galvanic cells and the rates of preferential dissolution in polymetallic seafloor massive sulphide deposits. Mehta and Murr (1983) determined that at 30°C and 55°C, *T. ferrooxidans* and thermophilic bacteria, respectively, enhance the rate of metals that are leached from polymineralic sulphide samples. This phenomenon was attributed to the bacteria converting reduced S into H<sub>2</sub>SO<sub>4</sub> and accelerating the galvanic interactions between CuFeS<sub>2</sub> and FeS<sub>2</sub> mineral grains (Fig. 1.8).

## **1.3 Methods**

### **1.3.1 Sampling**

Samples were collected by J. Jamieson and S. Piercey (Memorial University of Newfoundland) from active and inactive hydrothermal vent chimneys along the Endeavour Segment using the ROV *ROPOS*, during a 12-day cruise aboard the R/V John P. Tully involving researchers from Fisheries and Oceans Canada, University of Victoria, and Memorial University of Newfoundland. High-resolution (1 m) bathymetric maps (Clague et al., 2014) served as a guide to locate inactive vents at varying distances away from the ridge axis, assuming that older

and thus more oxidized inactive vents occur further away on the axial valley wall from the hydrothermally-active valley floor (Jamieson et al., 2013).

Samples were rinsed in fresh water and set out to dry over several days while onboard the ship. Samples were described and photographed once they were shipped back to Memorial University.

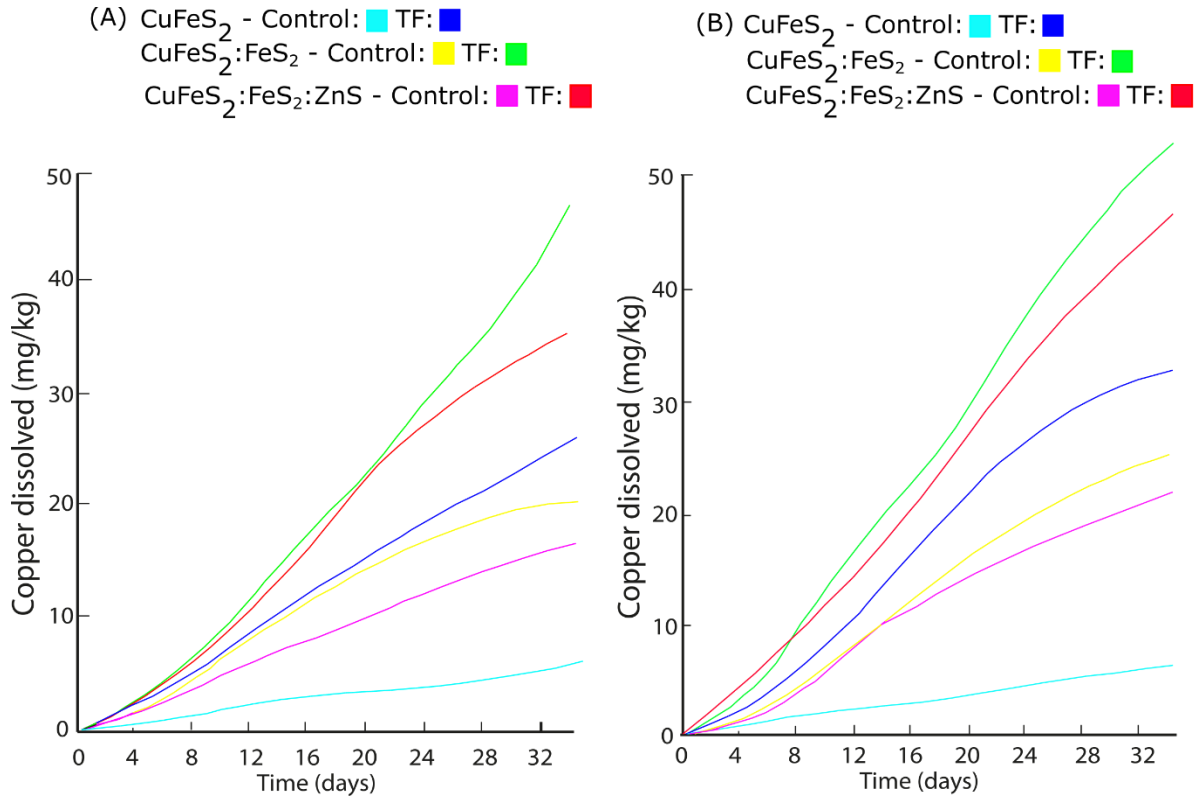


Figure 1.8: Comparison of Cu dissolution rates between isolated Chalcopyrite ( $\text{CuFeS}_2$ ), galvanically coupled chalcopyrite-pyrite ( $\text{CuFeS}_2\text{-FeS}_2$ ), and chalcopyrite-pyrite-sphalerite ( $\text{CuFeS}_2\text{-FeS}_2\text{-ZnS}$ ). Comparison with the presence and absence of (a) *T. ferrooxidans* at 30°C (b) thermophilic bacteria at 55°C. T.F. = *T. ferrooxidans*, TH = thermophilic bacteria.

### 1.3.2 Petrography

Thin sections were made at Memorial University of Newfoundland. Due to their porous nature, slabs were impregnated with epoxy before sawing. Thin sections were cut to expose a cross-section from interior to exterior of chimney walls. Thin section observations were made using a Nikon LV100NPOL microscope under both transmitted and reflected light.

### 1.3.3 Scanning Electron Microscope (SEM)

A JEOL JSM-7100F scanning electron microscope (SEM) at Memorial University of Newfoundland with field-emission source and an HKL backscattered-electron detector was used to image samples at high resolution. The SEM was operated at an accelerating beam of 15 kV. Energy dispersive spectrometry (EDS) was used to determine approximate stoichiometric ratios within iron-oxide coatings and discern individual oxide phases.

### 1.3.4 Whole Rock Geochemistry

Powdered sub-samples were sent to Actlabs, Ontario for whole rock major and trace element analysis. Elemental abundances were collected using either instrumental neutron activation analysis (INAA) or Na<sub>2</sub>O<sub>2</sub> fusion preparation and inductively coupled plasma optical emission and mass spectrometry (ICP-OES/MS). Accuracy for all elements measured by INAA is <6%, determined by comparing repeat analyses (n=7) of the GXR-1 standard. The 1σ precision of INAA measurements of GXR-1 was determined to be <5%, except for Tb at 5.2%. The accuracy of the Na<sub>2</sub>O<sub>2</sub> fusion ICP-OES/MS method, calculated by repeat measurements (n=3) of the OREAS 621 certified standard is within 8%, with the exception of Nd (19%), Pr (14%), Sb (13%), Th (11%), and Y (8.2%). The 1σ precision of these analyses was determined to be within 5%, with the exceptions of In (44%), Ce (5.7%), and Cr (8.7%). Additionally, Na<sub>2</sub>O<sub>2</sub> fusion ICP-OES/MS uncertainty was also monitored using the OREAS 922 standard with results and fell within 10% accuracy of the certified value with the exceptions of Cr (33%), Eu (16%), Gd (21%), Ho (13%), Hf (68%), Li (11%), Nd (16%), Ni (16%), Pr (13%), Sr (17%), Th (13%), Tl (11%), Yb (11%), and Zn (34%). OREAS 922 calculations were determined to be precise within 7% at 1σ with the exceptions of Bi (8.2%), Cs (8.3%), Er (9.7%), La (10%), Nb (10%), Ni (23%), Pb (11%), S (9.6%), Tm (9.2%), V (9.8%), and Zn (45%).

### 1.3.5 Geochronology

Ages were calculated using the following decay equation:

$$t = \frac{\ln\left(\frac{N_0}{N}\right) * 1600 \text{ yrs}}{\ln 2}$$

where  $t$  is age in years,  $N$  is the ratio of the activity of  $^{226}\text{Ra}$  to the Ba content of the sample (wt. %),  $N_0$  is the initial  $^{226}\text{Ra}/\text{Ba}$  of the sample when the sample formed, and 1600 years is the half-life of  $^{226}\text{Ra}$ .

Radium-226 activities were measured at Memorial University of Newfoundland using a gamma spectrometer with a high-purity Ge detector with a well configuration. The spectral signature was calibrated using BL-2 natural uranium ore reference material. Crushed samples containing greater than 1% barium were sealed with an epoxy for 21 days to ensure secular equilibrium between  $^{226}\text{Ra}$ ,  $^{214}\text{Pb}$ , and  $^{214}\text{Bi}$  by preventing the escape of the intermediate  $^{222}\text{Rn}$  daughter isotope. Lead-214 and  $^{212}\text{Bi}$  are used as proxies for measurement of  $^{226}\text{Ra}$  activity due to decay energy peak interference between  $^{226}\text{Ra}$  and  $^{235}\text{U}$ . Here,  $^{214}\text{Pb}$  was the primary daughter product used for analysis due to its higher detector efficiency at its respective spectral peaks, relative to  $^{214}\text{Bi}$ . Instrument count time for each sample was 24 hours. The resultant spectral data collected was interpreted using ScienTissiME software, which corrects for background radiation, detector efficiency, sample volume, and sample density and other matrix effects. Age uncertainties were calculated by propagating the uncertainties of each variable through the age equation using standard error propagation techniques (see Jamieson et al. (2013) for details):

$$\delta t = \frac{1600\text{yrs}}{\ln 2} \left( \frac{\delta^{226}\text{Ra}}{^{226}\text{Ra}} + \frac{\delta\text{Ba}}{\text{Ba}} + \frac{\delta N_0}{N_0} \right)$$

## 1.4 Co-Authorship Statement

### Euripidis A. Papanicolaou

I am the sole author of this thesis.

### John Jamieson and Steve Piercey:

Samples and video imagery for this project were collected by Dr. John Jamieson, Dr. Steve Piercey and the science team and ROV pilots aboard the CCGS John P. Tully during the 2016 research cruise. Dr. Jamieson designed this M.Sc. project, and provided critical assistance

throughout the entire thesis process. This thesis benefited extensively from edits and feedback provided by Dr. Jamieson and Dr. Piercey.

## **1.5 Thesis Presentation**

This thesis consists of three chapters and three appendices. Chapter 1 introduces the geological background of the Endeavour segment, exploration history, a summary of the formation requirements of varying seafloor sulphide minerals, the overarching purpose of the study, and the methods used in completion of this thesis.

Chapter 2 is manuscript to be submitted for publication in 2020. This manuscript reports petrographic, geochemical, and geochronologic results from a research cruise conducted by the CCGS John P. Tully in 2016.

Chapter 3 present a summary of the results collected over the course of the thesis and suggestions for further research.

The appendices are composed of supporting data for the thesis. Appendix 1 is a seafloor sample collection site location summary. Appendix 2 contains whole-rock major and trace element geochemical results of 16 rock samples. Appendix 3 contains detailed petrographic descriptions of 15 seafloor samples.

## 1.6 References

- Abratis, P. K., Patrick, R. A. D., Kelsall, G. H., & Vaughan, D. J. (2004). Acid leaching and dissolution of major sulphide ore minerals: processes and galvanic effects in complex systems. *Mineralogical Magazine*, 68(2), 343–351. doi: 10.1180/0026461046820191
- Acerro, P., Cama, J., Ayora, C., & Asta, M. P. (2009). Chalcopyrite dissolution rate law from pH 1 to 3. *Geologica Acta*, 7(3), 389–397. doi: 10.1344/105.000001444
- Ahonen, L., Tuovinen, O.H. (1994). Solid-phase alteration and iron transformation in column bioleaching of a complex sulfide ore. In: Alpers, C.N., Blowes, D.W. (Eds.), *Environmental Geochemistry of Sulfide Oxidation*. ACS Symposium Series 550, American Chemical Society, Washington, DC, 79–89.
- Akaku K, Reed M.H., Yagi M., Kai K., Yasuda Y. (1991). Chemical and physical processes occurring in the Fushime geothermal system, Kyushu, Japan. *Geochem J* 25:315-334.
- Allen, D. E., & Seyfried, W. E. (2003). Compositional controls on vent fluids from ultramafic-hosted hydrothermal systems at mid-ocean ridges: An experimental study at 400°C, 500 bars. *Geochimica et Cosmochimica Acta*, 67(8), 1531–1542.
- Ames, D. E., Franklin, J. M., & Hannington, M. D. (1993). Mineralogy and geochemistry of active and inactive chimneys and massive sulfide, Middle Valley, northern Juan de Fuca Ridge: an evolving hydrothermal system. *Canadian Mineralogist*, 31(4), 997–1024.
- Anderson L. G., Gates P. M., and Nold C. R. (1989). Mechanism of atmospheric oxidation of sulfur dioxide by hydroxyl radicals. In *Biogenic Sulfur in the Environment* (eds. E. S. Saltzman and W. J., 393 Cooper), pp. 437–449. American Chemical Society, Washington, DC.
- Baker, E. T., & Massoth, G. J. (1987). Characteristics of Hydrothermal Plumes From 2 Vent Fields on the Juan-De-Fuca Ridge, Northeast Pacific-Ocean. *Earth and Planetary Science Letters*, 85(1–3), 59–73.
- Baker, E. T., & German, C. R. (2004). On the global distribution of hydrothermal vent fields. *Mid-Ocean Ridges: Hydrothermal Interactions Between the Lithosphere and Oceans*, *Geophys. Monogr. Ser.*, 148, 245-266.
- Bailey J.K., Brinker C.J., Mecartney M.L. (1993). Growth mechanisms of iron oxide particles of differing morphologies from the forced hydrolysis of ferric chloride solutions. *J Colloid Interface Sci* 157:1–13
- Beaulieu, S.E., (2015). InterRidge Global Database of Active Submarine Hydrothermal Vent Fields: prepared for InterRidge, Version 3.3. World Wide Web electronic publication. Version 3.4 accessed 2017-03-15, <http://vents-data.interridge.org>

- Becker, U., Munz, A.W., Lennie, A.R., Thornton, G., Vaughan, D.J. (1997). The atomic and electronic structure of the (001) surface of monoclinic pyrrhotite (Fe<sub>7</sub>S<sub>8</sub>) as studied using STM, LEED, and quantum mechanical calculations. *Surf. Sci.* 389, 66 – 87.
- Belzile, N., Chen, Y. W., Cai, M. F., & Li, Y. (2004). A review on pyrrhotite oxidation. *Journal of Geochemical Exploration*, 84(2), 65–76. doi: 10.1016/j.gexplo.2004.03.003
- Berkenbosch, H. A., De Ronde, C. E. J., Gemmell, J. B., McNeill, A. W., & Goemann, K. (2012). Mineralogy and formation of black smoker chimneys from brothers submarine volcano, Kermadec Arc. *Economic Geology*, 107(8), 1613–1633. <http://doi.org/10.2113/econgeo.107.8.1613>
- Bhatti, T.M., Bigham, J.M., Carlson, L., Tuovinen, O.H. (1993). Mineral products of pyrrhotite oxidation by *Thiobacillus ferrooxidans*. *Appl. Environ. Microbiol.* 59, 1984–1990.
- Bierens de Haan, S. (1991). A review of the rate of pyrite oxidation in aqueous systems at low temperature. *Earth-Science Reviews*, 31(1), 1–10. [http://doi.org/10.1016/0012-8252\(91\)90039-I](http://doi.org/10.1016/0012-8252(91)90039-I).
- Bischoff, J.L., and Rosenbauer, R.J. (1984). The critical point and two-phase boundary of seawater, 200-500°C: *Earth and Planetary Science Letters*, v. 68, no. 1, p. 172–180.
- Bischoff, J. L., & Rosenbauer, R. J. (1985). An empirical equation of state for hydrothermal seawater (3.2 percent NaCl). *American Journal of Science*, 285(8), 725-763.
- Bowles, J. F. W., Howie, R. A., Vaughan, D. J., & Zussman, J. (2011). Rock-forming minerals. *Volume 5A, Non-silicates: oxides, hydroxides and sulphides*.
- Brierley, J.A. (1980). Facultative *Thiobacillus*-like bacteria in metal leaching. In: *Biochemistry of ancient and modern environments*. Proc. 4th Int. Syrup. Environmental Biogeochem. (ISEB), Leaching Conf. (Canberra, Australia, 26 Aug.-4 Sept. 1979).
- Brown A. D. and Jurinak J. J. (1989). Mechanism of pyrite oxidation in aqueous mixtures. *J. Environ. Qual.* 18, 545–550.
- Burleson D.J., Penn R.L. (2006). Two-step growth of goethite from ferrihydrite. *Langmuir* 22:402– 409
- Burrows N.D., Hale C.R.H., Penn R.L. (2012). Effect of ionic strength on the kinetics of crystal growth by oriented aggregation. *Cryst Growth Des* 12:4787–4797
- Burrows N.D., Hale C.R.H., Penn R.L. (2013) Effect of pH on the kinetics of crystal growth by oriented aggregation. *Cryst Growth Des* 13:3396–3403

- Carbotte, S. M., Detrick, R. S., Harding, A., Canales, J. P., Babcock, J., Kent, G., Diebold, J. (2006). Rift topography linked to magmatism at the intermediate spreading Juan de Fuca Ridge. *Geology*, 34(3), 209–212. <http://doi.org/10.1130/G21969.1>
- Chan C.S., De Stasio G., Welch S.A., Girasole M., Frazer B.H., Nesterova M.V., Fakra S., Banfield J.F. (2004). Microbial polysaccharides template assembly of nanocrystal fibers. *Science* 303:1656– 1658
- Chandra, A. P., & Gerson, A. R. (2010). The mechanisms of pyrite oxidation and leaching: a fundamental perspective. *Surface Science Reports*, 65(9), 293-315.
- Clague, D. A., Brian M. Dreyer, Jennifer B. Paduan<sup>1</sup>, Julie F. Martin, David W. Caress, James B. Gill, Deborah S. Kelley, Hans Thomas, Ryan A. Portner, John R. Delaney, Thomas P. Guilderson, and M. L. M. (2014). Eruptive and tectonic history of the Endeavour Segment, Juan de Fuca Ridge, based on AUV mapping data and lava flow ages. *Geochemistry, Geophysics, Geosystems*, (15), 3364–3391.
- Cornell R.M., Schwertmann U. (2003). The iron oxides: structures, properties, reactions, occurrences and uses. Wiley-VCH, Weinheim
- Cornell R.M, Schwertmann U. (2006). The iron oxides: structure, properties, reactions, occurrences and uses, 2nd, completely revised and extended edition. Wiley-VCH, Weinheim
- Cornell R.M., Schneider W., Giovanoli R. (1989). Phase transformations in the ferrihydrite/cysteine system. *Polyhedron* 8:2829–2836
- Craig, J. R., Vaughan, D. J., & Hagni, R. D. (1981). *Ore microscopy and ore petrography* (Vol. 406). New York: Wiley.
- Craig J. R., Vokes F. M., and Solberg N. (1998). Pyrite: Physical and chemical textures. *Mineralium Deposita* 34, 82–101.
- Cudrak, C.F., and R.M. Clowes. (1993). Crustal structure of Endeavour Ridge segment, Juan de Fuca Ridge, from a detailed seismic refraction survey. *Journal of Geophysical Research* 98:6,329–6,349.
- Delaney, J. R., Robigou, V., McDuff, R. E., & Tivey, M. K. (1992). Geology of a vigorous hydrothermal system on the Endeavour Segment, Juan de Fuca Ridge. *Journal of Geophysical Research*, 97(B13), 19663–19682.
- Dodd, M. S., Papineau, D., Grenne, T., Slack, J. F., Rittner, M., Pirajno, F., Little, C. T. S. (2017). Evidence for early life in Earth’s oldest hydrothermal vent precipitates. *Nature*, 543(7643), 60–64. <http://doi.org/10.1038/nature21377>
- Evans, G. N., Tivey, M. K., Seewald, J. S., & Wheat, C. G. (2017). Influences of the Tonga Subduction Zone on seafloor massive sulfide deposits along the Eastern Lau Spreading

Center and Valu Fa Ridge. *Geochimica et Cosmochimica Acta*, 215, 214–246.  
<http://doi.org/10.1016/j.gca.2017.08.010>

- Feely, R. A., Lewison, M., Massoth, G. J., Robert-Baldo, G., Lavelle, W., Byrne, R. H., Von Damm, K. L., and Curl Jr., H. C. (1987). Composition and Dissolution of Black Smoker Particulates from Active Vents of the Juan de Fuca Ridge, *Journal of Geophysical Research*, 92(B11), pp. 11,347 – 11,363.
- Feely, R. A., Geiselman, T. L., Baker, E. T., Massoth, G. J., & Hammond, S. R. (1990). Distribution and composition of hydrothermal plume particles from the ASHES Vent Field at Axial Volcano, Juan de Fuca Ridge. *Journal of Geophysical Research*, 95(B8), 12855.  
<http://doi.org/10.1029/JB095iB08p12855>
- Fleet, M. E. (2006). Phase Equilibria at High Temperatures. *Reviews in Mineralogy and Geochemistry*, 61(1), 365–419. <http://doi.org/10.2138/rmg.2006.61.7>
- Fontaine, F. J., & Wilcock, W. S. D. (2006). Dynamics and storage of Brine in mid-ocean ridge hydrothermal systems. *Journal of Geophysical Research: Solid Earth*, 111(6), 1–16.
- Frandsen C., Legg B.A., Comolli L.R., Zhang H., Gilbert B., Johnson E., Banfield J.F. (2014). Aggregation-induced growth and transformation of b-FeOOH nanorods to micron-sized a-Fe2O3 spindles. *CrystEngComm* 16:1451–1458.
- Galley, A. G., Hannington, M. D., & Jonasson, I. R. (2007). Volcanogenic Massive Sulfide Deposits. *Mineral Deposits of Canada: A Synthesis of Major Deposit-Types, District Metallogeny, the Evolution of Geological Provinces, and Exploration Methods*, 111(5), 141–161. [http://doi.org/10.1016/0169-1368\(95\)00022-4](http://doi.org/10.1016/0169-1368(95)00022-4).
- Gartman, A., Yucel, M., Madison, A. S., Chu, D. W., Ma, S., Janzen, C. P., Luther, G. W. (2011). Sulfide Oxidation across Diffuse Flow Zones of Hydrothermal Vents. *Aquatic Geochemistry*, 17(4), 583–601.
- Gartman, A., Findlay, A. J., & Luther, G. W. (2014). Nanoparticulate pyrite and other nanoparticles are a widespread component of hydrothermal vent black smoker emissions. *Chemical Geology*, 366, 32–41.
- Glickson, D.A., D.S. Kelly, and J.R. Delaney (2006). The Sasquatch Hydrothermal Field: Linkages between seismic activity, hydrothermal flow, and geology. *Eos, Transactions, American Geophysical Union* 87(52): Fall Meeting Supplement Abstract V23B-0614.
- Goldstein, S. J., M. T. Murrell, D. R. Janecky, J. R. Delaney, and D. A. Clague (1991), Geochronology and petrogenesis of MORB from the Juan de Fuca and Gorda Ridges by U-238 Th-230 disequilibrium, *Earth Planet. Sci. Lett.*, 107(1), 25–41.

- Hannington, M., Herzig, P., Scott, S., Thompson, G., & Rona, P. (1991). Comparative mineralogy and geochemistry of gold-bearing sulfide deposits on the mid-ocean ridges. *Marine Geology*, 101(1–4), 217–248. [https://doi.org/10.1016/0025-3227\(91\)90073-D](https://doi.org/10.1016/0025-3227(91)90073-D)
- Hannington, M. D. (1993). The formation of atacamite during weathering of sulfides on the modern seafloor. *Canadian Mineralogist*, 31(4), 945–956.
- Hannington, M. D., De Ronde, C. E. J., & Petersen, S. (2005). Sea-Floor Tectonics and Submarine Hydrothermal Systems. *Economic Geology*, 100th Anni, 111–141.
- Hannington, M. D., Jamieson, J., Monecke, T., & Petersen, S. (2010). Modern Sea-Floor Massive Sulfides and Base Metal Resources: Toward an Estimate of Global Sea-Floor Massive Sulfide Potential. *Society of Economic Geologists Special Publication 15*, 317–338.
- Hannington, M. D., & Scott, S. D. (1988). Mineralogy and Geochemistry of a Hydrothermal Silica-Sulfide-Sulfate Spire in the Caldera of Axial Seamount, Juan de Fuca Ridge, 26, 603–625.
- Hutchin, S.R., Davidson, M.S., Brierley, J.A. and Brierley, C.L. (1986). Microorganisms in reclamation of metals. *Annual Rev. Microbiol.*, 40: 311-336.
- Jambor, J.L. (1986). Detailed mineralogical examination of alteration products in core WA-20 from Waite Amulet tailings. CANMET Division Report MSL 86-137(IR). Dept. Energy Mines Resources, Canada.
- James, R. H., & Elderfield, H. (1996). Chemistry of ore forming fluids and mineral formation rates in an active hydrothermal sulfide deposit on the Mid-Atlantic Ridge. *Geology*, 24(12), 1147–1150.
- Jamieson, J. W., Hannington, M. D., Clague, D. A., Kelley, D. S., Delaney, J. R., Holden, J. F., L. E. (2013). Sulfide geochronology along the Endeavour Segment of the Juan de Fuca Ridge. *Geochemistry, Geophysics, Geosystems*, 14(7), 2084–2099.
- Jamieson, J. W., Clague, D. A., & Hannington, M. D. (2014). Hydrothermal sulfide accumulation along the Endeavour Segment, Juan de Fuca Ridge. *Earth and Planetary Science Letters*, 395, 136–148.
- Jamieson, J., & Petersen, S. (2015). Hydrothermalism, *Springer Reference*, pp. 1–19.
- Janzen, M.P., Nicholson, R.V., Scharer, J.M. (2000). Pyrrhotite reaction kinetics: reaction rates for oxidation by oxygen, ferric iron, and for nonoxidative dissolution. *Geochim. Cosmochim. Acta* 64, 1511–1522.

- Kappel, E. S., & Ryan, W. B. F. (1986). Volcanic episodicity and a non-steady-state rift valley along northeast Pacific spreading centers: Evidence from SeaMARC I. *Journal of Geophysical Research*, 91(3), 13925–13940.
- Karsten, J. L., Hammond, S. R., Davis, E. E., & Currie, R. G. (1986). Detailed geomorphology and neotectonics of the Endeavour Segment, Juan de Fuca Ridge: New results from Seabeam swath mapping. *Geological Society of America Bulletin*, 97(2), 213-221.
- Kawasumi, S., & Chiba, H. (2017). Redox state of seafloor hydrothermal fluids and its effect on sulfide mineralization. *Chemical Geology*, 451, 25–37.  
<http://doi.org/10.1016/j.chemgeo.2017.01.001>
- Kelley, D.S., J.R. Delaney, M. Lilley, and D. Butterfield (2001a). Vent field distribution and evolution along the Endeavour Segment, Juan de Fuca Ridge. *Eos, Transactions, American Geophysical Union* 82(47): Fall Meeting Supplement Abstract OS21B-0439.
- Kelley, D.S., J.R. Delaney, and D.A. Yoerger (2001b). Geology and venting characteristics of the Mothra Hydrothermal Field, Endeavour Segment, Juan de Fuca Ridge. *Geology* 29:959–962.
- Kelley, D. S. D., Carbotte, S. M., Caress, D. W., Clague, D. A., Delaney, J. R., Gill, J. B., Wilcock, W. S. D. D. (2012). Endeavour Segment of the Juan de Fuca Ridge: one of the most remarkable places on Earth. *Oceanography*, 25(1), 44–61.
- Kelley, D. S., Delaney, J. R., & Juniper, S. K. (2014). Establishing a new era of submarine volcanic observatories: Cabling Axial Seamount and the Endeavour Segment of the Juan de Fuca Ridge. *Marine Geology*, 352, 426–450.
- Kellogg, J.P., and R.E. McDuff (2010). A hydro-graphic transient above the Salty Dawg hydrothermal field, Endeavour Segment, Juan de Fuca Ridge. *Geochemistry Geophysics Geosystems* 11, Q12001.
- Knight, R. D., Roberts, S., & Cooper, M. J. (2017). Investigating monomineralic and polymineralic reactions during the oxidation of sulphide minerals in seawater: Implications for mining seafloor massive sulphide deposits. *Applied Geochemistry*, 90(August 2017), 63–74. <http://doi.org/10.1016/j.apgeochem.2017.12.027>
- Konhauser, K. (2007). *Introduction to geomicrobiology*. Blackwell, Malden, Mass.
- Koski, R. A. (2012): Hypogene Ore Characteristics. In: Shanks, W.C. Pat, III, and Thurston, Roland, eds., 2012, *Volcanogenic massive sulfide occurrence model: U.S. Geological Survey Scientific Investigations Report 2010–5070–C*, p. 137-146.
- Lowson, R. T. (1982). Aqueous oxidation of pyrite by molecular oxygen. *Chemical Reviews*, 82(5), 461–497. <http://doi.org/10.1021/cr00051a001>

- Lilley, M. D., Feely, R. A., and Trefry, J. H. (1995). Chemical and Biochemical Transformations in Hydrothermal Plumes, Seafloor Hydrothermal Systems: Physical, Chemical, Biological, and Geological Interactions; *Geophysical Monograph*, 91, pp. 369–391.
- Lilley, M.D., J.A. Lupton, D.A. Butterfield, and E.J. Olson (2003). Magmatic events can produce rapid changes in hydrothermal vent chemistry. *Nature* 422:878–881.
- Lundgren, D.G. and Silver, M. (1980). Ore leaching by bacteria, *Annual Rev. Microbiol.* 34: 263-283.
- Mikhlin, Yu. L., Kuklinskii, A.V., Pavlenko, N.I., Varnek, V.A., Asonov, I.P., Okotrub, A.V., Selyutin, G.E., Solovyev, L.A. (2002). Spectroscopic and XRD studies of the air degradation of acid- reacted pyrrhotite. *Geochim. Cosmochim. Acta* 66, 4057–4067.
- Miki, H., Nicol, M.J., 2008a. The kinetics of the copper-catalysed oxidation of iron (II) in chloride solutions. In: Young, C., Anderson, C., Taylor, P., Choi, Y. (Eds.), *Hydrometallurgy 2008*. The Minerals, Metals and Materials Society, Warrendale, PA, USA, pp. 971–979.
- Morales M.P., Gonzalezcarreno T., Serna C.J. (1992). The formation of alpha-Fe<sub>2</sub>O<sub>3</sub> monodispersed particles in solution. *J Mater Res* 7:2538–2545
- Moncur, M.C., Ptacek, C.J., Blowes, D.W., Jambor, J.L. (2005). Release, transport and attenuation of metals from an old tailings impoundment. *Appl. Geochem.* 20, 639–659.
- Mozgova, N. N., Borodaev, Y. S., Gablina, I. F., Cherkashev, G. A., & Stepanova, T. V. (2005). Mineral assemblages as indicators of the maturity of oceanic hydrothermal sulfide mounds. *Lithology and Mineral Resources*, 40(4), 293–319. <http://doi.org/10.1007/s10987-005-0030-z>
- Mozgova, N. N., Efimov, A., Borodaev, Y. S., Krasnov, S. G., Cherkashov, G. A., Stepanova, T. V., & Ashadze, A. M. (1999). Mineralogy and chemistry of massive sulfides from the Logatchev hydrothermal field (14 degrees 45'N Mid-Atlantic Ridge). *Exploration and Mining Geology*, 8(3-4), 379-395.
- Monecke, T., Petersen, S., and Hannington, M.D. (2014). Constraints on water depth of massive sulfide formation: Evidence from modern seafloor hydrothermal systems in arc-related settings: *Economic Geology*, v. 109, no. 8, p. 2079–2101.
- Murphy P.J., Posner A.M., Quirk J.P. (1976a). Characterization of partially neutralized ferric nitrate solutions. *J Colloid Interface Sci* 56:270–283
- Navrotsky A., Mazeina L., Majzlan J. (2008). Size-driven structural and thermodynamic complexity in iron oxides. *Science* 319:1635–1638

- Nicholson, R., Gillham, R., & Reardon, E. (1988). Pyrite oxidation in carbonate-buffered solution: 1. Experimental kinetics. *Geochimica et Cosmochimica Acta*, 52(5), 1077–1085. <https://doi.org/10.1007/s00779-012-0535-0>
- Nicholson, R.V., Sharer, J.M. (1994). Laboratory studies of pyrrhotite oxidation kinetics. In: Alpers, C.N. Blowes, D.W. (Eds.), *Environmental Geochemistry of Sulfide Oxidation*. ACS Symposium Series, vol. 550, pp. 14 – 30. Washington, DC.
- Nicol, M., Miki, H., & Zhang, S. (2017). The anodic behaviour of covalite in chloride solutions: Voltammetry. *Hydrometallurgy*, 171(June), 198–205. <http://doi.org/10.1016/j.hydromet.2017.05.016>
- Nordstrom, K., D., Southam, G. (1997). Geomicrobiology of sulfide mineral oxidation, in: Banfield, J.F., Nealson, K.H. (Eds.), *Geomicrobiology: Interactions between Microbes and Minerals* Rosenberg. Reviews in Mineralogy, Min. Soc. Am, Washington, pp. 361-390.
- Ocaña M., Morales M.P., Serna C.J. (1995). The growth mechanism of  $\alpha$ -Fe<sub>2</sub>O<sub>3</sub> ellipsoidal particles in solution. *J Colloid Interface Sci* 171:85–91
- Penn R.L., Erbs J., Gulliver D. (2006) Controlled growth of alpha-FeOOH nanorods by exploiting- oriented aggregation. *J Cryst Growth* 293:1–4
- Penn R.L., Tanaka K., Erbs J. (2007). Size dependent kinetics of oriented aggregation. *J Cryst Growth* 309:97–102
- Penn, R. L., Li, D., & Soltis, J. A. (2017). New Perspectives on Mineral Nucleation and Growth, 257–273. <http://doi.org/10.1007/978-3-319-45669-0>
- Petersen, S., Lehrmann, B., & Murton, B. J. (2018). Modern Seafloor Hydrothermal Systems: New Perspectives on Ancient Ore-Forming Processes. *Elements*, 14(5), 307–312. <http://doi.org/10.2138/gselements.14.5.307>
- Plysunin, A.M., Mironov, A.G., Belomestrova, N.V., Chernigova, S.Y. (1990). Laboratory studies on gold-bearing sulfide oxidation. *Geokhimiya* 1, 51–60.
- Reed, M. H., Palandri J. (2006). Sulfide Mineral Precipitation from Hydrothermal Fluids. *Reviews in Mineralogy and Geochemistry*, 61(1), 609–631. <http://doi.org/10.2138/rmg.2006.61.11>
- Rickard, D.T. (1972). Covellite formation in low temperature aqueous solution. *Mineralium Deposita* 7:180-188
- Rimstidt, D. D., Vaughan, D. J. (2003). Pyrite oxidation: A state-of-the-art assessment of the reaction mechanism. *Geochimica et Cosmochimica Acta*, 67(5), 873–880. [http://doi.org/10.1016/S0016-7037\(02\)01165-1](http://doi.org/10.1016/S0016-7037(02)01165-1)

- Robb, L. (2005): Introduction to ore-forming processes. Blackwell, 373 pp.
- Robigou, V.R., J.R. Delaney, and D.S. Stakes (1993). Large massive sulfide deposits in a newly discovered active hydrothermal system, the High Rise Field, Endeavour Segment, Juan de Fuca Ridge. *Geophysical Research Letters* 20:1,887–1,890.
- Ryan, W.B.F., S.M. Carbotte, J.O. Coplan, S. O'Hara, A. Melkonian, R. Arko, R.A. Weissel, V. Ferrini, A. Goodwillie, F. Nitsche, J. Bonczkowski, and R. Zensky (2009). Global Multi-Resolution Topography synthesis, *Geochem. Geophys. Geosyst.*, 10, Q03014.
- Schwertmann, U. (1983). Effect of pH on the Formation of Goethite and Hematite from Ferrihydrite. *Clays and Clay Minerals*, 31(4), 277–284.  
<http://doi.org/10.1346/CCMN.1983.0310405>
- Scott, S. D., & Barnes, H. L. (1972). Sphalerite-wurtzite equilibria and stoichiometry. *Geochimica et Cosmochimica Acta*, 36(11), 1275–1295. [https://doi.org/10.1016/0016-7037\(72\)90049-X](https://doi.org/10.1016/0016-7037(72)90049-X)
- Scott S (1997) Submarine hydrothermal systems and deposits. In: *Geochemistry of Hydrothermal Ore Deposits*, Third Edition. Barnes HL (ed) Wiley, p 797-875
- Seyfried, W. E., Pester, N. J., Ding, K., & Rough, M. (2011). Vent fluid chemistry of the Rainbow hydrothermal system (36 ° N, MAR): Phase equilibria and in situ pH controls on seafloor alteration processes. *Geochimica et Cosmochimica Acta*, 75(6), 1574–1593.
- Shanks, W. C., Bischoff, J. L., & Rosenbauer, R. J. (1981). Seawater sulfate reduction and sulfur isotope fractionation in basaltic systems: Interaction of seawater with fayalite and magnetite at 200-350°C. *Geochimica et Cosmochimica Acta*, 45(11), 1977–1995.
- Shanks, W.C. (2012): Volcanogenic massive sulfide occurrence model. U.S. Geological Survey Scientific Investigations Report 2010-5070-C, 345 pp.
- Singer, P.C., Stumm, W. (1970). Acidic Mine Drainage: The Rate-Determining Step. *Science* 176, 1121-1123
- Skirrow, R., & Coleman, M. L. (1982). Origin of sulphur and geothermometry of hydrothermal sulphides from the Galapagos Rift, 86 ° W. *Nature*, 299 (September), 142–144.
- Spiess, F. N., Macdonald, K. C., Atwater, T., Ballard, R., Carranza, A., Cordoba, D., et al. (1980). East Pacific Rise: Hot Springs and Geophysical Experiment. *Geological Survey*, 207(4438), 1421–1433.
- Stakes, D., and W.S. Moore (1991). Evolution of hydrothermal activity on the Juan de Fuca Ridge: Observations, mineral ages and Ra isotope ratios. *Journal of Geophysical Research* 96:21,739-21,752.

- Steger, H.F., Desjardins, L.E., (1978). Oxidation of sulphide minerals: 4. Pyrite, chalcopyrite and pyrrhotite. *Chem. Geol.* 23, 225–237.
- Steger, H.F. (1982). Oxidation of sulfide minerals: VII. Effect of temperature and relative humidity on the oxidation of pyrrhotite. *Chem. Geol.* 35, 281–295.
- Styrt, M. M., Brackmann, A. J., Holland, H. D., Clark, B. C., Aerospace, M. M., Box, P. O., et al. (1981). The mineralogy and the isotopic composition of sulfur in hydrothermal sulfide / sulfate deposits on the East Pacific Rise, 21 ° N latitude ~ f ~ Site of = n °, 53(November 1979), 382–390.
- Sugimoto T., Muramatsu A., Sakata K., Shindo D. (1993). Characterization of hematite particles of different shapes. *J Colloid Interface Sci* 158:420–428
- Sullivan, E.A., Zajic, J.E. and Jack, T.R. (1980). The effect of chemical and biological redox reactions on the growth of *Thiobacillus thiooxidans*. In: *Biochemistry of ancient and modern environments*. Proc. 4th Int. Syrup. Environmental Biogeochem. (ISEB), Leaching Conf. (Canberra, Australia 26 Aug. 4 Sept. 1979).
- Suzuki, I. (1974). Mechanisms of inorganic oxidation and energy coupling. *Annu. Rev. Microbiol.* 28, 85–101.
- Suzuki, I., Chan, C.W., Takeuchi, T.L. (1994). Oxidation of inorganic sulfur compounds by *Thiobacilli*. In: Alpers, C.N., Blowes, D.W. (Eds.), *Environmental Geochemistry of Sulfide Oxidation ACS Symposium Series*, vol. 550, pp. 60–67. Washington, DC.
- Tivey, M. (2007). Generation of Seafloor Hydrothermal Vent Fluids and Associated Mineral Deposits. *Oceanography*, 20(1), 50–65.
- Tivey, M. K., & Delaney, J. R. (1986). Growth of large sulfide structures on the endeavour segment of the Juan de Fuca ridge. *Earth and Planetary Science Letters*, 77(3–4), 303–317.
- Tivey, M. K., & McDuff, R. E. (1990). Mineral Precipitation in the Walls of Black Smoker Chimneys: A Quantitative Model of Transport and Chemical Reaction. *J. Geophys. Res.*, 95(B8), 12617–12637. <https://doi.org/10.1029/JB095iB08p12617>
- Van der Zee C., Roberts D.R., Rancourt D.G., Slomp C.P. (2003). Nanogoethite is the dominant reactive oxyhydroxide phase in lake and marine sediments. *Geology* 31:993–996
- Vaughan D.J., Craig J.R. (1978). *Mineral Chemistry of Metal Sulfides*. Cambridge University Press, Cambridge, 512 pp
- Vaughan, D. J., & Corkhill, C. L. (2017). Mineralogy of Sulfides. *Elements*, 81–88. <http://doi.org/10.2113/gselements.13.2.81>

- Viaravanmurthy M. and Zhou W. (1995). Characterization of a transient ?2 sulfur oxidation state intermediate from the oxidation of aqueous sulfide. In *Geochemical Transformations of Sedimentary Sulfur* (eds. M. Viaravanmurthy, M. Schoonen, T. Eglinton, G. Luther, and B. Manowitz), pp. 280–292. American Chemical Society, Washington, DC.
- Von Damm, K. L. (1990). Seafloor Hydrothermal Activity: Black Smoker. *Annual Review of Earth and Planetary Sciences*, (18), 173–204.
- Walker, S. L., and Baker, E. T. (1988). Particle-size distributions within hydrothermal plumes over the Juan de Fuca Ridge, *Marine Geology*, 78, pp. 217 –226.
- Ward, J.C. (1970) The structure and properties of some iron sulphides. *Rev. Pure Appl. Chem.* 20, 175 – 206.
- Waychunas G.A., Kim C.S., Banfield J.F. (2005). Nanoparticulate iron oxide minerals in soils and sediments: unique properties and contaminant scavenging mechanisms. *J Nanopart Res* 7:409– 433
- Yuwono V.M., Burrows N.D., Soltis J.A., Do T., Penn R.L. (2012). Aggregation of ferrihydrite nanoparticles in aqueous systems. *Faraday Discuss* 159:235–245

## Chapter 2

### 2.1 Abstract

Hydrothermal vents on the seafloor are often rich in metal sulphide minerals. Seafloor massive sulfide (SMS) deposits, which form at sites of long-lived high-temperature venting, are the modern analogue for volcanogenic massive sulphide (VMS) deposits that are mined on land for Cu, Zn, Pb, Au, and Ag. However, the geological processes associated with the burial and preservation of SMS deposits are poorly constrained. This study investigates a suite of 16 massive sulphide and sulphate samples collected from inactive hydrothermal vents within the active Endeavour vent field, along the Endeavour Segment of the Juan de Fuca Ridge, northeast Pacific Ocean. Using high-resolution bathymetry as a guide, and previous work on the spatial/temporal evolution of hydrothermal activity at Endeavour, chimneys were chosen to maximize a range of time and exposure to ambient seafloor conditions. Variations in the compositions and morphology of these relict chimneys are documented through detailed investigations of collected samples using petrography, geochemistry, geochronology. Results of this work suggest that the vent mineral assemblages undergo significant mineralogical changes and reduction in mineral diversity associated with biotic and abiotic processes, and these changes occur over relatively short periods of less than 6000 years. Sulphide minerals generate spontaneous galvanic cells due to differences in rest potential of these minerals, resulting in preferential oxidation of lower rest potential minerals (e.g., chalcopyrite, sphalerite) and simultaneously preserves higher rest potential minerals (e.g., pyrite), resulting in lower mineral assemblage diversity. Vent mineral assemblages are further subject to microbial-mediated chemical reactions enhance oxidation. Secondary oxide minerals are precipitated as either abiotic or microbially mediated Fe-oxyhydr(oxides). Four new radiometric  $^{226}\text{Ra}/\text{Ba}$  ages were determined, including one 'zero-age'. These results support an increasing ageing trend of hydrothermal vents with greater distance from the spreading ridge axis.

## 2.2 Introduction

Seafloor massive sulphide (SMS) deposits on the modern seafloor are potential a future resources of Cu, Zn, Ag, and Au (Petersen et al., 2016). Our understanding of the formation of SMS deposits is based largely on the study of active hydrothermal systems. Inactive SMS deposits have been the subject of fewer studies, partly because they are more challenging to locate on the seafloor. Seafloor massive sulfide deposits are found in the ancient rock record, indicating that these deposits are preserved once they stop forming. However, the geological mechanisms that allow for prolonged SMS deposit preservation are currently not well constrained. Their preservation potential is intimately associated with abundance of metal-rich sulphide minerals of deposits, which are unstable in the presence of oxygen-rich seawater (Edwards, 2004). Metal sulphide mineral instability can result in inactive SMS deposit structures degrading over time, until their eventual collapse. Recently, microbial activity has also been linked to the preservation potential of inactive SMS deposits as certain types of microbes have been shown to thrive off of the oxidation of seafloor sulphide structures (Sylvan et al., 2012; Meier et al., 2018). Once inactive, SMS deposits are more difficult to locate, making assessment of the chemical, physical, and biological processes associated with aging of inactive deposits challenging. Therefore, the current understanding of preservation constraints of seafloor hydrothermal systems is an avenue of research to be pursued to provide further clarity on this topic.

During periods of hydrothermal inactivity metal sulphide minerals are oxidized to metal-oxides and oxyhydroxides by the influx of oxygenated seawater. Three major pathways for the aqueous oxidation of metal sulphide minerals by molecular oxygen are identified: chemical, electrochemical, and bacterial (Lowson, 1982). Chandra and Gerson (2010) highlighted that, currently, there is a general acceptance that electrochemical reactions are the primary sulphide mineral oxidation process.

In conjunction with oxidizing pathways impacting oxidation reaction rates, the effectiveness of an oxidation reaction is also influenced by the presence of existing oxidation agents and their individual efficiency. Iron(III) in oxygenated seawater has been

demonstrated in past laboratory experiments to be the most effective oxidizing agent (Chandra & Gerson, 2010). However, dissolution of a sulphide mineral followed by the release of  $\text{Fe}^{2+}$  ions and the reduction of oxygen is required to produce  $\text{Fe}^{3+}$  (Moses et al., 1987). Additionally, the oxidation of  $\text{Fe}^{2+}$  is not rapid and is stoichiometrically unfavourable, requiring more ionization energy than the oxidation of S to  $\text{S}^+$  (Rimstidt & Vaughan, 2003). As a result, the relatively slow oxidation of  $\text{Fe}^{2+}$  is the rate-limiting step in the production of  $\text{Fe}^{3+}$  (Moses & Herman, 1991). Sulphide minerals can be oxidized by  $\text{Fe}^{3+}$  when  $\text{Fe}^{2+}$  cations are adsorbed onto sulphide mineral surfaces where electrons are transferred from the sulphide mineral surface. Electron donation and acceptance occurs cyclically until the adsorbed cation is oxidized by reduced  $\text{O}_2$  from seawater (Moses & Herman, 1991).

Oxidation rates in natural environments are not yet well constrained, despite a significant number of laboratory based experimental studies (c.f. Lawson, 1982; Moses et al., 1987; Bierens de Haan, 1991; Rimstidt & Vaughan, 2003; Belzile et al., 2004; Heidel et al., 2013a; ). Oxidation rates are calculated using the number of metals ions released into solution. However, the sequestration capacity of the iron-oxyhydr(oxides) within SMS deposits makes it difficult to determine accurate rates of oxidation (Knight et al., 2017). Rate determination is further complicated by the nearly continuous electrochemical reactions occurring within SMS deposits due to their mixed metal-sulphide mineralogy and the constant presence of conductive seawater (Heidel et al., 2013a).

Experimental work to investigate the oxidation mechanics impacting polymetallic massive sulphide deposits in simulating ambient seawater conditions show that the most relevant factors to abiotic oxidation reactions are the available surface area, pH, and temperature (Belzile et al., 2004; Acero et al., 2007; Chandra & Gerson, 2010; Kimball et al., 2010). When considering the overall effect of these factors under ambient seafloor conditions, however, pH fluctuations are buffered by the surrounding seawater and temperatures are generally stable, leaving surface area as the main contributing factor to variations in the rate of abiotic oxidation (Bilenker et al., 2016). More recent work by Fallon and others (2017) highlighted that, within an individual polymetallic sulphide

deposit, the pH, mineral assemblages and modal abundances, Fe content of present minerals, and mineral grain size and surface area exposed to oxidizing conditions are also major variables influencing the rate of oxidation.

The recognition of internal electrochemical interactions occurring within polymetallic SMS deposits has since brought the formation of naturally occurring electrochemical galvanic cells to the attention of researchers. Galvanic cells form from two minerals with different rest potentials being in contact with one another in a conductive aqueous solution. The difference in rest potential of each mineral acts as a chemical driver, generating a redox reaction (Table 2.1; Mehta & Murr, 1983). The higher rest potential mineral is protected, only catalyzing the reaction as the reduced cathode, while the lower rest potential mineral becomes the anode and is preferentially oxidized. The rest potential of individual minerals are not static values; potentials can be influenced by several factors, including the conductive fluid medium, pH, temperature, and natural impurities (Fallon et al., 2017). Recent experimental work on the galvanic interactions within polymetallic sulphide deposits has led to a more detailed understanding of these natural electrochemical cells (Fallon et al., 2017; Knight et al., 2017). These studies highlight the potential impact of dissolution reactions driven by galvanic cells on the economic potential of polymetallic massive sulphide deposits.

Knight and others (2017) went on to compare the oxidation products generated by both monometallic and polymetallic SMS deposits, namely Fe-oxides and Fe-oxyhydroxides. Demonstrating that the impact of Fe-oxyhydroxide on sulphide oxidation in synthetic seawater can influence the behaviour of metals in solution. Iron concentrations present in solution decreased significantly in some experiments, which was interpreted to be linked to iron-oxyhydroxide precipitation. Copper and Zn did not demonstrate any significant trends. Overall, in experimental work for polymetallic and monometallic sulphide deposits, a greater quantity of oxide material appeared to form during polymineralic experiments in comparison to monomineralic experiments (Heidel et al., 2013b; Knight et al., 2017).

Table 2.1: Rest potential of various sulphide minerals commonly found within seafloor massive sulphide deposits.

Mineral	Rest Potential	Rest Potential
	at pH 4	at pH 7
Pyrite (FeS <sub>2</sub> )	0.66	0.45
Marcasite (FeS <sub>2</sub> )	0.63	-
Chalcopyrite (CuFeS <sub>2</sub> )	0.56	0.34
Covellite (CuS)	0.42	-
Sphalerite (ZnS)	0.46	-

Rest potential measurements at pH 4 from Majima (1969), measurements in pH 7 from Cheng and Iwasaki (1992) in distilled water.

Bacterial mats can inhabit both low temperature and inactive hydrothermal vent sites and can also impact oxidation rates. Bacteria can enhance polymineralic reactions by using the redox gradients generated by chimney oxidation as a part of their lithoautotrophic metabolism (Konhauser et al., 2007). Experimental work assessing bacterial oxidation pathways has shown that bacteria have both a direct and indirect means of affecting the rates of oxidation. The direct approach taken by Fe leaching bacteria is to affix to the sulphur portion of a target sulphide mineral. The bacteria's metabolism dissolves the sulphide's metal component as a source for energy (Bierens de Haan, 1991). Bacteria may indirectly accelerate the rates of sulphide oxidation by promoting the oxidation of Fe<sup>2+</sup> to Fe<sup>3+</sup>, which is a naturally slow reaction (Edwards et al., 2003). Under ideal conditions, Fe-oxidizing bacteria can accelerate this reaction up to 10<sup>6</sup> times (Singer & Stumm, 1970). In addition, bacteria have been shown to impact the reactive efficiency of galvanic cells and the rates of preferential dissolution in polymetallic seafloor massive sulphide deposits. Mehta and Murr (1983) determined that at 30°C, *T. ferrooxidans* and, at 55°C, thermophilic bacteria enhance the rate of metal leaching from sulphide minerals. This phenomenon was attributed to the bacteria converting sulphur into H<sub>2</sub>SO<sub>4</sub> and increasing the efficiency of the galvanic interactions between metal sulphide particles.

The challenge associated with the preservation of inactive SMS deposits is the constant exposure to an oxygen-rich environment that results in continuous reactions with exposed sulphide minerals. Prolonged exposure of metal sulphide minerals to oxygenated seawater results in the progressive oxidation of the exposed SMS deposits until an interfering preservation event occurs, such as burial by sediments or volcanic flows (Shanks and Thurston, 2012). In the absence of a preservation event, oxidation through abiotic, bacteria-mediated, or electrochemical processes results in the release of metal ions into seawater, which, depending on specific physicochemical conditions, may reprecipitate into Fe-oxyhydr(oxide) minerals. The purpose of this study is to examine the mineralogy of extinct massive sulphide chimney samples of various ages from the Endeavour vent fields to constrain mineralogic and geochemical changes associated with sulphide oxidation at the seafloor. This study varies from previous studies as we seek to explain experimental concepts through a combination of in-situ petrographic observations, their resultant geochemical trends, and  $^{226}\text{Ra}/\text{Ba}$  geochronology. We consider the impacts of dissolution effects of galvanic cells within polymetallic sulphide mineral assemblages, oxidation related passivation/armouring of reactive sulphide grain surfaces, and the effects of bacterially mediated oxide precipitation on SMS deposits. The findings of this study suggest that SMS deposits, under ambient seawater conditions, will be subject to a progressive reduction in metal sulphide diversity before total oxidative replacement or dissolution.

In this thesis, Fe oxyhydr(oxide) is used to refer to all of the orange/brown Fe(III) oxides, hydroxides and oxyhydroxides that can form as products of sulfide mineralization at hydrothermal vents. These sulfide oxidation products can display a wide range of colours and textures, and their specific mineralogical identification or chemical composition can be difficult to identify, even using X-ray diffraction, due to their poor crystallinity.

### **2.3 Geological Setting**

The Endeavour vent fields are located within an axial valley along the Endeavour segment of the Juan de Fuca Ridge. The mid-ocean ridge spreads at an intermediate-rate of 4-6 cm/year (Clague et al., 2014). The axial valley walls consist of a series of stepped

half-grabens, and active hydrothermal venting is predominantly confined to the axial valley floor and focused within five active vent fields (from south to north): Mothra, Main Endeavour, High Rise, Sasquatch, and Salty Dawg (Kelley et al., 2012; Jamieson et al., 2013). Dating of the hydrothermal deposits using  $^{226}\text{Ra}/\text{Ba}$  indicates continuous venting at the Main Endeavour Field for over 3,000 years (Jamieson et al., 2013). Overall, venting at Endeavour over a 6,000 year history has resulted in an abundance of inactive sulphide structures accumulated within the axial valley (Jamieson et al., 2014). The dominant primary mineralogy of chimneys is generally polymetallic sulphides (pyrite, marcasite, chalcopyrite, sphalerite, wurtzite, and pyrrhotite), sulphates (anhydrite and barite), and amorphous silica. The amorphous silica and barite content provide long-term structural stability to inactive chimneys at Endeavour, preserving numerous spire-like structures (Delaney et al., 1992b; Tivey et al., 1999a).

## **2.4 Methodology**

Sampling was completed using the remotely operated vehicle (ROV) ROPOS on dives R1938, R1939, R1940, and R1941 during a 2016 research cruise onboard the CCGS John P. Tully (Fig. 2.1). Sixteen sulphide samples were collected from chimneys, chimney bases, and sulphide talus fields, one sulphate sample from a chimney, and one basalt fragment from a talus field. Sampling was conducted at varied distances away from actively venting fields including High Rise, Sasquatch, far off axis along the eastern half-graben, and north of Main Endeavour field, where samples were collected from a linear transect starting at the active axial valley floor and moving westward up the axial valley wall (Fig. 2.2). The aim of the sampling strategy was to collect samples from a broad age distribution of inactive sulphide structures. Samples were collected from each site and

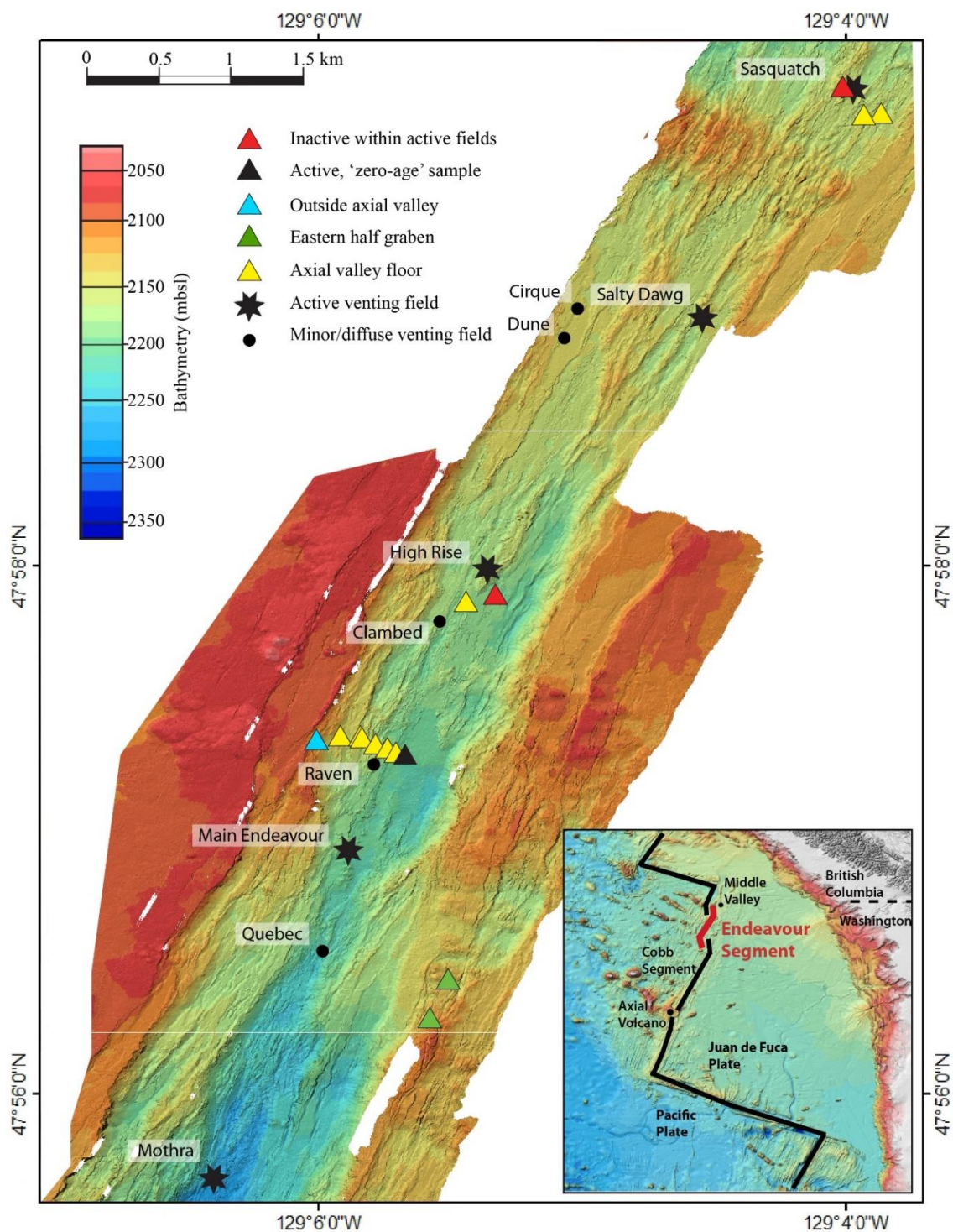


Figure 2.1: Autonomous undersea vehicle (AUV) 1-meter resolution bathymetric map of the Endeavour Segment. Indicated samples were collected for the purpose of this study. Data courtesy of the Monetary Bay Research Institute (MBARI). Inset: Regional tectonic setting of the Juan de Fuca Ridge along the west coast of North America.

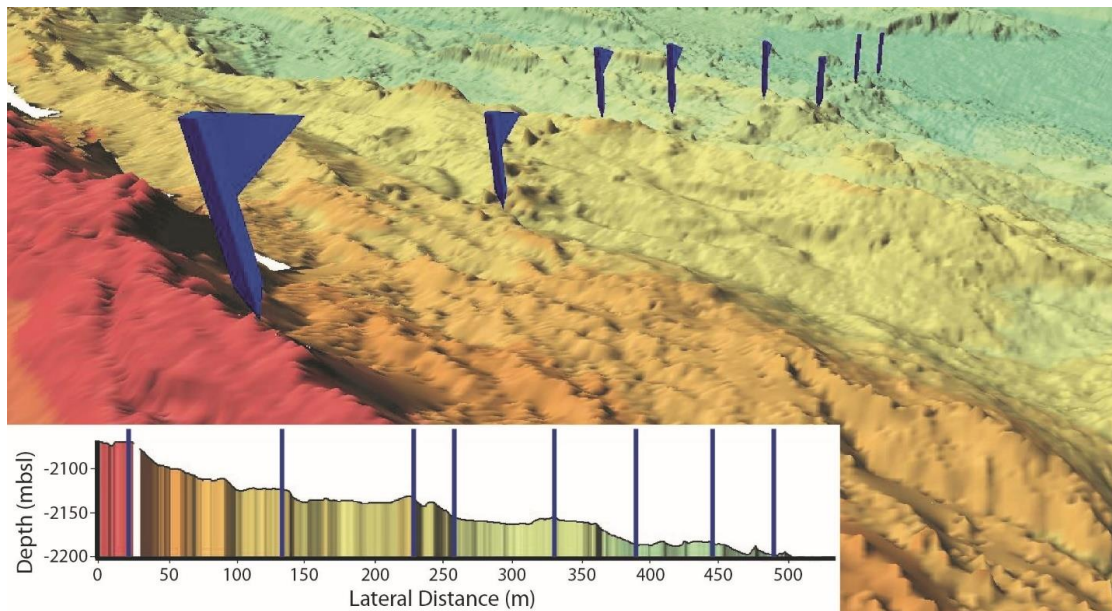


Figure 2.2: Autonomous undersea vehicle (AUV) 1-meter resolution bathymetric data 3-dimensional render of the seafloor north of Main Endeavour Field. Purple flags indicate dive R1940 sample collection transect. Data courtesy of the Monetary Bay Research Institute (MBARI). Inset: Depths of sample sites measured in meters below sea level (mbsl) and the relative distance between sites measured in meters and indicated by purple marker lines.

placed in bio-boxes onboard the ROV and brought to the surface where they were dried at ambient air temperature. Samples range from centimeters to tens of centimeters in scale, and, because of the heterogenous nature of the mineralogy of vents at that scale, the observed mineralogy and bulk chemistry may not reflect the overall composition of the vent structure associated with each sample (Jamieson et al., 2016; Lehrmann et al., 2018).

#### 2.4.1 Petrography

Thin sections were prepared at the Memorial University of Newfoundland. Slabs were impregnated with epoxy before polishing and were cut to expose a cross-section from interior to exterior of chimney walls. Thin section observations were made using a Nikon LV100NPOL microscope under both transmitted and reflected light.

### **2.4.2 Scanning Electron Microscopy (SEM)**

Carbon-coated petrographic thin sections were analyzed using a JEOL JSM-7100F scanning electron microscope (SEM) with a field emission source and silicon detector at Memorial University of Newfoundland. Spectra were analyzed using Thermo Fisher spectra analysis software. The SEM was operated using an accelerating voltage of 15 keV. Energy dispersive spectroscopy (EDS) was used to provide semi-quantitative results compared to known mineral spectra. The EDS spectra were acquired and analyzed using Thermo-Fisher software. The SEM-EDS analysis was used in conjunction with petrographic microscopy observations for petrographic confirmation and was useful for determining the composition and mineralogy of iron-oxyhydr(oxide) precipitates and replacement phases.

### **2.4.3 Whole Rock Geochemistry**

Samples were manually crushed, then powdered using a tungsten-carbide disc-mill. Powdered sub-samples were analyzed for whole-rock major and trace element analysis at Actlabs, in Ontario. Elemental abundances were collected using instrumental neutron activation analysis (INAA) and Na<sub>2</sub>O<sub>2</sub> fusion inductively coupled plasma optical emission and mass spectrometry. See section 1.3.4 for details on reported accuracy and precision.

### **2.4.4 Geochronology**

Hydrothermal barite that co-precipitated with sulphide minerals was dated using the <sup>226</sup>Ra/Ba technique. This technique relies on the decay of unsupported <sup>226</sup>Ra within barite relative to the initial amount of <sup>226</sup>Ra. Although the initial <sup>226</sup>Ra activity cannot be measured, the value can be inferred by measuring <sup>226</sup>Ra/Ba content from active, “zero-age” samples, assuming that this ratio remains constant over the lifespan of the vent field (Eq. 31) (Ditchburn et al., 2005; Ditchburn et al., 2007; Jamieson et al., 2013) :

$$t = \frac{\ln\left(\frac{N_0}{N}\right) * 1600 \text{ yr}}{\ln 2} \quad (31)$$

where  $N_0$  is the  $^{226}\text{Ra}/\text{Ba}$  of an actively forming “zero-age” vents at Endeavour, and  $N$  is the measured  $^{226}\text{Ra}/\text{Ba}$  of samples collected from extinct vent sites.

Radium-226 activities were measured at Memorial University of Newfoundland using a gamma spectrometer with a high-purity germanium well detector calibrated using BL-5, a naturally occurring uranium ore reference material. Instrument accuracy was determined by repeated measurements of IAEA-312. Crushed samples containing greater than 1% barium were sealed using epoxy for three weeks for  $^{214}\text{Pb}$  to attain secular equilibrium with  $^{226}\text{Ra}$ . Lead-214 was the primary daughter product used for determining  $^{226}\text{Ra}$  activity due to the higher detector efficiency for primary  $^{214}\text{Pb}$  spectral peaks at 352 and 295 KeV, and the presence of peak interferences at 186 keV for  $^{226}\text{Ra}$  and  $^{235}\text{U}$ . The sample analysis count time for each sample was 24 hours. The resultant gamma spectra were analyzed using a commercial software package provided by ScienTissiME Inc., which corrects for background, detector efficiency, sample volume, and matrix effects. For further details on error propagation and treatment see section 1.3.5.

## 2.5 Results

### 2.5.1 Mineralogy of samples collected from extinct chimneys

Samples for this study were collected from several inactive hydrothermal vents within and near three of the major active hydrothermal fields along Endeavour Segment. From Sasquatch field, four samples were collected from sulphide chimneys that reached up to 30 m in height and commonly have a geometry featuring wide bases and narrow towards the peak. These structures were notably different from other observed chimneys during this study, which featured more bulbous morphologies near their peaks. Within the axial valley, segmented ridges and half-graben terraces run parallel to the axial valley floor (Fig. 2.2). Sulphide structures of both pointed and bulbous morphologies occur

mostly on the valley floor but also occur along these ridges (Jamieson et al., 2014). Chimney exterior surfaces are red to orange due to the oxidation of sulphide minerals or microbially-mediated oxidation processes, or black from hydrothermal manganese precipitation (Hein et al., 1997). At the sampled inactive vent sites away from the active portion of Sasquatch field, chimneys were observed to be more weathered with sulfide rubble commonly surrounding their base. Basaltic sheet flows and pillows commonly surround the sulphide accumulations. However, in some areas, the seafloor around inactive chimneys is covered by up to 15 cm of sediment.

Southwest of Main Endeavour Field, hydrothermal vent structures located along the eastern half-graben of the axial valley, approximately 1 km from the active field, are located near the summit of a 150 meter wide basaltic mound (Fig. 2.1). The first sampled structure from the eastern half-graben was a chimney with a wide base, bulbous growth patterns, multiple distinct vent orifices at its peak and surrounded by sulphide talus (Fig. 2.3.a). Its surface is weathered reddish-brown from sulphide oxidation or black from manganese oxide precipitation. Colonization by macrofauna appears to be restricted to corals inhabiting manganese coated surfaces. The second sampling site is a tall, narrow, red to orange oxidized chimney located within the depression between two basaltic mounds where oxidized sulphide sediment accumulation partially buries oxidized boulders and sulphide talus.

North of Main Endeavour Field, nine samples were collected during a transect up the western axial valley wall (Fig. 2.2) to test the hypothesis that the degree of oxidation of inactive vents increases with increasing age of the vents away from the currently active spreading center (Jamieson et al., 2013). Sampling of the assumed youngest hydrothermal feature was from an active complex of tall (12 – 15 m), wide base and narrow peak chimneys on the valley floor with abundant bacterial mats on the surfaces of the structures (Fig. 2.3.b). Samples collected along the axial valley floor were primarily sulphide talus fragments, taken from along the flanks of inactive sulphide chimneys. These sulphide structures were commonly covered by a dusting of sediment. Fault scarps of up to 20 m form discontinuities between adjacent sampling sites along the sample

transect (Fig. 2.2). The sample collected at the base of one of the axial valley's raised fault blocks bordering the axial valley floor was in a debris field of a mixture of basalt and sulphide fragments and several centimetres of sediment infilling low points. The subsequent inactive sampling sites along the transect were located above the axial valley floor, progressing up the west valley wall. The first sampling site, an inactive chimney with sulphide rubble around its base and pillow basalts surrounding it was located approximately 60 m away from and 20 meters above the axial valley floor. This site featured a distinctive lack of corals or any other macrofauna (Fig. 2.3.c). Chimneys at this site are approximately 8 m high and some host corals and sponges. Chimneys at this site displayed increased red to orange surface colouration compared to the chimneys at the valley floor, indicating a higher degree of weathering and oxidation. The chimneys were also surrounded by abundant sulphide talus indicating more frequent structural collapse, and abundant oxidized sediments (Fig. 2.3.d). Relict chimneys located further westward, up the axial valley wall, were estimated to be up to 10 m tall. These chimneys often had sulphide debris surrounding their base and hosted sponges. The transect ends at the axial valley rim. A highly weathered relict chimney 5 m tall with an abundance of sulphide rubble, and sediment on and surrounding the sulphide structure was sampled at the axial valley rim (Fig. 2.3.e). This site also featured a significant amount of sessile faunal growth (e.g. sponges and corals) and a black manganese oxide coating.

The High Rise field was additionally surveyed and sampled. Here, several active and inactive chimneys concentrated along the axial valley floor, and range in height from ~5 to 17 m were documented. These sulphide chimneys are fragmented, blocky, bulbous, and have reddish-brown to black exterior surfaces. These chimneys formed directly on basaltic sheet flows, and are directly surrounded by rubble, and sulphide-bearing sediments.

Massive sulphide samples collected from inactive chimney edifices are primarily composed of pyrite, marcasite, chalcopyrite, and sphalerite (Table 2.2; Fig. 2.4.a-e). These samples also contain minor amounts of barite, anhydrite, amorphous silica, atacamite,

isocubanite, and secondary Cu-sulphide minerals (covellite, chalcocite; Fig. 2.4.f) which were identified through transmitted and reflected light microscopy.

Pyrite is the most abundant sulphide mineral in the massive sulphide samples (20-90% modal abundance). It is present most often as individual or intersecting euhedral cubes or as a massive crystalline aggregate (Fig. 2.4.a), but also as colloform bands (Fig. 2.4.b), and fine-grained framboids (Fig. 2.4.c). Pyrite is generally euhedral, appearing only in subhedral to anhedral form when isolated from other sulphide minerals. Marcasite, occurs in minor abundances as an epigenetic rimming feature of the primary sulphide minerals (Fig. 2.4.d) and, locally, as crystalline dendrites developing along the exterior of chimney walls (Fig. 2.4.e).

Chalcopyrite is the second most abundant sulphide mineral in the sulphide samples and occurs in minor to trace (1-14% modal abundance) amounts (Table 2.2). Chalcopyrite grains are generally subhedral to anhedral and are frequently intergrown with pyrite (Fig. 2.4.a). Additionally, chalcopyrite can be locally abundant (30 – 50% modal abundance) as subhedral and massive crystal aggregates homogeneously intergrown with isocubanite lamellae (Fig. 2.4.f) during early growth.

Secondary Cu-sulphide minerals (covellite, chalcocite) are present in nearly all recovered samples that contain chalcopyrite (Table 2.2). Of these secondary Cu sulphide minerals, covellite is the most abundant, with chalcocite occurring locally in trace amounts within Cu-rich massive sulphide samples. Both covellite and chalcocite occurs as anhedral, fine-grained mineral aggregates or as replacement features along fractures or grain boundaries between chalcopyrite (Fig. 2.4.f). In addition to covellite and chalcocite, atacamite is locally present in trace amounts as colloform bands or as a precipitate on the exterior surface of Cu-rich massive sulphide samples.

Sphalerite is the dominant Zn-sulphide mineral present in the recovered samples. Sphalerite occurs as a minor metal-sulphide phase, and, generally, is less abundant than chalcopyrite when both minerals are present. Sphalerite occurs commonly in trace amounts as fine-grained blebs intergrown within pyrite (Fig. 2.4.a). It is also present in

minor amounts (5-14% modal abundance) as anhedral crystals, often proximal to chalcopyrite grains (Fig. 2.4.a Fig. 2.5.a). In a single massive sulphide sample collected in Sasquatch field, sphalerite is the dominant metal-sulphide mineral and is composed entirely of sphalerite and amorphous silica.

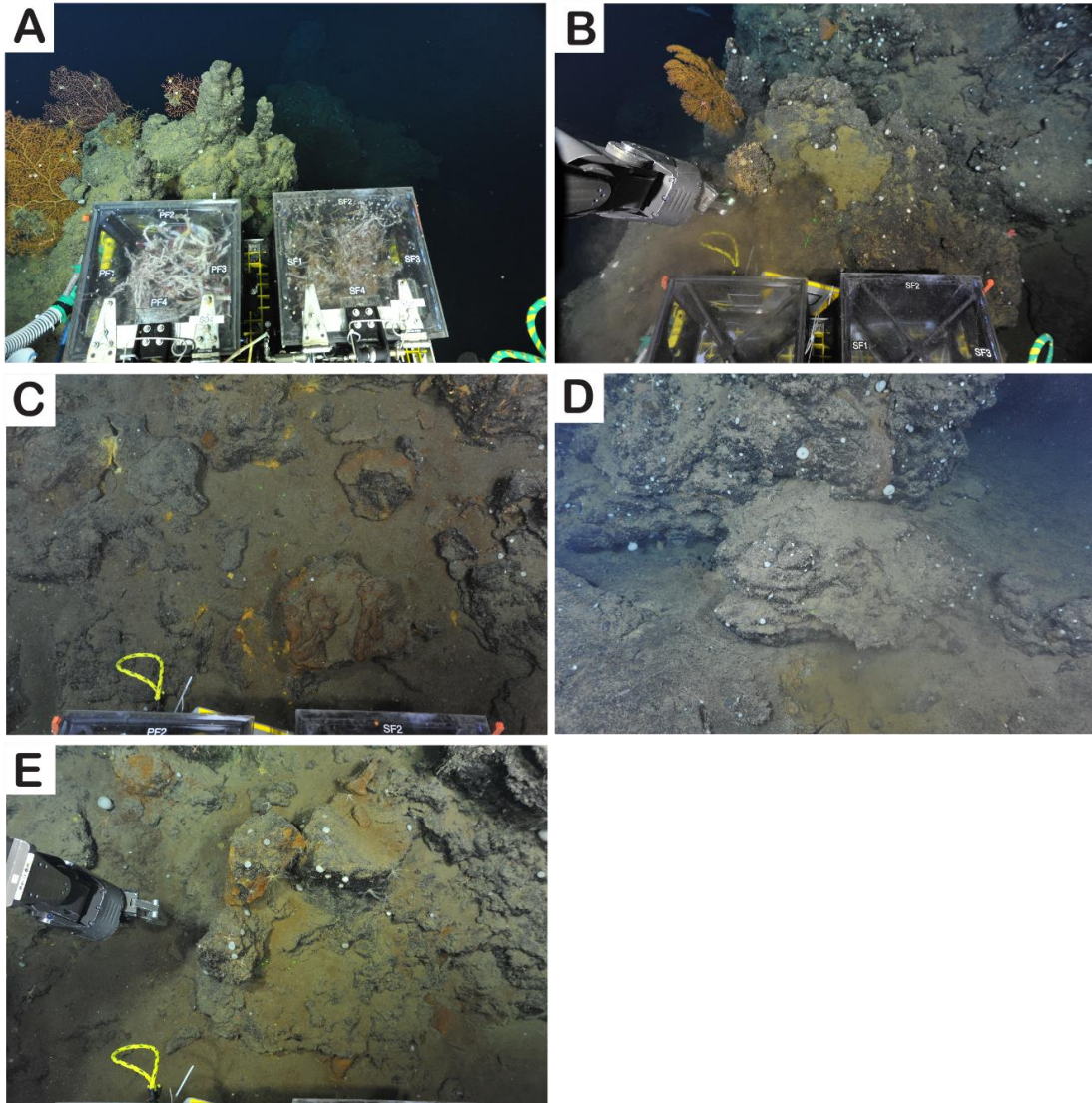


Figure 2.3: a) Zero age sample collection site north of the Endeavour vent fields; b) inactive chimney located along the western valley wall north of Main Endeavour with an estimated age of 3,000 years; c) inactive chimney located at the western rim of the axial estimated age of 5,800 years; d) inactive chimney located outside the Endeavour axial valley, sampled by Jamieson et al. (2013) using ROV Doc Ricketts, and dated to be ~5,850 years old; e) inactive chimney from the eastern half-graben with significant Fe-Mn coating, and dated to be 5,750 years old.

Table 2.2: Visually estimated modal mineral abundances in seafloor massive sulphide samples at Endeavour..

	Inactive Chimney	Chimney Base	Sulphide Talus
Pyrite	***	***	***
Marcasite	**	*	*
Chalcopyrite	**	*	**
Covelite	*	*	*
Chalcocite	*		*
Spahlerite	**		*
Atacamite	**	*	*
Fe - Oxide/ Oxyhydroxide	***	***	**

\*\*\* =>30% Mineral Abundance, \*\* = 5-30% Mineral Abundance, \* = <5% Mineral Abundance.

All collected massive sulphide samples contain trace to abundant iron-oxide and iron-oxyhydroxide precipitates (Table 2.2). The Fe-oxyhydr(oxides) occur as crusts up to 1mm thick, are light-orange to dark-red in colour, or occur as black precipitates in the presence of manganese oxides (Fig. 2.6.a). In the massive sulphide dominant thin sections, iron-oxides and oxyhydroxides occur primarily along the exterior boundary (Fig. 2.4.d). The focused occurrence of oxidation along the sample exterior margin results in an abundance of Fe-oxhydr(oxide) precipitate (10-30% modal abundance) and replacement Fe-oxyhydr(oxide) (0-10% modal abundance) being comparatively minor in volume, relative to the entire sample.

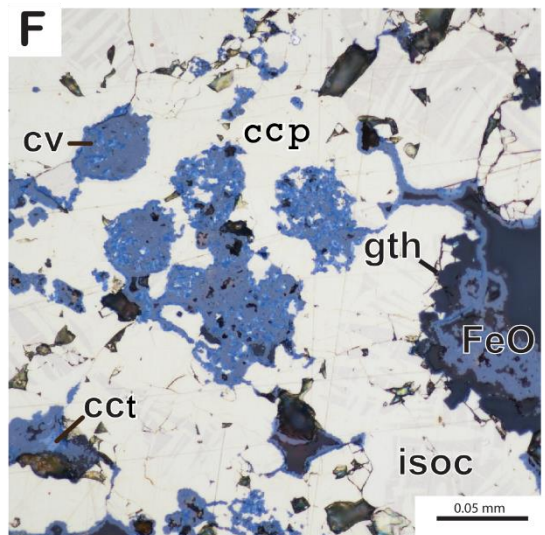
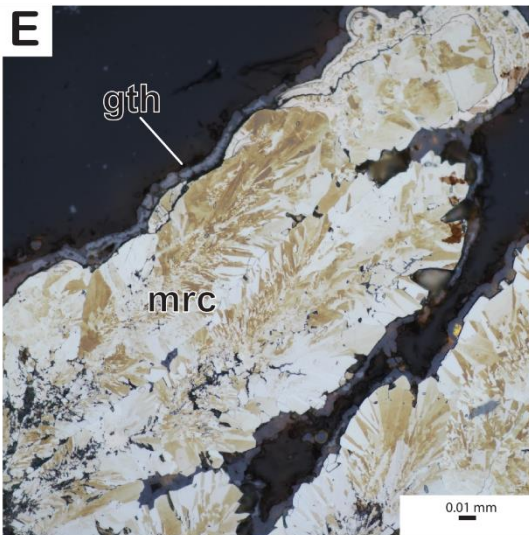
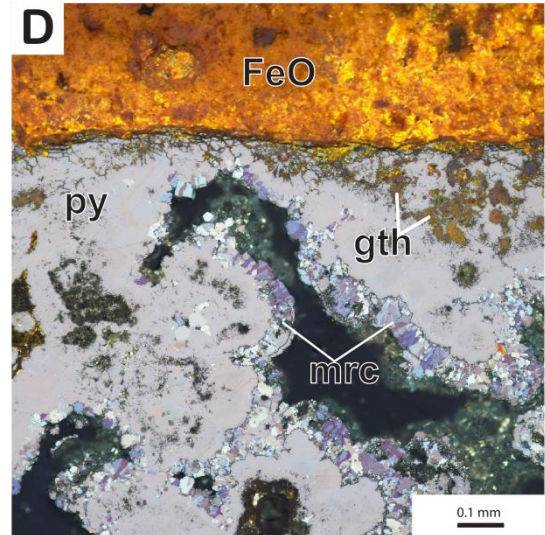
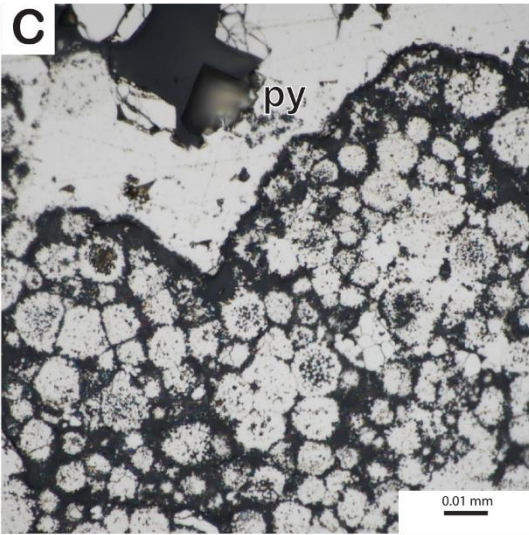
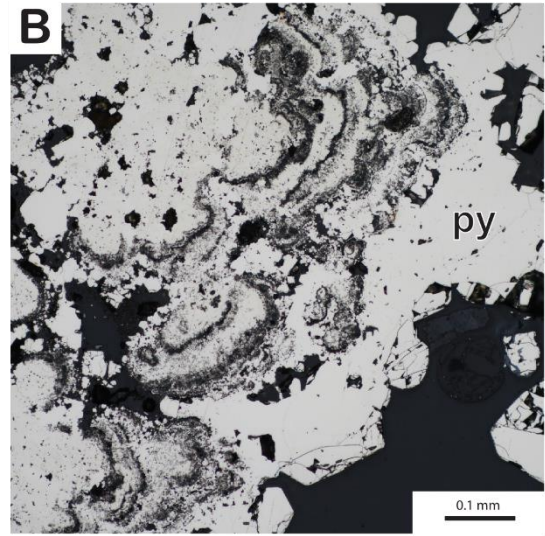
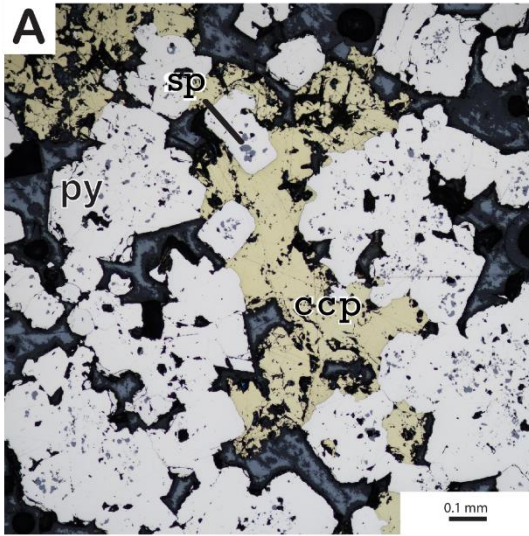


Figure 2.4: Characteristic sulphide mineral assemblages observed in plane and cross-polarized reflected light photomicrographs; (A) Euhedral-subhedral cubic pyrite (py) crystal aggregates commonly containing blebs of sphalerite (sp), with subhedral massive chalcopyrite (ccp); (B) Massive pyrite with subsequent colloform pyrite growth and further late-stage massive pyrite; (C) Framboidal pyrite (py) with later stage massive pyrite growth; (D) Exterior margin of massive sulphide composed of massive pyrite (py) with a void space lining of marcasite (mrc), and exterior surface composed of Fe-oxide (goethite (gth)) and Fe-oxyhydr(oxide); (E) Dendritic marcasite (mrc) with minor colloform banding, Fe-oxide replacement at crystal edges by goethite (gth); (F) Massive chalcopyrite (ccp) with intermixed solid solution of isocubanite (isoc) altering into secondary covellite (cv) (dark blue)/chalcocite(cct) (light blue) and oxidized into Fe-oxyhydr(oxide) precipitates.

Iron-oxyhydro(oxide) precipitates forming at the surface of sulphide mineral grains are the most abundant oxidation product occurring in the sulphide samples. This Fe-oxyhydr(oxide) precipitate is assumed to be poorly ordered ferrihydrite, however without further analysis of these precipitates, definitive identification is difficult (Hrischeva & Scott, 2007) (Fig. 2.4). In thin section, Fe-oxyhydr(oxides) that replace sulfide minerals are dark grey to black with a characteristic red-orange hue (Fig. 2.5.a, c, d).

Iron-oxyhydr(oxide) commonly occurs as a secondary replacement phase in massive sulphide samples. Goethite ( $\alpha$ -FeOOH), identified through petrographic observations and supporting semi-quantitatively scanning electron microscopy-energy dispersive spectroscopy (SEM-EDS) point analysis, partially to fully replaces entire pyrite grains. Replacement of oxidized metal sulphide minerals occurs along grain boundaries (Fig. 2.4.e, Fig. 2.5.b), fractures (Fig. 2.4.d), or less commonly because of a variation in a mineral grain's chemical potential from center to rim resulting in an atoll texture (Fig. 2.6.a). Goethite is observed to be the primary oxide phase to replace sulphide minerals, consistent with previous experimental oxidation studies (Hrischeva & Scott, 2007).

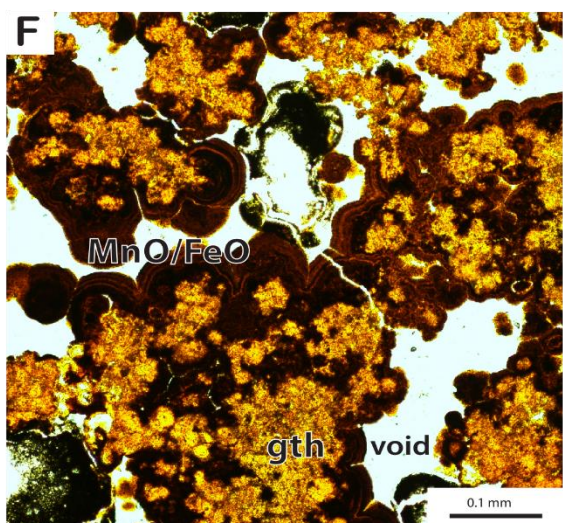
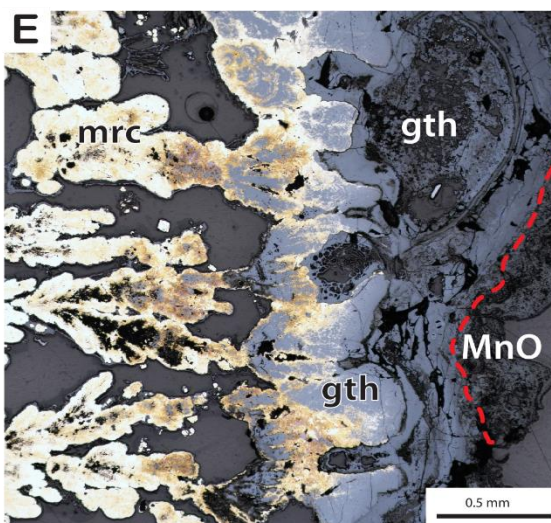
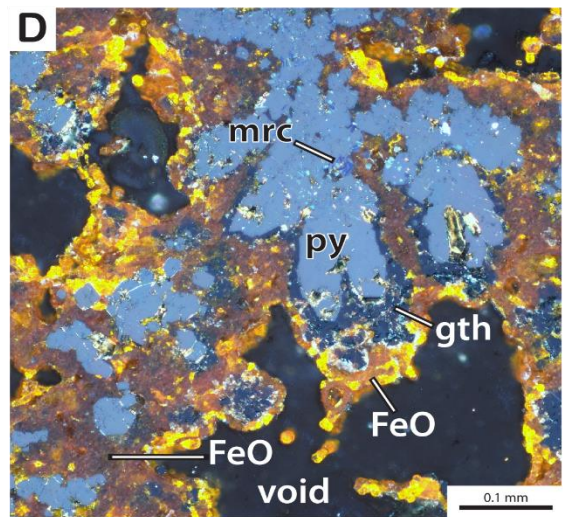
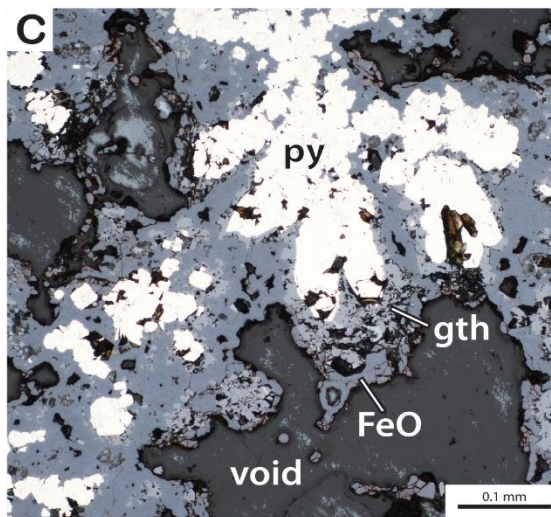
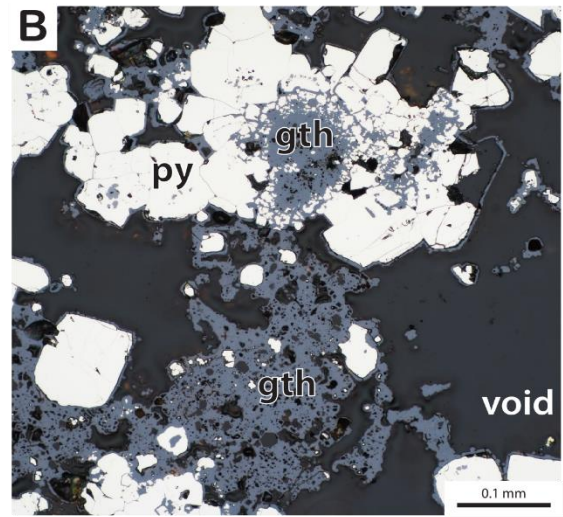
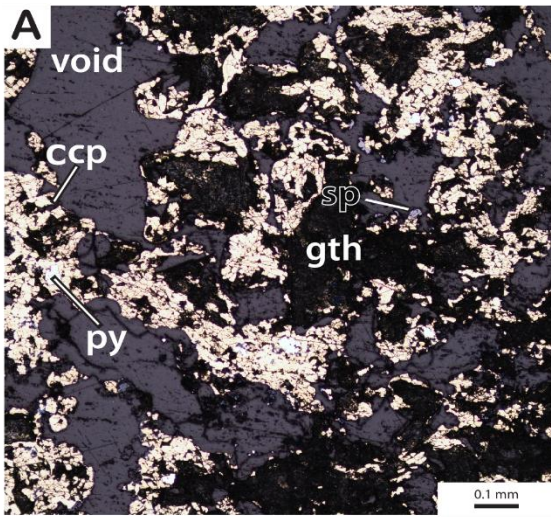


Figure. 2.5: Plain and cross-polarized photomicrographs of characteristic Fe-oxides and oxyhydroxides. Note that void spaces are infilled with epoxy. (A) Goethite (gth) replacing massive anhedral chalcopyrite (ccp) with interstitial pyrite (py) and sphalerite (sp); (B) Plain polarized reflected light photomicrograph of euhedral cubic pyrite partially replaced by goethite (grey-blue) from both at grain rims, along grain boundaries, and internally forming atoll textures; (C-D) Plan and cross-polarized reflected light photomicrographs of Fe-oxyhydr(oxide) (likely goethite) replacement of pyrite in addition to Fe-oxyhydr(oxide) (likely FeO) precipitate forming along the remnant sulphide grain boundaries; (E) Plain-polarized reflected light micrograph of dendritic marcasite (mrc) partially replaced by goethite with late-stage Fe-Mn crust precipitation (Fe-Mn ox) formed along exterior boundary; (F) Fe-oxyhydr(oxide) concretions acting as nucleation points for intermingling banding of Fe-oxyhydr(oxide) and Mn oxide (MnO) precipitates.

#### **2.5.1.1 Mineralogy of oxide and oxyhydroxide deposits**

Four highly oxidized (>50% modal abundance oxide or oxyhydroxide) samples were collected from two bases and two peaks of inactive chimneys (Table 2.2). Three of these samples are composed almost entirely (90-99% modal abundance) of a combination of Fe-oxyhydr(oxide) precipitates (Fig. 2.5.a). One sample, collected from a chimney's base north of Main Endeavour field, is composed of locally banded Fe-oxyhydr(oxide) and Mn oxide (Fig. 2.5.e,f).

In contrast to the mm-scale oxide crusts that characterize much of the oxide precipitates, filament, rod, and concretion network microstructures are also present in some samples, and, in previous studies, have been linked to microbial processes (Juniper et al., 1988). These Fe-oxyhydroxide networks are grey-red under reflected light and translucent red orange under transmitted light (Fig. 2.6).

#### **2.5.1.2 Mineral Divisions inferred from Geochemical Enrichment**

Samples can be divided into two distinct compositional groups based a combination of mineral abundances and whole-rock geochemical data (Table 2.3; Fig. 2.7). Group 1 is composed primarily of Mn and bacteria related and abiotic Fe-oxyhydr(oxides), barite, and lesser amounts of pyrite, marcasite, and anhydrite. Group 2 is composed of primarily of metal sulphide minerals (pyrite, marcasite, chalcopyrite, and sphalerite), secondary copper minerals (covellite, chalcocite, isocubanite, and atacamite),

lesser abundances of Fe oxide and hydroxide phases; and minor amounts of barite and amorphous silica.

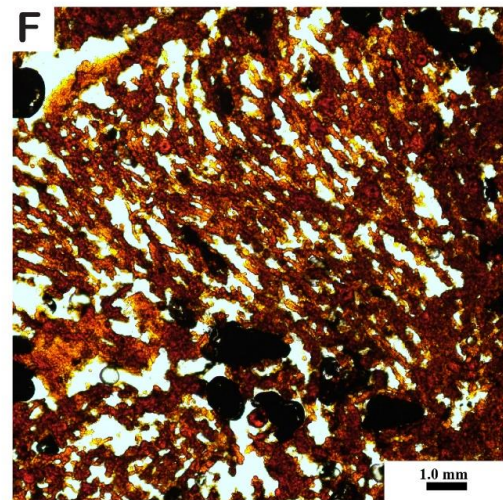
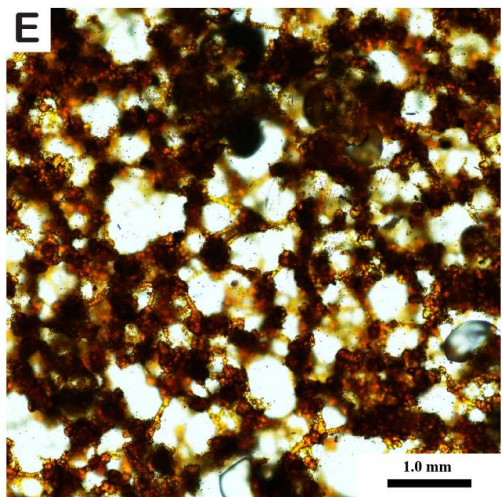
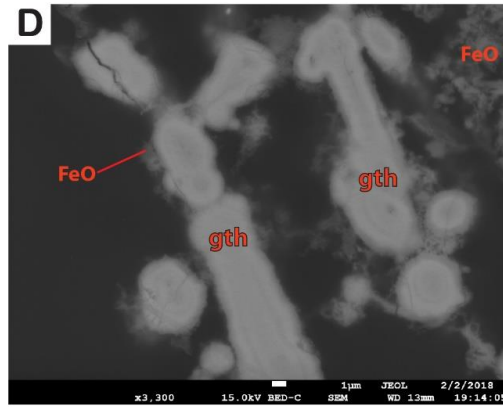
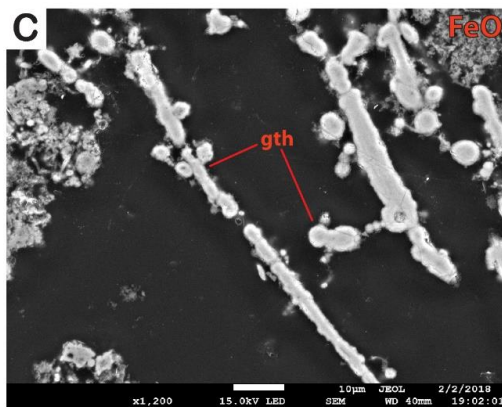
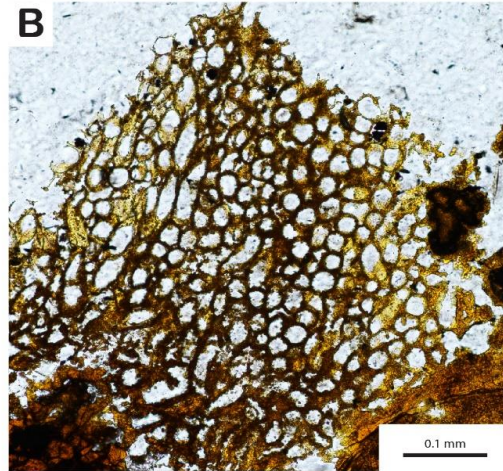
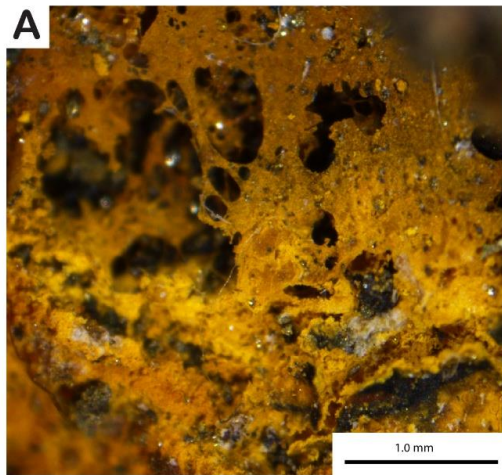


Figure 2.6: (A) Millimetre scale image of Fe-oxyhydr(oxide) on the exterior surface of a massive sulphide sample; (B) Plain polarized transmitted light photomicrograph of a pristine bacterial generated goethite (gth) filament network at the outer surface of a heavily oxidized sample; (C) Scanning electron microscope backscattered image of goethite Fe-oxyhydr(oxide) filaments and concretions with surficial Fe-oxyhydr(oxide) precipitation (FeO); (D) Scanning electron microscope image of abiotic Fe-oxyhydr(oxide) precipitation developing along the surface of bacteria-related goethite filament structures.

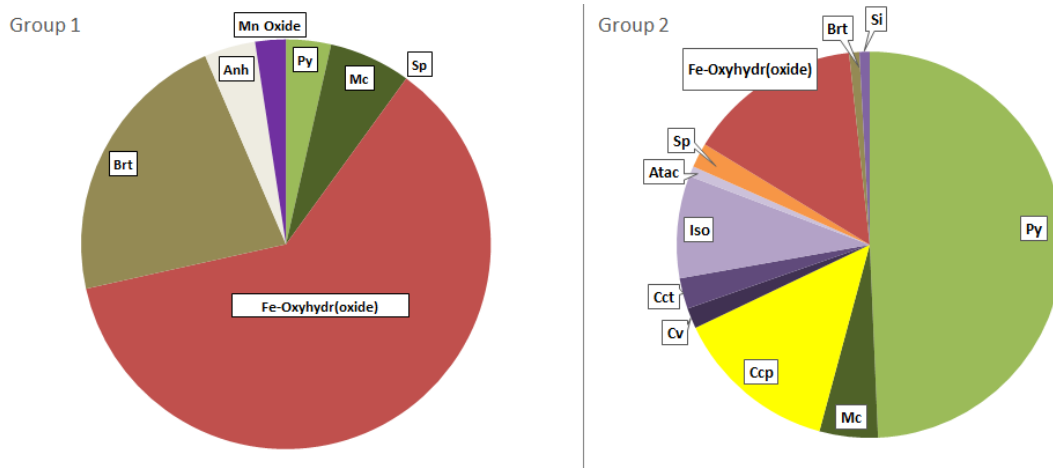


Figure 2.7: Graphic representation of the average mineral composition for the two sample sub-sets, based on petrographic observations. Group 1 is relatively enriched in Al, Ba, Mg, Mn, Ni, Pb, Si, Sm, U, and V, whereas group 2 is relatively enriched in Co, Cu, Fe, and Mo. Mineral abbreviations: Anh = Anhydrite, Mn Oxide = Manganese Oxide mineral, Py = Pyrite, Mc = Marcasite, Fe-Oxyhydr(oxide) = Iron-Oxyhydr(oxide) mineral, Brt = Barite, Si = Amorphous Silica, Ccp = Chalcopyrite, Cv = Covellite, Cct = Chalcocite, Iso = Isocubanite, Atac = Atacamite, and Sp = Sphalerite.

### 2.5.2 Scanning Electron Microscope- Energy Dispersive Spectroscopy Analysis

Scanning electron microscope – energy dispersive spectroscopy (SEM-EDS) was used to support petrographic observations for identification of sulphide and oxide minerals. Several point analyses on targeted abiotic Fe-oxyhydr(oxide) precipitates, bacterial oxyhydr(oxide) structures, and massive crystalline bands provided a measure of Fe/O (Fig. 2.8). Using these values, we were able to confirm that goethite (Fe/O = ~0.5) is

the major oxide phase replacing existing sulphide minerals, and FeO (Fe/O = ~1) is the dominant abiotic precipitate Fe-oxhydr(oxide) phase (Fig. 2.5).

Analysis of the abiotic Fe-oxhydr(oxide) precipitates by SEM-EDS indicated elevated concentrations of Si, P, S, Cl, and Cu. The Fe-oxhydr(oxides) with morphologies associated with microbially activity contained similar enrichments in Si, P, S, Cl, but also Ca, Al, and Mg, and lesser Cu. Presumed ferromanganese oxide phases identified through petrographic observations were also confirmed through detection of high amounts of Mn using SEM-EDS (Fig. 2.5.f; Fig. 2.8.d).

### **2.5.3 Major and Trace Element Lithochemistry**

Two distinct geochemical groups, plus a single Au-Ag-Zn rich, Fe-poor outlier were identified from the whole rock geochemistry. In general, group 1 contains higher Al, Ba, Mg, Mn Ni, Pb, Si, Sm, U, and V, and group 2 contains higher Co, Cu, Fe, and Mo (Table 2.3).

There is a relationship of co-enrichment between elements associated with seawater exposure (U, V, and Mn; Fig. 2.9). Typical high-temperature sulphide samples (group 2) generally have lower concentrations of U, V than the oxidized, Fe-oxhydr(oxide) dominant samples (group 1), consistent with the oxidized samples having greater long-term exposure to seawater (Fig. 2.9).

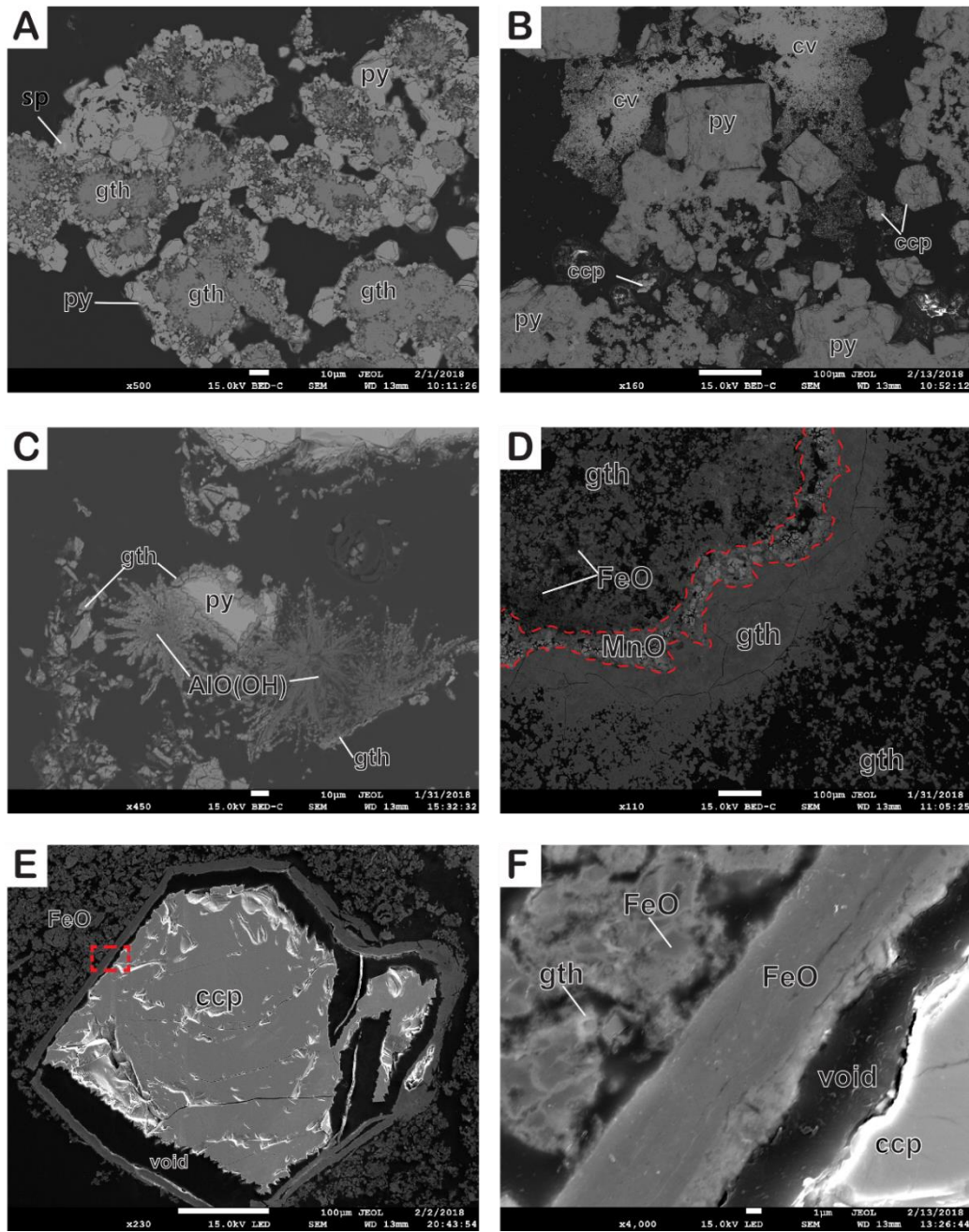


Figure 2.8: SEM-EDS analysis of massive sulphide, and Fe-oxyhydr(oxide) samples from the Endeavour Segment (A) Massive pyrite with sphalerite (sp) bleb intergrowths. Oxide dissolution/oxidation (gth) of pyrite (py) forming "atoll" textures; (B) Alteration of chalcopyrite (ccp) into covellite (cv) (loss of Fe, S; increase in Cu) to Cu-containing Fe-oxyhydr(oxide); (C) Pyrite replacement by goethite, in addition to replacement of the Fe<sup>3+</sup> cation Al<sup>3+</sup> forming AlO(OH); (D) Iron-oxyhydr(oxide) of microbial origin, with composition ranging from massive to porous and branching, in addition to a defined band of manganese oxide (MnO); (E) Iron-oxyhydr(oxide) precipitate exterior of a massive sulphide sample with an isolated chalcopyrite grain with high relief oxidized boundary; (F) Detailed perspective of abiotic Fe-oxyhydr(oxide) precipitate armouring isolated chalcopyrite grain, confirming that it is compositionally similar but texturally varied from surrounding oxides.

Table 2.3: Major and trace element analysis of seafloor samples collected throughout the Endeavour vent fields.

Analyte Symbol	Ag	Al	Au	Ba	Co	Cu	Fe	Mg	Mn	Mo	Ni	Pb	Si	Sm	U	V	Zn
Unit Symbol	ppm	%	ppb	ppm	ppm	ppm	%	%	ppm	ppm	ppm	ppm	%	ppm	ppm	ppm	ppm
Detection Limit	2	0.01	2	20	0.1	2	0.01	0.01	3	2	10	0.8	0.01	0.01	0.1	5	10
Analysis Method	INAA	FUS-MS	INAA	INAA	INAA	FUS-MS	INAA	FUS-MS	FUS-MS	INAA	FUS-MS	FUS-MS	FUS-MS	INAA	FUS-MS	FUS-MS	INAA
R1938-Rck-20	<b>108</b>	0.29	<b>1230</b>	1040	15.8	19700	6.25	0.06	161	6	20	388	5.38	0.16	3.6	55	<b>454000</b>
<b>Group 1</b>																	
R1938-Rck-16	100	<b>0.38</b>	385	<b>147000</b>	30.8	2480	8.32	<b>0.02</b>	<b>1040</b>	9	<b>20</b>	<b>1170</b>	<b>18.6</b>	<b>0.14</b>	<b>3.1</b>	<b>33</b>	16400
R1940-Rck-1	1	<b>0.49</b>	49	<b>137000</b>	18.5	1	22.9	<b>0.33</b>	<b>8060</b>	14	<b>190</b>	<b>502</b>	<b>3.53</b>	<b>0.89</b>	<b>10.1</b>	<b>322</b>	1850
R1940-Rck-5	1	<b>0.33</b>	111	<b>94500</b>	21.3	2590	29.4	<b>0.21</b>	<b>9680</b>	9	<b>50</b>	<b>1090</b>	<b>4.82</b>	<b>0.48</b>	<b>8.1</b>	<b>214</b>	4740
R1940-Rck-9	1	<b>0.13</b>	1	<b>540</b>	40.2	1480	26.6	<b>0.62</b>	<b>78600</b>	10	<b>80</b>	<b>225</b>	<b>6.39</b>	<b>0.38</b>	<b>2.6</b>	<b>82</b>	7940
R1939-Rck-13	79	<b>0.21</b>	450	<b>11700</b>	199	13300	38.3	<b>0.08</b>	<b>5490</b>	5	<b>80</b>	<b>1380</b>	<b>2.47</b>	<b>1.14</b>	<b>2.6</b>	<b>139</b>	36300
Average	36.4	<b>0.308</b>	199	<b>78148</b>	62	3970.2	25.1	<b>0.252</b>	<b>20574</b>	9.4	<b>84</b>	<b>873.4</b>	<b>7.162</b>	<b>0.61</b>	<b>5.3</b>	<b>158</b>	13446
<b>Group 2</b>																	
R1941-Rck-13	34	0.01	161	370	<b>71.3</b>	<b>10400</b>	<b>50.9</b>	0.005	224	<b>437</b>	20	542	0.04	0.005	0.3	2.5	21900
R1941-Rck-12	13	0.07	38	10	<b>51.4</b>	<b>69900</b>	<b>48.5</b>	0.01	47	<b>324</b>	10	22.1	0.16	0.005	0.6	12	3460
R1938-Rck-21	38	0.03	240	3870	<b>759</b>	<b>105000</b>	<b>37.2</b>	0.02	1430	<b>97</b>	20	327	0.71	0.23	3.9	42	31600
R1938-Rck-22	1	0.01	127	270	<b>726</b>	<b>5420</b>	<b>39.3</b>	0.05	28	<b>80</b>	270	102	0.82	0.005	0.7	2.5	2160
R1940-Rck-4	1	0.05	117	450	<b>239</b>	<b>30900</b>	<b>43.5</b>	0.06	108	<b>41</b>	20	212	0.16	0.005	1.8	30	2290
R1939-Rck-14	6	0.03	200	680	<b>364</b>	<b>47800</b>	<b>41.8</b>	0.01	36	<b>196</b>	20	115	0.09	0.07	6.5	16	470
R1940-Rck-2	6	0.08	70	260	<b>100</b>	<b>54900</b>	<b>41.3</b>	0.12	115	<b>97</b>	20	152	0.25	0.005	0.4	2.5	920
R1940-Rck-6	1	0.005	63	190	<b>39.7</b>	<b>3160</b>	<b>45.3</b>	0.02	81	<b>126</b>	10	151	0.25	0.1	2.8	2.5	2630
R1940-Rck-7	8	0.07	242	10	<b>57.2</b>	<b>664</b>	<b>53.3</b>	0.01	105	<b>313</b>	20	309	0.17	0.005	0.6	15	1890
R1940-Rck-8	7	0.03	65	10	<b>43</b>	<b>10100</b>	<b>52.9</b>	0.005	70	<b>315</b>	10	122	0.18	0.005	0.5	6	3170
Average	11.5	0.0385	132	612	<b>245</b>	<b>33824</b>	<b>45.4</b>	0.031	224.4	<b>203</b>	42	205.41	0.283	0.04	1.81	13.1	7049

Bolded values denote the elements enriched for the designated sample sub-set.

Analysis techniques used: INAA: Induced Neutron Activation Analysis, and FUS-MS: Sodium Peroxide Fusion Mass Spectrometry.

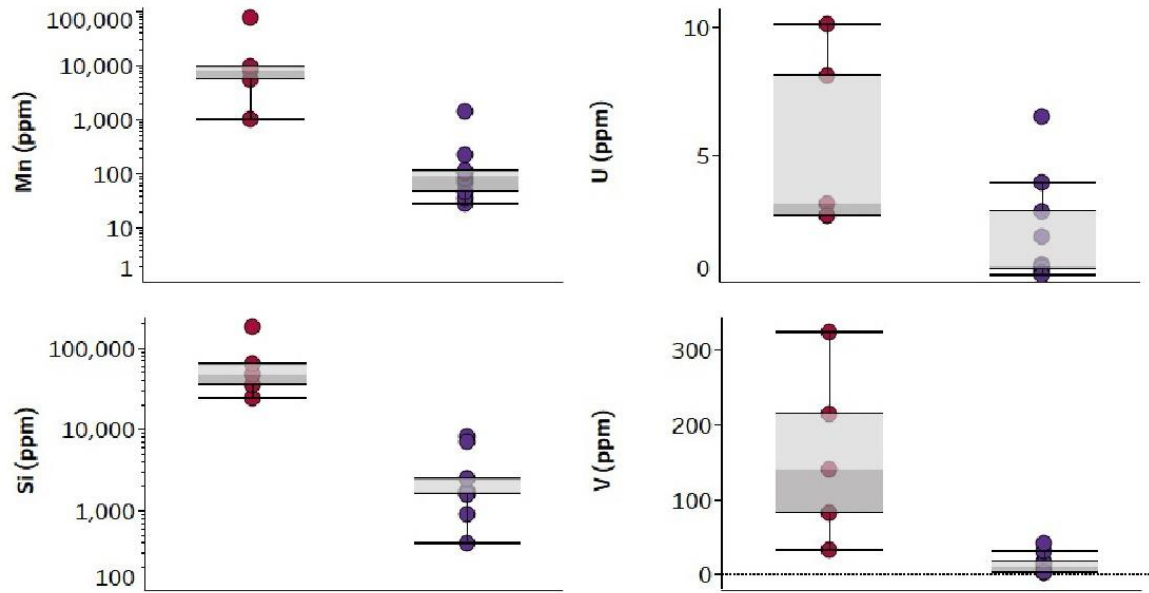


Figure 2.9: Box and whisker plot of contrasting seawater sourced elemental abundances between heavily oxidized (group 1 - red symbols) and typical seafloor massive sulphide (group 2 – purple symbols) samples. Boxes represent the middle 50% of data, box shading indicates median value, and the whiskers represent 1.5 times the interquartile range.

#### 2.5.4 Geochronology

Four samples contained sufficient Ba (>~1 wt.%) to be dated using the  $^{226}\text{Ra}/\text{Ba}$  method (Table 2.4). Sample ages are plotted alongside ages determined by Jamieson et al. (2013; Fig. 2.10). The study by Jamieson et al. (2013) developed the initial  $N_0$  value for the Endeavour vent fields with a value of 1275  $^{226}\text{Ra}/\text{Ba}$  Bq/kg\*Ba wt.%. This study adds a new data point that maintains a statistical significance ( $r^2 = 0.9965$ ) for the overall correlation of zero-age ( $N_0$ ) samples while significantly increasing the range in Ba wt.% for the zero-age samples (Fig. 2.11).

Table 2.4:  $^{226}\text{Ra}/\text{Ba}$  Geochronology results of massive sulphide samples collected from inactive locations along the Endeavour Segment.

Sample	Field	Latitude	Longitude	Ba (wt.%)	$^{226}\text{Ra}$ Activity (Bq/kg)	Age* (years)
R1938-R-16	Sasquatch	47.997005	-129.066782	14.7 ± 0.76	15814.5 ± 496.9	629 ± 45
R1939-R-13	E. Half Graben	47.940647	-129.091813	1.17 ± 0.06	136.9 ± 4.8	5749 ± 140
R1940-R-1	N. of MEF	47.954902	-129.094518	13.7 ± 0.70	19523.5 ± 613.4	''Zero age''
R1940-R-5	N. of MEF	47.955500	-129.096393	9.45 ± 0.49	4757 ± 149.9	2382 ± 50

\*Age uncertainties calculated by propagation of uncertainties from input variables (see section 1.3.5).

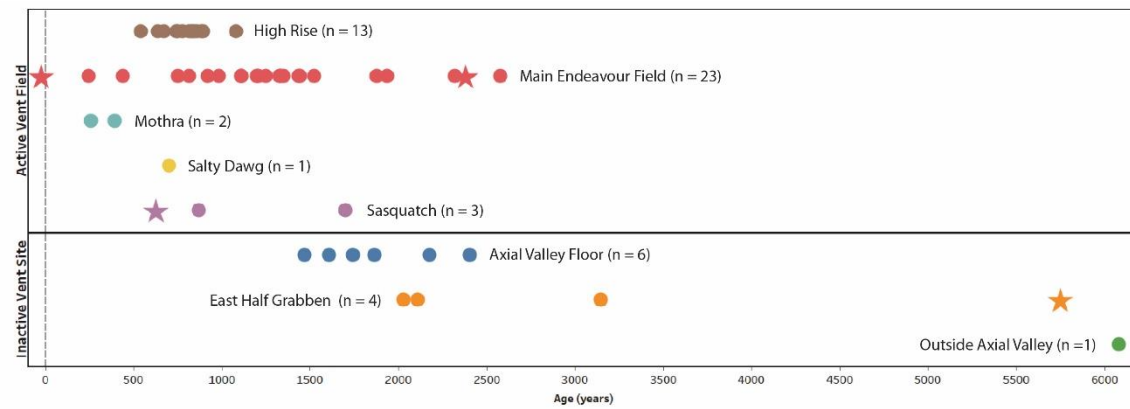


Figure 2.10: Age distribution of hydrothermal sulphide samples from the Endeavour Segment, divided into active vent field samples (top) and inactive vent site samples (bottom). Samples introduced in this study are represented by star markers and previous data collected by Jamieson et al. (2013) are represented by circle markers. Of the four new samples introduced to this dataset one sample is a new “zero-age” sample. Two samples collected from inactive structures within active venting fields are relatively young (<3,000 years), and one sample, collected from an inactive sulphide mound on the eastern half-graben, is relatively old (~5,500 years). Figure modified from Jamieson et al. (2013).

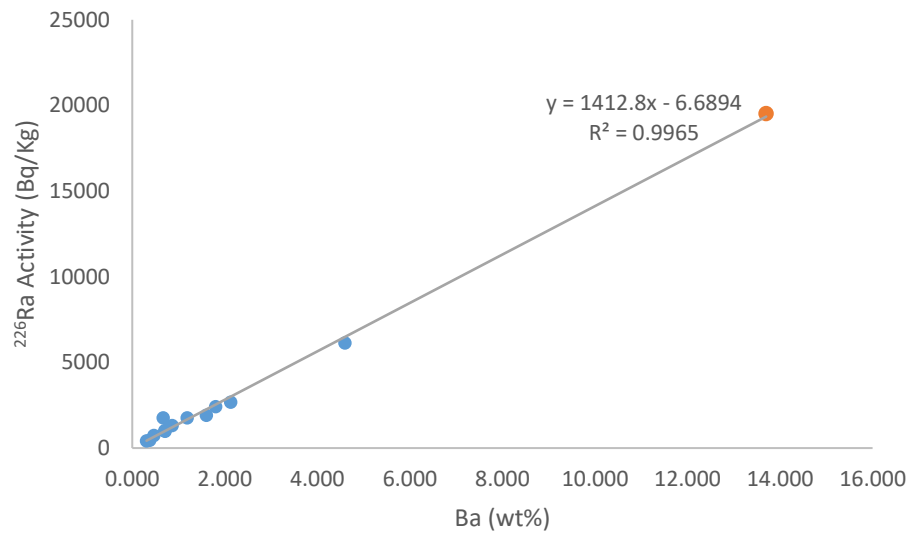


Figure 2.11: Plot of  $^{226}\text{Ra}/\text{Ba}$  activity vs. Ba wt.% from collected “zero-age” samples from the Endeavour Segment. Samples collected by Jamieson et al. (2013) are denoted by blue markers; this study denoted with an orange marker. A correlation line is plotted for all existing data maintaining an  $r^2$  value of 0.9965 denoting a statistically significant correlation.

## 2.6 Discussion

### 2.6.1 Oxidation of sulphide minerals

The cessation of venting of hot, reduced hydrothermal fluids results in exposure of sulfide deposits to oxygenated seawater. Under oxidizing conditions, sulphide minerals are chemically unstable and subject to two major chemical weathering processes: oxidation and dissolution (Moses et al., 1987). Oxidation occurs when the sulphide minerals react with a combination of aqueous  $\text{Fe}^{2+}$  ions and oxygen from seawater (Lowson, 1982). Oxidation rates increase with temperature, acidity, and the presence of a more reactive oxidizing agent (e.g.,  $\text{Fe}^{3+}$ ; Chandra & Gerson, 2010). In oxidizing and acidic conditions, pyrite releases  $\text{Fe}^{2+}$  ions that are oxidized by available  $\text{O}_2$  to form  $\text{Fe}^{3+}$  (Eq. 33). The  $\text{Fe}^{3+}$  reprecipitates as iron-oxyhydroxides such as ferrihydrite and goethite (Eq. 34; Singer & Stumm, 1970; Belzile et al., 2004; Gartman et al., 2014).



These oxidation products have the additional effect on their respective sulphide mineral assemblage of creating precipitation barriers or “armour” that inhibit further oxidation (section 2.6.1.1). The oxidation rates of massive sulphide assemblages are further complicated by the mixed mineral assemblages that form galvanic cells between low and high rest potential minerals, thereby accelerating oxidation rates (section 0). The formation of both galvanic cells and the production of oxidation products are both further enhanced by the catalyzing presence of Fe-oxidizing bacteria (section 2.6.1.3). These bacteria accelerate the galvanic interactions between metal sulphide minerals and the production of Fe- oxyhydr(oxides).

#### **2.6.1.1 Abiotic oxidation and metal sulphide armouring**

Iron--oxyhydr(oxide) crusts form on the exterior surface of seafloor massive sulphide deposits (Fig. 2.3). These crusts can range from one to several millimetres thick, depending on the formation conditions available. Observations from samples at Endeavour agree with previous studies that suggest that Fe-oxyhydr(oxide) crusts limit the available surface area for further oxidation reactions (Fig. 2.4.d; Fig. 2.8.e) (i.e. Bilenker et al., 2016). However, evidence of continuous dissolution and replacement of sulphide minerals within the interior of Fe-oxyhydr(oxide) crusts (Fig. 2.4.d), indicate that oxyhydr(oxide) crusts do not entirely prevent oxidation processes from occurring (Bilenker et al., 2016).

From petrographic analysis, abiotic oxidation products appear as iron-oxyhydr(oxide) precipitates and crystalline replacement rims on grains of pyrite, chalcopyrite, and sphalerite (Fig. 2.5, Fig. 2.8). Numerous experimental studies of monomineralic pyrite oxidation have documented the complex multistep chemical transformation taking place in acidic (e.g., acid mine drainage) and circumneutral (e.g., seawater) pH conditions (Lowson, 1982; Rimstidt & Vaughan, 2003; Gartman & Luther,



quickly than covellite under ambient seawater conditions (Fullston et al., 1999). The conditions of formation of both covellite and chalcocite suggest that these secondary sulphide minerals form during low-temperature hydrothermal conditions, but will then also be subject to oxidation and dissolution at ambient seawater conditions, with chalcocite oxidizing at a faster rate than covellite (Fig. 2.4.f). Because covellite and chalcocite are readily oxidized in seawater, these minerals are typically anhedral and typically exhibit significant dissolution textures (Fig. 2.12, Fig. 2.13). The occurrence of covellite or chalcocite within massive sulphide samples with otherwise little to no oxidation can be used as an indication that the sample is relatively young.

Table 2.5: Mineral abundance variation of massive sulphide samples grouped by primary and secondary mineral phases and compared by estimated ages.

	<b>Young Samples</b> (<400 m from central reference line)	<b>Old Samples</b> (>400 m from central reference line)
<b>Primary Mineralogy</b>		
Pyrite	****	****
Marcasite	** (L)	***
Chalcopyrite	***	*
Sphalerite	****	* (L)
Barite	* (L)	* (L)
Amorphous Silica	*** (L)	* (L)
<b>Secondary Mineralogy</b>		
Fe-Oxyhydr(oxides)	***	****
Covellite	*	* (L)
Chalcocite	*	
Isocubanite	** (L)	
Atacamite	*	
Ferromanganese Oxides		* (L)
<b>Total number of phases</b>	<b>11</b>	<b>9</b>

Age classifications were defined by relative distance from a central reference line in Fig. 2.15. Mineral abundances are denoted by: \* = trace (1-4 %), \*\* = minor (5 – 14%), \*\*\* = major (15 – 29%), \*\*\*\* = abundant (>30 %), and (L) = local occurrence. Abundance estimates are approximated visual estimations.

### **2.6.1.2 Influence of galvanic cells on sulphide mineral oxidation**

A comparison of the number of different minerals within hydrothermal samples from inactive vents to the degree of oxidation (and therefore age) reveals a trend towards a reduction in the diversity of mineralogy over time (Table 2.5). This trend is consistent with our observation of 1) absence of sulphide minerals with lower resting potentials in old, highly oxidized samples, and 2) when minerals with low resting potentials are still present, they exhibit significant oxidation and/or dissolution textures (Fig. 2.12). This is consistent with previous experimental results that show that preferential oxidation consistently targets low rest potential metal sulphide minerals when multiple sulphide minerals are present (Mehta & Murr, 1983). Pyrite is the most common sulphide mineral to act as a cathode in any galvanic cell reaction due to its high rest potential (Kwong et al., 2005; Heidele et al., 2013b), and commonly occurs as a euhedral or minimally oxidized mineral phase in polymineralic samples that otherwise exhibit high degrees of oxidation and dissolution (e.g., Fig. 2.4.a vs. Fig. 2.4.b). In contrast, chalcopyrite and sphalerite have lower rest potentials and act as anodic minerals and are subject to preferential dissolution when in contact with pyrite or marcasite (Fig. 2.12.b). Chalcopyrite and sphalerite appear to be unaffected by the presence of each other, and commonly share grain boundaries with no evidence of oxidative interactions (Fig. 2.13.b; Knight et al., 2017). Galvanic reactions between pyrite and covellite under experimental conditions show that mineral rest potentials are sensitive to changes in pH (Sato, 1992). In this case, at low pH conditions, pyrite is the cathode, whereas at high pH covellite is the cathode. For samples from inactive vents at Endeavour, covellite primarily occurs as fine-grained anhedral crystal aggregates near subhedral to euhedral pyrite cubic grains (Fig. 2.12.a, Fig. 2.13.d, f). However, the reaction dynamics between this mineral set is complicated by the precipitation of Fe-oxyhydr(oxides) such as goethite. While it could be hypothesized that Fe-oxyhydr(oxide) precipitation could establish an electrochemical bridge between pyrite and covellite, this study shows no evidence of this (Fig. 2.12.d, Fig. 2.13.d).

For a galvanic reaction to occur, previous studies have indicated that contact between the two minerals is required (Knight et al., 2017). Based on our observations of

mixed sulphide assemblages, galvanic interactions occur when the minerals are (or were) in contact, and these reactions continue if a suitable (e.g., low pH, high conductivity) medium is available to maintain the passage of electrons (Fig. 2.12.c, Fig. 2.13.c,d).

Table 2.6: Ages and estimated ages of seafloor massive sulphide samples.

Sample ID	Distance to Central Reference Line (m)	E/W of Center	Location Type	Age <sup>1</sup> (years)	Distance change (m/ year)	Estimated Age (Avg Dx * x)
<b>R1938-Rck-16</b>	170	E	Extinct within Active Vent Field	<b>629 ±45</b>	0.27	
R1938-Rck-20	345	E	Extinct within Active Vent Field			101
R1938-Rck-21	345	E	Extinct within Active Vent Field			101
R1938-Rck-22	420	E	Extinct within Active Vent Field			122
<b>R1939-Rck-13</b>	630	E	Eastern Half Graben	<b>5749 ±140</b>	0.11	
R1939-Rck-14	650	E	Eastern Half Graben			189
<b>R1940-Rck-1</b>	150	W	Active Zero Age	<b>0</b>		
R1940-Rck-2	190	W	Axial Valley Floor			55
R1940-Rck-3	250	W	Axial Valley Floor			73
R1940-Rck-4	250	W	Axial Valley Floor			73
<b>R1940-Rck-5</b>	310	W	Axial Valley Floor	<b>2382 ±50</b>	0.13	
R1940-Rck-6	390	W	Axial Valley Floor			114
R1940-Rck-7	405	W	Axial Valley Floor			118
R1940-Rck-8	505	W	Axial Valley Floor			147
R1940-Rck-9	600	W	Outside Axial Valley			175
R1941-Rck-12	245	W	Extinct within Active Vent Field			71
R1941-Rck-13	140	W	Extinct within Active Vent Field			41

<sup>1</sup>Bolded sample numbers and values represent radiometrically determined ages. Estimated sample ages are based on relationship between age of hydrothermal activity and distance from average ridge (average Dx = 0.29 m/year) (Jamieson et al., 2013).

For samples for which it was not possible to determine absolute ages (due to lack of sufficient barite), ages were estimated based on position within the axial valley relative to sites that were radioisotopically dated, and the interpreted spatial-temporal relationship between hydrothermal venting and faulting from Jamieson et al. (2013) (Table 2.6). A

comparison of absolute and estimated ages for vents and petrographic evidence for galvanic-mediated oxidation of sulfide minerals suggests that galvanic dissolution is a relatively rapid process, causing significant dissolution of sulfide metals over timescales of hundreds of years.

Galvanic interactions within natural mixed metal sulphide deposits, which can be compositionally highly variable, and texturally complex, will likely behave differently from experimental results, due to the dependency of galvanic cells on the size, shape and arrangement of the different mineral phases within the samples (e.g., intergrown minerals in Fig. 2.13.a versus secondary phases sharing a single grain boundary in Fig. 2.13.b). In one example, fine-grained sphalerite blebs in pyrite (Fig. 2.4.a) likely oxidized at a rate higher than would be predicted from laboratory-based sphalerite-pyrite galvanic experiments.

Petrographic observations indicate that, with increasing age, sulphide minerals are less likely to be in direct contact with each other, due to the galvanic dissolution of the anodic mineral phase breaking the necessary conductivity circuit required for electron flow (Fig. 2.12.b,c; Fig. 2.13.b,c,d). In contrast, young or inferred young (<400m from the inferred ridge axis) polymetallic massive sulphide samples typically have cathodic and anodic minerals that are still in direct contact with each other (Fig. 2.13.a).

Overall, older sulphide samples appear to progressively transition to a mineral assemblage dominated by high rest potential metal sulphide minerals, such as pyrite or marcasite, iron-oxyhydr(oxides), and reprecipitated secondary copper sulphide minerals (Table 2.5; Fig. 2.13.d). These mineral assemblage transitions are taking place over timescales of 100s to 1000s of years.

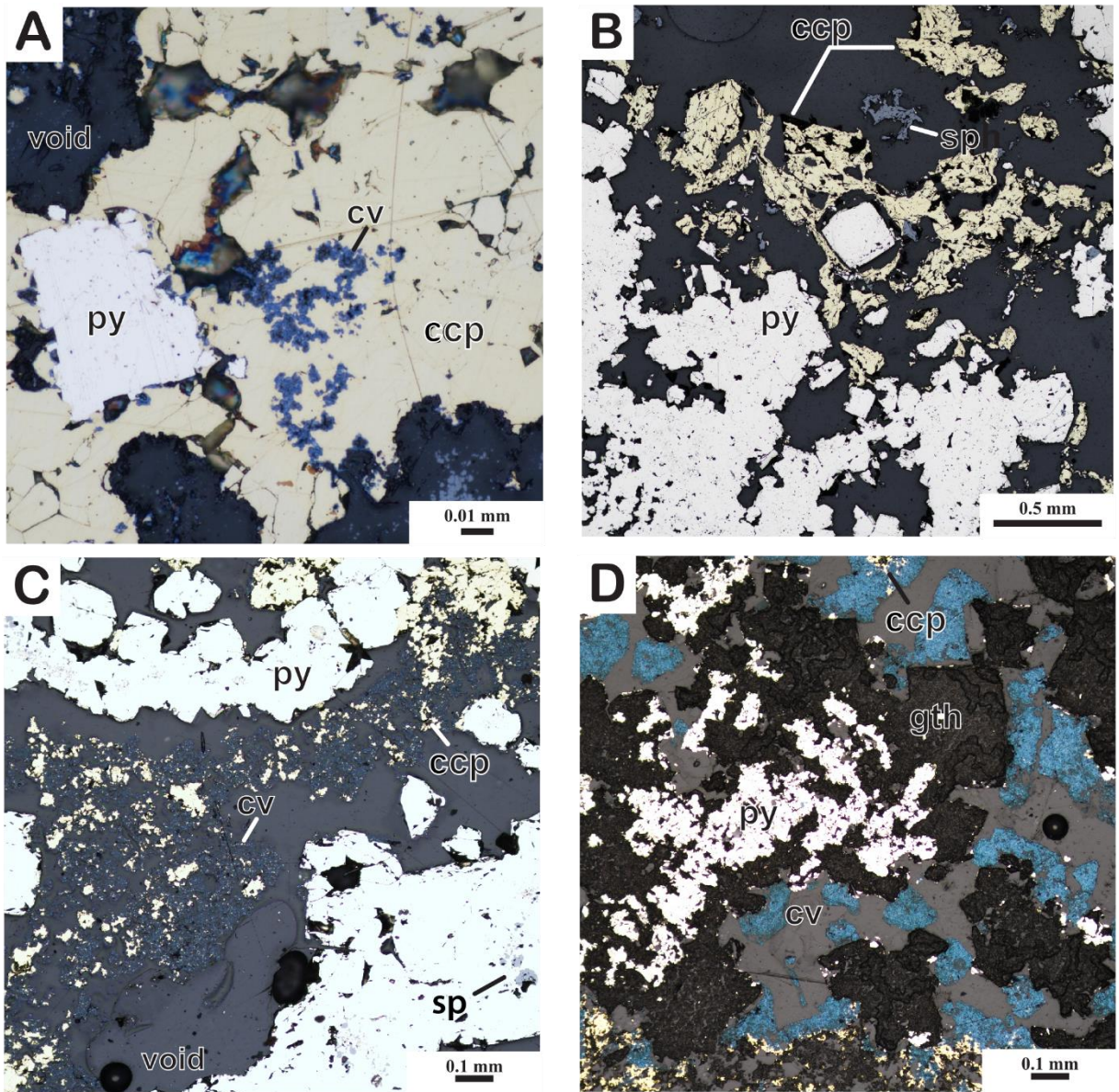


Figure 2.12: Plain polarized reflected light photomicrograph of the progressive galvanic interactions between polymetallic sulphide minerals. A) Cathodically protected euhedral cubic pyrite (py) galvanically reacting with intergrown subhedral chalcopyrite (ccp) forming secondary covellite (cv) along crystal fractures, and boundaries, B) progressed galvanic interaction of cathodically protected cubic euhedral pyrite and anodic preferentially oxidized subhedral chalcopyrite, and anhedral sphalerite (sp). C) Extensive preferential oxidative dissolution of chalcopyrite releasing copper ions into seawater precipitating covellite from pyrite with sphalerite blebs. D) Nearly complete oxidative dissolution and replacement of chalcopyrite into covellite no longer cathodically protecting pyrite and forming cubic remnant cubic goethite (gth) pseudomorphs.

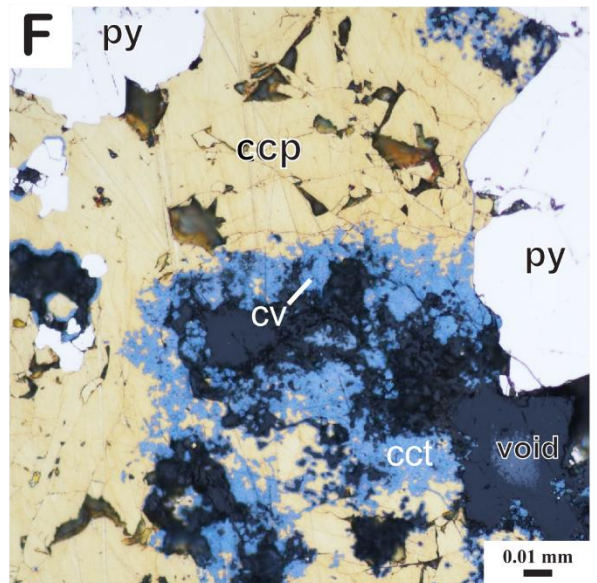
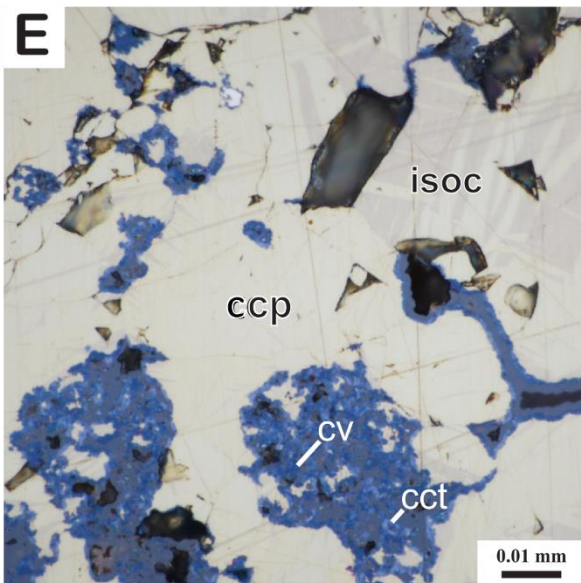
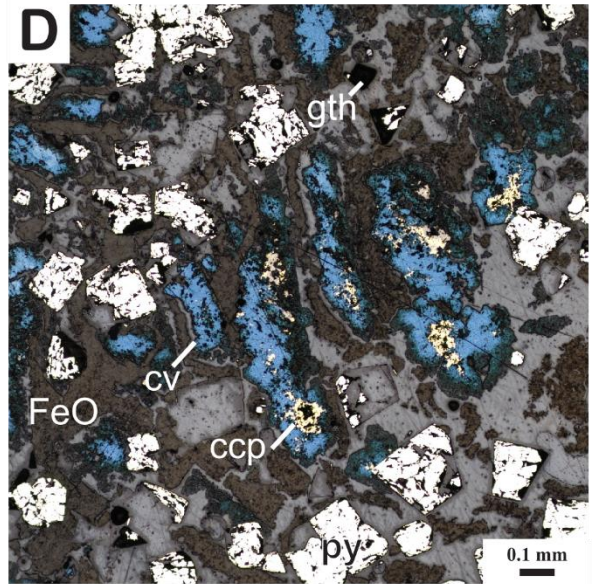
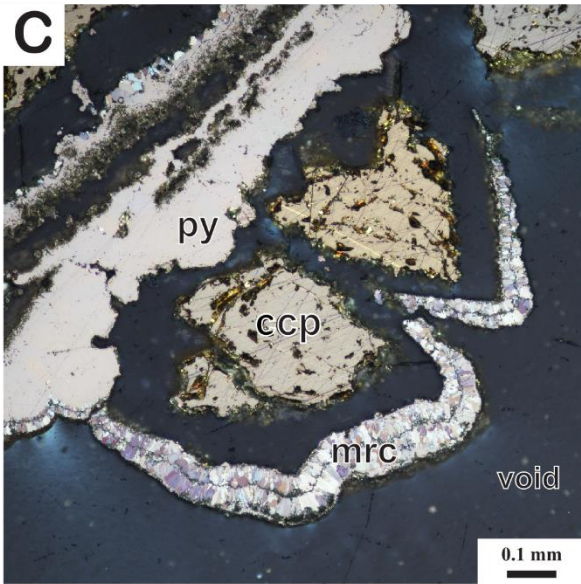
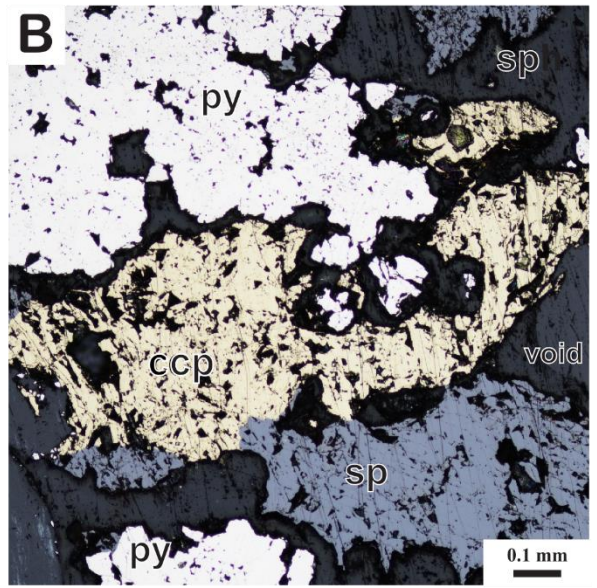
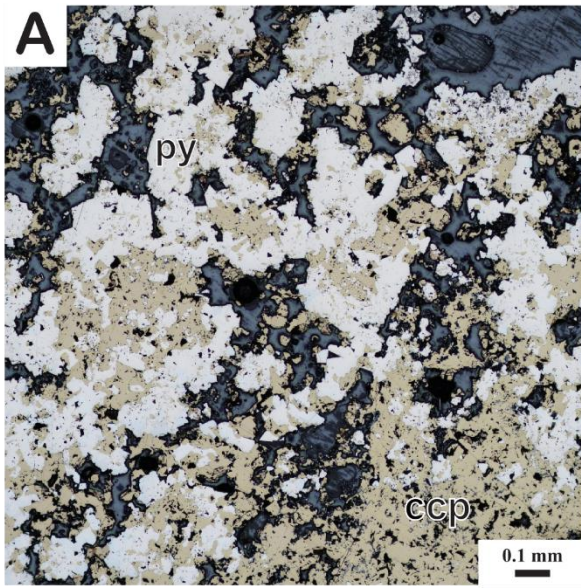


Figure 2.13: Galvanic interaction variation photomicrographs under reflected light. A. Intermingling euhedral massive pyrite (py) with chalcopyrite (cpy), B. Euhedral pyrite crystal aggregate in proximity but not in contact with subhedral chalcopyrite-sphalerite (sph), C. Anhedral chalcopyrite rimmed by banded marcasite (mrc) and massive subhedral pyrite, D. Late stage oxidation of chalcopyrite resulting in the release of copper ions into solution allowing for the secondary precipitation of covellite (cv) and the iron released into solution is oxidized to form Fe-oxhydr(oxide) precipitate. Pyrite replacement by goethite (gth) as it is not galvanically protected by another metal sulphide, E. massive chalcopyrite, isocubanite (isoc) solid solution with oxidation along chalcopyrite grain boundaries forming covellite and chalcocite (cc). No visible galvanic interactions are occurring between isocubanite and chalcopyrite, F. euhedral pyrite interacting with intermixed chalcopyrite forming secondary covellite and chalcocite.

### 2.6.1.3 Bacterially mediated Oxidation

In addition to precipitation driven by chemical gradients, Fe-oxyhydr(oxide) can also form from Fe-oxidizing bacteria that inhabit vents or parts of chimneys with low-temperature (<100°C) fluid venting (Juniper et al., 1988; L veill  & Juniper, 2002; Fortin & Langley, 2005). Here, the bacteria can rapidly convert aqueous Fe<sup>2+</sup> into Fe<sup>3+</sup>, resulting in the microbially-mediated precipitation of primary Fe-oxyhydr(oxides) that form distinct structures including filaments (Fig. 2.6.b), rods (Fig. 2.6.c, d), and spheroidal concretions (Fig. 2.6.e; Herzig et al., 1991). These structures have been documented to be able to grow over a 2-month period and are hypothesized to inhibit circumneutral abiotic Fe(II) oxidation and create an improved micro-environment for biotic oxidation (Toner et al., 2009). Bacterial generated oxidation products can also be distinguished by their trace element content. For example, silica is enriched in bacterially generated Fe-oxyhydr(oxides) (Fig. 2.9, Table 2.3) due to the large surface area of these precipitates (Jambor & Dutrizac, 2003). The occurrence of abiotic Fe-oxyhydr(oxide) precipitation on the surfaces of bacterial Fe-oxyhydroxide precipitates also suggests that the large surface area of the bacteria-mediated Fe-oxyhydr(oxides) enhances the ability for abiotic Fe-oxyhydr(oxide) precipitation in circumneutral seawater conditions (Fig. 2.6.d) (Kennedy et al., 2003). Overall, the enhanced nucleation potential of Fe-oxyhydr(oxides) can result in increased scavenging of metal ions (i.e. Fe<sup>3+</sup>, Fe<sup>2+</sup>, Cu, Zn) released into solution by sulphide oxidation (Kennedy et al., 2003).

The samples that contain significant bacterially derived Fe-oxyhydr(oxides) are generally highly oxidized in terms of their sulphide mineralogy. Bacteria can generate acidic pore waters, enhancing oxidation rates in circumneutral conditions by up to four times, and in acidic conditions by up to six times, relative to experimental abiotic rates (Kennedy et al., 2003; Penn et al., 2017). Thus, sulphide oxidation may be especially enhanced during the low-temperature, waning stages of venting, when conditions are suitable for microbial growth.

Once hydrothermal activity ceases, these low-temperature bacteria are replaced by other types of bacteria that thrive off of inactive, oxidizing chimneys (Sylvan et al., 2012; Meier et al., 2018). The presence of bacteria persisting in periods of hydrothermal inactivity indicates that, at both low temperatures and inactive hydrothermal vent sites, metal sulphide mineral assemblages may be subject to the influence of iron-oxidizing bacteria. These bacteria enable and accelerate oxidizing conditions by as much as an order of magnitude using the oxidation of Fe(II) from sulphide minerals (Jannasch, 1995; Edwards et al., 2003; Percak-Dennett et al., 2017).

Experimental work has shown that, in addition to affecting the immediate oxidation reactions occurring in neutral and acidic pH conditions, vent bacteria can directly impact the reactivity of galvanic cells and the rates of preferential dissolution in polymetallic sulphide deposits. This phenomenon is attributed to bacteria converting elemental sulphur into  $H_2SO_4$ , catalyzing galvanic interactions between  $CuFeS_2$  and  $FeS_2$  particles (Mehta & Murr, 1983). More recently, filamentous bacteria have been hypothesized to be ‘cable bacteria,’ transporting electrons between electron donors and acceptors over centimetre distances using electrical currents (Meysman, 2018). The increased ability of electron transport could imply an extension in the range of electrochemical redox reactions occurring within a polymetallic mineral assemblage. Within the Endeavour samples, this extended range of electron transportation occurs where bacterially related oxidation textures bridge gaps and pore spaces between sulphide minerals. The increased range in oxidation reactivity may explain why little to no

chalcopyrite occurs near bacteria-related textural features (Fig. 2.6, Fig. 2.8) despite being one of the slowest oxidizing minerals in monometallic reactions (Bilenker et al., 2016).

## **2.6.2 Seafloor Massive Sulphide Site Characteristics use as a Vector for Time**

### **2.6.2.1 Inactive seafloor massive sulphide morphology**

Visual characteristics of inactive hydrothermal chimneys, including the degree of sediment cover, morphology, oxidation, degree of Fe-Mn oxide coating, physical weathering, and colonization by sessile fauna not associated with active venting may provide insights into the estimated age of the structures (Jannasch, 1995; Koschinsky & Halbach, 1995; Tivey et al., 1999b; Hrischeva & Scott, 2007). Inactive chimney structures at Endeavour are either reddish-orange to reddish-brown or have black surface exteriors from precipitation of Mn-oxide (Fig. 2.3). Eight of the inactive chimneys sampled for this study host sessile corals and sea-sponges.

The transect up the western axial valley wall north of the Main Endeavour field was done to identify any patterns and trends related to the ageing of inactive chimneys. Results from ROV observations show that chimney morphology transitions as a function of age from more commonly tall (~15–20m), narrow, spire-like structures, to moderate (10–12m) sized structures that appear more bulbous, and finally to smaller (~5– 8 m) structures away from the axial valley floor. Sedimentation on the chimneys is only present at four chimney sites of varied ages and morphologies. Significant sedimentation is only likely to occur on inactive vents because thermal upwelling above active vents prevents significant sediment deposition. The prevention of sedimentation during active hydrothermal activity suggests that sedimented vents are indicative of extended periods of hydrothermal inactivity and increased age (Fig. 2.3.b, c, e). However, sedimentation rates within the axial valley are likely affected by local currents, and influence of hydrothermal plume fall-out. Thus, although sedimentation can provide an indication of vent inactivity, it is likely not a reliable tool to determine the age of inactivity. Coral and sponge colonization are present on chimneys from both the central axial valley and the upper valley rim, suggesting that colonization also does not provide information regarding

relative age of the chimneys, despite being an indicator of inactivity. Therefore, observations from this transect suggest that, as chimneys age, they decrease in size height, their morphological features become more subdued. Degree of sedimentation and presence, abundance and diversity of sessile animals do not correlate with age of inactive chimneys.

#### **2.6.2.2 Ferromanganese oxide precipitates**

The accumulation of ferromanganese crusts on inactive hydrothermal vents was investigated as an indicator of age of inactivity and for the potential to decrease sulphide oxidation within the vents. Five chimneys featured significant ferromanganese oxides precipitates on their surface. These crustal features were relatively uniform in their thickness (~1 mm) despite existing on both younger and older hydrothermal vent sites (Fig. 2.3.a, f). Three samples contained multiple ferromanganese precipitate bands intermixed within Fe-oxyhydr(oxides) (Fig. 2.5.e, f; Fig. 2.14). These intergrowing bands of ferromanganese precipitates and Fe-oxyhydr(oxide) suggest that there were multiple episodes of ferromanganese oxide precipitation in a relatively short period (<~5700 years). Based on the young ages of the collected sulphide samples, and the multiple precipitation bands visible in thin section, the observed ferromanganese oxide precipitates are likely due to nearby hydrothermal activity, as opposed to constant background hydrogenetic Mn precipitation more commonly associated with nodules and seamounts (Hein et al., 1997). Hydrothermal precipitation rates are incredibly rapid relative to hydrogenetic manganese precipitation, which slowly develop from the trace amounts of Mn in seawater (1 – 10 mm/Ma; Lusty et al., 2018). No meaningful correlations between age and crust thickness variations are apparent. However, degree of ferromanganese oxide coverage of inactive vents correlates with proximity to active venting. Therefore, Mn-oxide coatings cannot be used as an indicator of the age of a vent structure since proximity to active venting is the controlling factor on the thickness and growth rate of the coatings. Finally, thin section observations of Fe-Mn precipitates and crusts section

(Fig. 2.5.e, f) did not demonstrate any preservation potential as oxidative reactions appear to have progressed regardless of a crust being formed on a sample's exterior.

### **2.6.3 Implications of New $^{226}\text{Ra}/\text{Ba}$ Age Data for the Endeavour Segment**

This study adds three new dates to the inventory of ages of hydrothermal vents originally published by Jamieson et al. (2013). This study also provided a new datapoint for the “zero age”  $^{226}\text{Ra}/\text{Ba}$  calibration curve for the Endeavour Segment. The new zero age calibration point is especially significant because the active chimney from which the sample was collected contains significantly more Ba than previously analyzed zero age samples from the Endeavour vent fields (Fig. 2.11), thereby expanding the range of calibration and reducing the uncertainty associated with the extrapolation of the calibration curve. With the addition of the data point collected from this study, the  $^{226}\text{Ra}/\text{Ba}$  relationship was determined to remain statistically significant ( $r^2 = 0.997$ ) and significantly increases the confidence of the zero-age  $^{226}\text{Ra}/\text{Ba}$  value, which is used to determine the ages of samples from Endeavour with a wide range of barite content (Fig. 2.11).

For the three new dated samples, the sample collected from slightly north of MEF (R1940-Rck-5;  $2,382 \pm 50$  years) has an age that is consistent with the known age of venting at MEF (Fig. 2.10). This sample was collected from a faulted bench on the west valley wall, and the age of the sample is also consistent with ages from other samples on the faulted valley wall half-grabens (Fig. 2.15; Fig. 2.16). Sample R1938-R-16, collected from an inactive structure within the active Sasquatch field has an  $^{226}\text{Ra}/\text{Ba}$  age of  $629 \pm 45$  years. This age is younger than the two other known ages of venting at Sasquatch (Fig. 2.10) and provides further evidence that Sasquatch has been continuously active for at least 1,500 years. Sample R1939-R-13, collected from the eastern half-graben, provides the most surprising deposition age from this study. At  $5,749 \pm 140$  years, this sample provides, the oldest known record of hydrothermal venting within the axial valley (Fig. 2.10). Prior to this study, the oldest age within the axial valley was only  $\sim 3,200$  years, from a sample also collected from the eastern half-graben. The oldest age of hydrothermal venting at

Endeavour remains ~6,100 years, from a sample collected from outside the axial valley (Fig. 2.10; Jamieson et al., 2013).

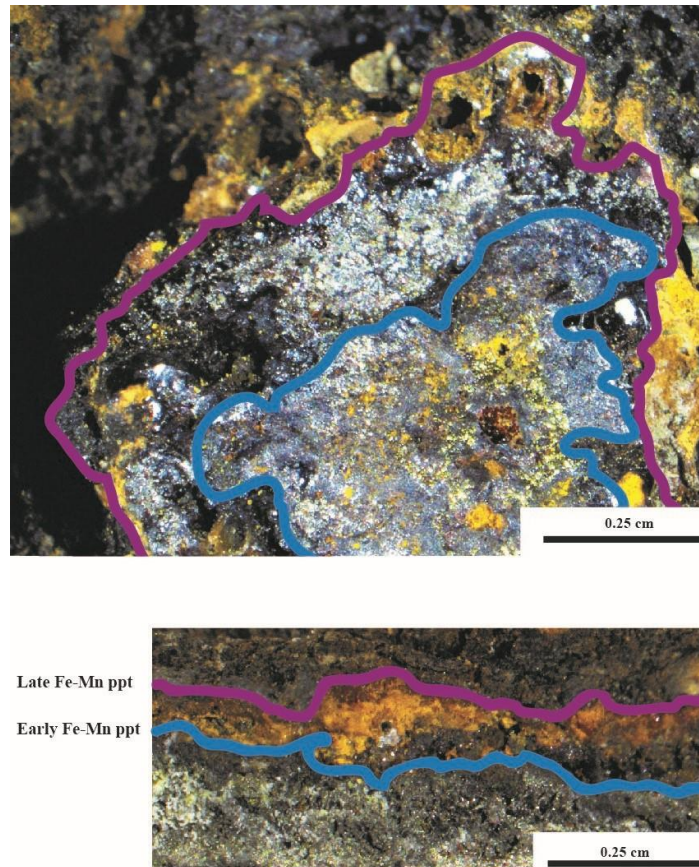


Figure 2.14: Orifice and massive sulphide wall perspectives of surface manganese precipitation, sulphide oxidation, and the original massive sulphide. Colour coordinated polylines indicate respective boundaries.

Overall, there is a general relationship between increasing age and decreasing mineralogical diversity with increasing distance from the ridge axis (Fig. 2.15; Fig. 2.16). The age versus distance trend (Fig. 2.16) indicates a coarse relationship of 6 years per meter distance from the estimated locus of the ridge axis. Because the location of hydrothermal

venting is intimately tied to fault-controlled subsurface permeability, this age/distance relationship is likely a result of the evolution of rift faulting within the axial valley, and not the spreading rate of the ridge itself. The spacing of the normal faults is neither regular, nor symmetrical across the valley. Therefore, caution must be applied when using the age/distance relationship to predict the ages of vents based primarily on distance from the axis (Table 2.6).

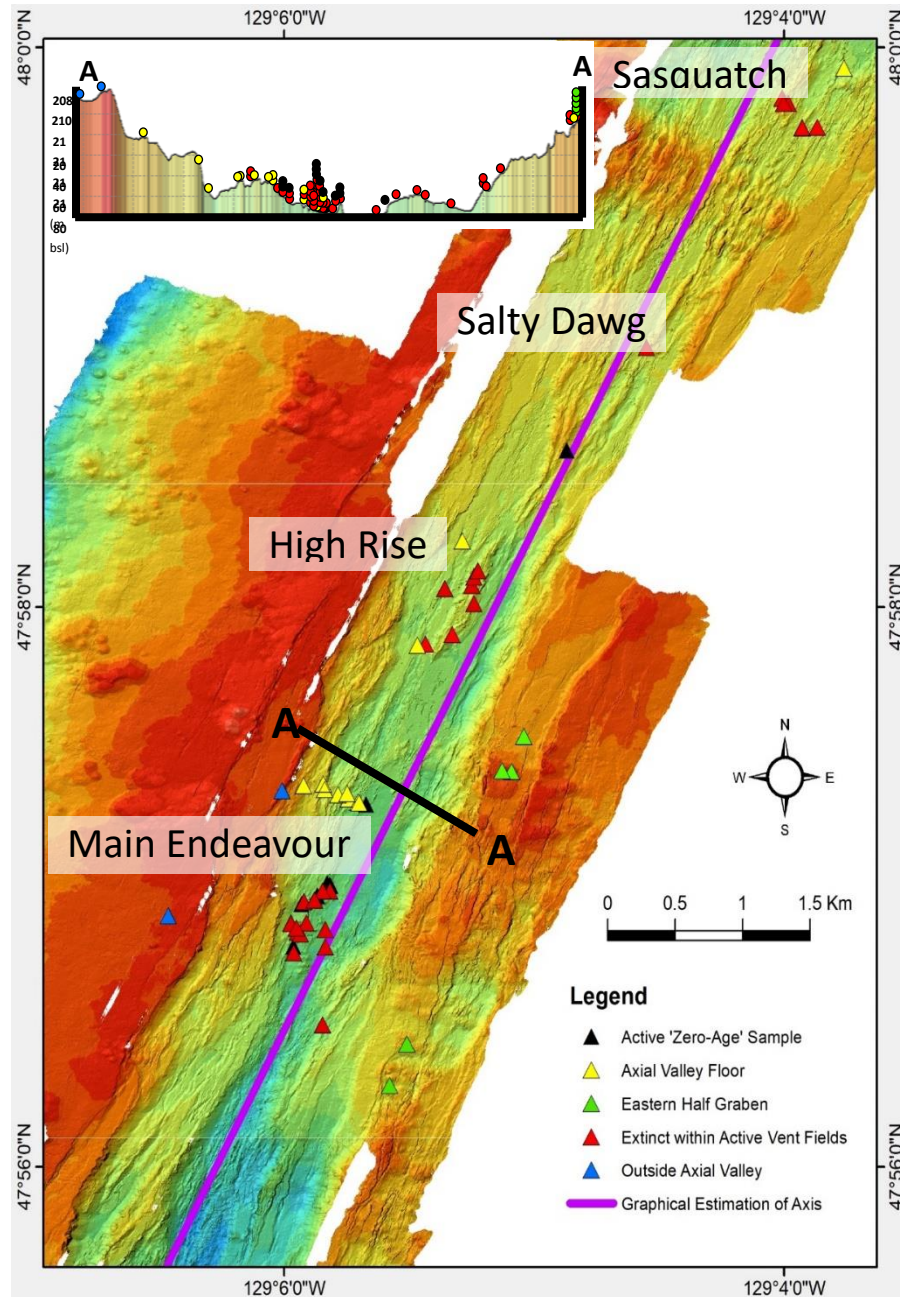


Figure 2.15: Map of samples from this and other studies with associated  $^{226}\text{Ra}/\text{Ba}$  age data (Jamieson et al., 2013). This figure shows the relative distances of the collected samples from a graphical estimate of the location of the spreading axis. Figure inset is defined by the cross-section A to A' providing depth of sample collection in meters below sea level (mbsl). All sample points follow the same colour trend defined in the legend.

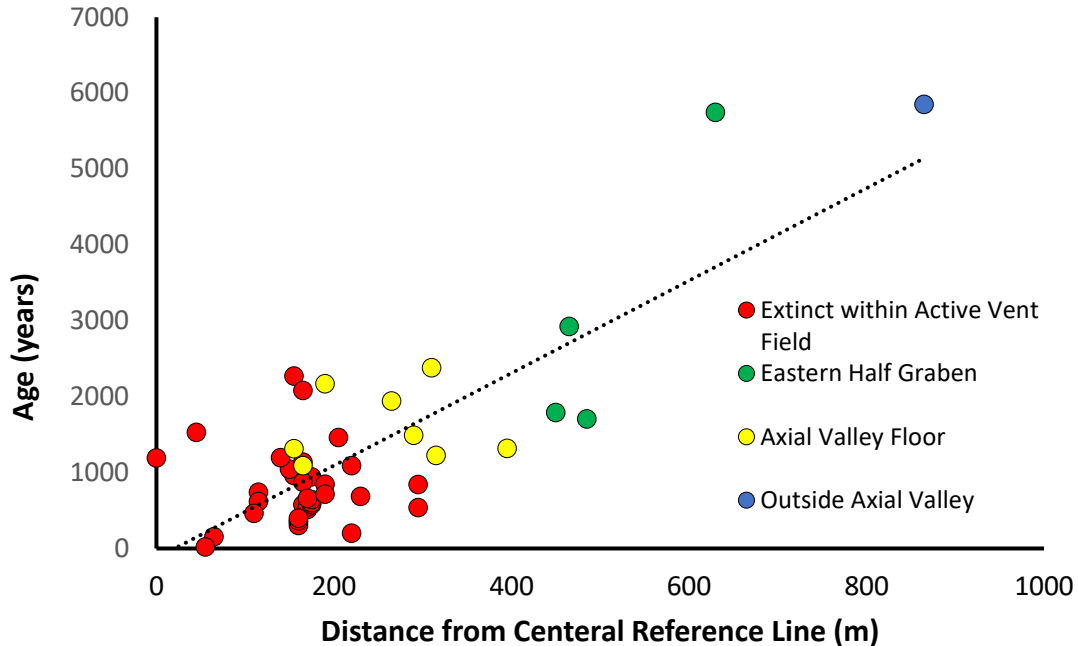


Figure 2.16: Biplot of age versus distance from the graphical estimation of the spreading center axis for all collected seafloor massive sulphide deposit samples with associated  $^{226}\text{Ra}/\text{Ba}$  barite dates. The linear regression line defined for the data series has a positive trend with a slope of  $\sim 6$  years/m ( $r^2 = 0.63$ ).

## 2.7 Conclusions

Inactive seafloor hydrothermal vents from the Endeavour Segment of the Juan de Fuca Ridge show evidence of mineralogical changes over time. The polymetallic composition of recently active hydrothermal deposits has textures that indicate the formation of galvanic cells that result in the preferential dissolution of low rest potential minerals such as chalcopyrite, sphalerite, covellite, and chalcocite. These electrochemical reactions, in turn, preserves higher rest potential mineralogy such as pyrite or marcasite

from oxidation. Based on  $^{226}\text{Ra}/\text{Ba}$  dating of four seafloor sulphide samples, the preferential dissolution of polymetallic sulphide deposits occurs relatively rapidly, with significant changes evident in samples that are less than ~5,700 years old. These observations point to the importance of galvanic interactions in that; (1) preferential oxidation of metal sulphide minerals likely results in greater abundances of high rest potential minerals on the seafloor (i.e. pyrite, marcasite); (2) galvanic cells proceed at a rapid rate in the timeframe of typical geologic processes that are hypothesized to be critical to deposit preservation, such as burial by sediments or lava flows; and (3) there is enhancement of galvanic cell effectiveness by bacterial influence. The potentially rapid oxidation processes which can occur implies a need for preservation within a relatively short period to maximize the economic potential of inactive polymetallic deposits on the seafloor.

Additionally, samples of a wide range of ages often host an abundance of Fe-oxyhydr(oxide) with textures associated with bacteria, such as sheaths, filaments, and concretions. The pervasive degree of oxidation makes identification of source material impossible, but the commonality of bacterial structures in association with a high degree of oxidation suggests the accelerating effect of bacteria on oxidation of seafloor sulphide deposits can take place within a relatively short (~5700 years) timespan.

## 2.8 References

- Acero, P., Cama, J., Ayora, C., & Asta, M. P. (2009). Chalcopyrite dissolution rate law from pH 1 to 3. *Geologica Acta*, 7(3), 389–397. <https://doi.org/10.1344/105.000001444>
- Acero, Patricia, Cama, J., & Ayora, C. (2007). Sphalerite dissolution kinetics in acidic environment. *Applied Geochemistry*, 22(9), 1872–1883. <https://doi.org/10.1016/j.apgeochem.2007.03.051>
- Ahonen, L., & Tuovinen, O. H. (1994). Solid-phase alteration and iron transformation in column bioleaching of a complex sulfide ore. In C. N. Alpers & D. W. Blowes (Eds.), *Environmental Geochemistry of Sulfide Oxidation ACS Symposium Series 550* (pp. 79–89). Washington, DC: American Chemical Society.
- Alt, J. C. (1995). Subseafloor processes in Mid-Ocean ridge hydrothermal systems. *Geophysical Monograph*, 91, 85–114. <https://doi.org/10.1017/CBO9781107415324.004>
- Anderson, G. L., Gates, M. P., & Nold, R. C. (1989). Mechanism of atmospheric oxidation of sulfur dioxide by hydroxyl radicals. In Biogenic Sulfur in the Environment. In E. S. Saltzman & W. J. Cooper (Eds.), *Biogenic Sulfur in the Environment* (pp. 437–449). Washington, DC.: American Chemical Society.
- Van Ark, E. M., Detrick, R. S., Canales, J. P., Carbotte, S. M., Harding, A. J., Kent, G. M., et al. (2007). Seismic structure of the endeavour segment, Juan de Fuca Ridge: Correlations with seismicity and hydrothermal activity. *Journal of Geophysical Research: Solid Earth*, 112(2), 1–22. <https://doi.org/10.1029/2005JB004210>
- Baker, E. T., & German, C. R. (2004). On the global distribution of hydrothermal vent fields . in Mid-Ocean Ridges: Hydrothermal Interactions Between the Lithosphere and Oceans. *Geophysical Monograph Series*, 148, 245–266. Retrieved from <http://www.pmel.noaa.gov/pubs/outstand/bake2544/bake2544.shtml>
- Baker, E. T., & Massoth, G. J. (1987). Characteristics of hydrothermal plumes from two vent fields on the Juan de Fuca Ridge, northeast Pacific Ocean. *Earth and Planetary Science Letters*, 85(1–3), 59–73. [https://doi.org/10.1016/0012-821X\(87\)90021-5](https://doi.org/10.1016/0012-821X(87)90021-5)
- Barker, W. W., Welch, S. A., Chu, S., & Banfield, J. F. (1998). Experimental observations of the effects of bacteria on aluminosilicate weathering. *American Mineralogist*, 83(11-12 PART 2), 1551–1563. <https://doi.org/10.2138/am-1998-11-1243>
- Beaulieu, S. E. (2015). InterRidge Global Database of Active Submarine Hydrothermal Vent Fields: prepared for InterRidge. <Http://Www.Interridge.Org/Irvents>. Retrieved from <http://ci.nii.ac.jp/naid/10029967540/en/>
- Belzile, N., Chen, Y. W., Cai, M. F., & Li, Y. (2004). A review on pyrrhotite oxidation. *Journal of Geochemical Exploration*, 84(2), 65–76.

<https://doi.org/10.1016/j.gexplo.2004.03.003>

- Bemis, K., Lowell, R., & Farough, A. (2012). Diffuse Flow On and Around Hydrothermal Vents at Mid-Ocean Ridges. *Oceanography*, 25(1), 182–191. <https://doi.org/10.5670/oceanog.2012.16>
- Benjamin, M. M., & Leckie, J. O. (1981). Multiple-site adsorption of Cd, Cu, and Pb on amorphous iron oxyhydroxides. *Journal of Colloid and Interface Science*, 79(1), 209–221. [https://doi.org/10.1016/0021-9797\(81\)90063-1](https://doi.org/10.1016/0021-9797(81)90063-1)
- Bhatti, T. M., Bigham, J. M., Carlson, L., & Tuovinen, O. H. (1993). Mineral products of pyrrhotite oxidation by *Thiobacillus ferrooxidans*. *Applied and Environmental Microbiology*, 59(6), 1984–1990.
- Bierens de Haan, S. (1991). A review of the rate of pyrite oxidation in aqueous systems at low temperature. *Earth-Science Reviews*, 31(1), 1–10. [https://doi.org/10.1016/0012-8252\(91\)90039-I](https://doi.org/10.1016/0012-8252(91)90039-I)
- Bilenker, L. D., Romano, G. Y., & McKibben, M. A. (2016). Kinetics of sulfide mineral oxidation in seawater: Implications for acid generation during in situ mining of seafloor hydrothermal vent deposits. *Applied Geochemistry*, 75, 20–31. <https://doi.org/10.1016/j.apgeochem.2016.10.010>
- Blowes, D. W., Ptacek, C. J., Jambor, J. L., Weisener, C. G., Paktunc, D., Gould, W. D., & Johnson, D. B. (2003). The Geochemistry of Acid Mine Drainage. In *Treatise on Geochemistry: Second Edition* (Vol. 11, pp. 131–190). Pergamon. <https://doi.org/10.1016/B978-0-08-095975-7.00905-0>
- Bowers, T. S., Von Damm, K. L., & Edmond, J. M. (1985). Chemical evolution of mid-ocean ridge hot springs. *Geochimica et Cosmochimica Acta*, 49(11), 2239–2252. [https://doi.org/10.1016/0016-7037\(85\)90224-8](https://doi.org/10.1016/0016-7037(85)90224-8)
- Brierley, J. A. (1980). Facultative-Thermophilic *Thiobacillus*-Like Bacteria in Metal Leaching. In *Biogeochemistry of Ancient and Modern Environments* (pp. 445–450). Berlin, Heidelberg: Springer.
- Brown, A. D., & Jurinak, J. J. (1989). Mechanism of Pyrite Oxidation in Aqueous Mixtures. *Journal of Environment Quality*, 18(4), 545–550. <https://doi.org/10.2134/jeq1989.00472425001800040028x>
- Butterfield, D. A., McDuff, R. E., Mottl, M. J., Lilley, M. D., Lupton, J. E., & Massoth, G. J. (1994). Gradients in the Composition of Hydrothermal Fluids From the Endeavor Segment Vent Field - Phase-Separation and Brine Loss. *Journal of Geophysical Research-Solid Earth*, 99(B5), 9561–9583. <https://doi.org/10.1029/93jb03132>
- Carbotte, S. M., Detrick, R. S., Harding, A., Canales, J. P., Babcock, J., Kent, G., et al. (2006). Rift topography linked to magmatism at the intermediate spreading Juan de Fuca Ridge. *Geology*, 34(3), 209–212. <https://doi.org/10.1130/G21969.1>

- Chandra, A. P., & Gerson, A. R. (2010). The mechanisms of pyrite oxidation and leaching: A fundamental perspective. *Surface Science Reports*, 65(9), 293–315. <https://doi.org/10.1016/j.surfrep.2010.08.003>
- Clague, D. A., Dreyer, B. M., Paduan, J. B., Martin, J. F., Caress, D. W., Gill, J. B., et al. (2014). Eruptive and tectonic history of the Endeavour Segment, Juan de Fuca Ridge, based on AUV mapping data and lava flow ages. *Geochemistry, Geophysics, Geosystems*, 15(8), 3364–3391. <https://doi.org/10.1002/2014GC005415>
- Von Damm, K. L., Edmond, J. M., Grant, B., Measures, C. I., Walden, B., & Weiss, R. F. (1985). Chemistry of submarine hydrothermal solutions at 21 °N, East Pacific Rise. *Geochimica et Cosmochimica Acta*, 49(11), 2197–2220. [https://doi.org/10.1016/0016-7037\(85\)90222-4](https://doi.org/10.1016/0016-7037(85)90222-4)
- Delaney, J. R., Robigou, V., McDuff, R. E., & Tivey, M. K. (1992a). Geology of a vigorous hydrothermal system on the Endeavour Segment, Juan de Fuca Ridge. *Journal of Geophysical Research*, 97(B13), 19663–19682. <https://doi.org/10.1029/92jb00174>
- Delaney, J. R., Robigou, V., McDuff, R. E., & Tivey, M. K. (1992b). Geology of a vigorous hydrothermal system on the Endeavour Segment, Juan de Fuca Ridge. *Journal of Geophysical Research*, 97(B13), 19663. <https://doi.org/10.1029/92JB00174>
- Ditchburn, R., Barry, B. J., & de Ronde, C. E. J. (2005). Uranium series disequilibrium dating of volcanic massive sulphide deposits.pdf. *UMI: Marine Minerals: Crossroads of Science, Engineering, and the Environment*.
- Ditchburn, R. G., de Ronde, C. E. J., & Barry, B. J. (2007). Application of radiometric dating methods to modern seafloor volcanic massive sulphide deposits - insights into hydrothermal processes. *UMI: Marine Minerals of the Pacific: Science, Economics and the Environment*.
- Edwards, K. J., Rogers, D. R., Wirsén, C. O., & McCollom, T. M. (2003). Isolation and characterization of novel psychrophilic, neutrophilic, Fe-oxidizing, chemolithoautotrophic  $\alpha$ - and  $\gamma$ -Proteobacteria from the deep sea. *Applied and Environmental Microbiology*, 69(5), 2906–2913. <https://doi.org/10.1128/AEM.69.5.2906-2913.2003>
- Edwards, Katrina J., McCollom, T. M., Konishi, H., & Buseck, P. R. (2003). Seafloor bioalteration of sulfide minerals: Results from in situ incubation studies. *Geochimica et Cosmochimica Acta*, 67(15), 2843–2856. [https://doi.org/10.1016/S0016-7037\(00\)00089-9](https://doi.org/10.1016/S0016-7037(00)00089-9)
- Edwards, Katrina J. (2004). Formation and degradation of seafloor hydrothermal sulfide deposits, 83–96.
- Fallon, E. K., Petersen, S., Brooker, R. A., & Scott, T. B. (2017). Oxidative dissolution of hydrothermal mixed-sulphide ore: An assessment of current knowledge in relation to

- seafloor massive sulphide mining. *Ore Geology Reviews*, 86, 309–337.  
<https://doi.org/10.1016/j.oregeorev.2017.02.028>
- Feely, R. A., Geiselman, T. L., Baker, E. T., Massoth, G. J., & Hammond, S. R. (1990). Distribution and composition of hydrothermal plume particles from the ASHES Vent Field at Axial Volcano, Juan de Fuca Ridge. *Journal of Geophysical Research*, 95(B8), 12855. <https://doi.org/10.1029/JB095iB08p12855>
- Fortin, D., & Langley, S. (2005). Formation and occurrence of biogenic iron-rich minerals. *Earth-Science Reviews*, 72(1–2), 1–19.  
<https://doi.org/10.1016/j.earscirev.2005.03.002>
- Fouquet, Y., Wafik, A., Cambon, P., Mevel, C., Meyer, G., & Gente, P. (1993). Tectonic setting and mineralogical and geochemical zonation in the snake pit sulfide deposit (mid-Atlantic ridge at 23N). *Economic Geology*, 88(8), 2018–2036.  
<https://doi.org/10.2113/gsecongeo.88.8.2018>
- Frankel, G. S. (2016). Fundamentals of corrosion kinetics. In *Active Protective Coatings* (pp. 17–23). <https://doi.org/10.1007/978-94-017-7540-3>
- Fullston, D., Fornasiero, D., & Ralston, J. (1999). Zeta potential study of the oxidation of copper sulfide minerals. *Colloids and Surfaces A: Physicochemical and Engineering Aspects*, 146(1–3), 113–121. [https://doi.org/10.1016/S0927-7757\(98\)00725-0](https://doi.org/10.1016/S0927-7757(98)00725-0)
- Gartman, A., Yücel, M., & Luther III, G. W. (2014). An Introduction to the Major Chemical Components Released from Hydrothermal Vents. *Reference Module in Earth Systems and Environmental Sciences*, (Ii), 1–11. <https://doi.org/10.1016/B978-0-12-409548-9.09105-3>
- Gartman, Amy, & Luther, G. W. (2014). Oxidation of synthesized sub-micron pyrite (FeS<sub>2</sub>) in seawater. *Geochimica et Cosmochimica Acta*, 144, 96–108.  
<https://doi.org/10.1016/j.gca.2014.08.022>
- Gartman, Amy, Findlay, A. J., & Luther, G. W. (2014). Nanoparticulate pyrite and other nanoparticles are a widespread component of hydrothermal vent black smoker emissions. *Chemical Geology*, 366, 32–41.  
<https://doi.org/10.1016/j.chemgeo.2013.12.013>
- Glickson, D. A., Kelley, D. S., & Delaney, J. R. (2006). The Sasquatch hydrothermal field: Linkages between seismic activity, hydrothermal flow, and geology. In *AGU Fall Meeting Abstracts*.
- Goldstein, S. J., Murrell, M. T., Janecky, D. R., Delaney, J. R., & Clague, D. A. (1991, October 1). Geochronology and petrogenesis of MORB from the Juan de Fuca and Gorda ridges by <sup>238</sup>U/<sup>230</sup>Th disequilibrium. *Earth and Planetary Science Letters*. Elsevier. [https://doi.org/10.1016/0012-821X\(92\)90088-D](https://doi.org/10.1016/0012-821X(92)90088-D)
- Grundl, T., & Delwiche, J. (1993). Kinetics of ferric oxyhydroxide precipitation. *Journal of Contaminant Hydrology*, 14(1), 71–87. <https://doi.org/10.1016/0169->

7722(93)90042-Q

- Hannington, M. D. (1993). The formation of atacamite during weathering of sulfides on the modern seafloor. *Canadian Mineralogist*, 31(4), 945–956.
- Hannington, Mark D., Jonasson, I. R., & Petersen, S. (1995). Physical and Chemical Processes of Seafloor Mineralization at Mid-Ocean Ridges. In *Seafloor hydrothermal systems: physical, chemical, biological, and geological interactions; Geophysical monograph ; 91* (pp. 115–157).
- Hannington, Mark D., De Ronde, C. E. J., & Petersen, S. (2005). Sea-Floor Tectonics and Submarine Hydrothermal Systems. *Economic Geology*, 100th Anni, 111–141. Retrieved from <http://eprints.uni-kiel.de/6271/>
- Hannington, Mark D., Jamieson, J., Monecke, T., & Petersen, S. (2010). Modern Sea-Floor Massive Sulfides and Base Metal Resources: Toward an Estimate of Global Sea-Floor Massive Sulfide Potential. *Society of Economic Geologists Special Publication 15*, 317–338. Retrieved from <file://localhost/Users/jescartin/WORK/Referencias/pdfs/Hannington2010.pdf>
- Hannington, Mark D., & Scott, S. D. (1988). Mineralogy and Geochemistry of a Hydrothermal Silica-Sulfide-Sulfate Spire in the Caldera of Axial Seamount, Juan de Fuca Ridge. *Canadian Mineralogist*, 26, 603–625.
- Haymon, R. M., & Kastner, M. (1981). Hot spring deposits on the East Pacific Rise at 21°N: preliminary description of mineralogy and genesis. *Earth and Planetary Science Letters*, 53(3), 363–381. [https://doi.org/10.1016/0012-821X\(81\)90041-8](https://doi.org/10.1016/0012-821X(81)90041-8)
- Heidel, C., Tichomirowa, M., & Junghans, M. (2013a). Oxygen and sulfur isotope investigations of the oxidation of sulfide mixtures containing pyrite, Galena, And sphalerite. *Chemical Geology*, 342, 29–43. <https://doi.org/10.1016/j.chemgeo.2013.01.016>
- Heidel, C., Tichomirowa, M., & Junghans, M. (2013b). Oxygen and sulfur isotope investigations of the oxidation of sulfide mixtures containing pyrite, Galena, And sphalerite. *Chemical Geology*, 342, 29–43. <https://doi.org/10.1016/j.chemgeo.2013.01.016>
- Hein, J. R., Koschinsky, A., Halbach, P., Manheim, F. T., Bau, M., Kang, J.-K., & Lubick, N. (1997). Iron and manganese oxide mineralization in the Pacific. *Geological Society, London, Special Publications*, 119(1), 123–138. <https://doi.org/10.1144/GSL.SP.1997.119.01.09>
- Herzig, P. M., Hannington, M. D., Scott, S. D., Maliotis, G., Rona, P. A., & Thompson, G. (1991). Gold-rich sea-floor gossans in the troodos ophiolite and on the mid-Atlantic ridge. *Economic Geology*, 86(8), 1747–1755. <https://doi.org/10.2113/gsecongeo.86.8.1747>
- Hrischeva, E., & Scott, S. D. (2007). Geochemistry and morphology of metalliferous

- sediments and oxyhydroxides from the Endeavour segment, Juan de Fuca Ridge. *Geochimica et Cosmochimica Acta*, 71(14), 3476–3497.  
<https://doi.org/10.1016/j.gca.2007.03.024>
- Hutchins, S. R., Davidson, M. S., Brierley, J. A., & Brierley, C. L. (1986). Microorganisms in Reclamation of Metals. *Annual Review of Microbiology*, 40, 311–336.
- Jambor, J.L. (1986). *Detailed mineralogical examination of alteration products in core WA-20 from Waite Amulet tailings.*
- Jambor, John L., & Dutrizac, J. E. (2003). Occurrence and Constitution of Natural and Synthetic Ferrihydrite, a Widespread Iron Oxyhydroxide. *Chemical Reviews*, 98(7), 2549–2586. <https://doi.org/10.1021/cr970105t>
- Jamieson, J., & Petersen, S. (2015). Hydrothermalism, 1–19.
- Jamieson, J. W., Clague, D. A., & Hannington, M. D. (2014). Hydrothermal sulfide accumulation along the Endeavour Segment, Juan de Fuca Ridge. *Earth and Planetary Science Letters*, 395, 136–148. <https://doi.org/10.1016/j.epsl.2014.03.035>
- Jamieson, John W., Hannington, M. D., Clague, D. A., Kelley, D. S., Delaney, J. R., Holden, J. F., et al. (2013). Sulfide geochronology along the Endeavour Segment of the Juan de Fuca Ridge. *Geochemistry, Geophysics, Geosystems*, 14(7), 2084–2099. <https://doi.org/10.1002/ggge.20133>
- Jamieson, John William, Hannington, M. D., Tivey, M. K., Hansteen, T., Williamson, N. M. B. B., Stewart, M., et al. (2016). Precipitation and growth of barite within hydrothermal vent deposits from the Endeavour Segment, Juan de Fuca Ridge. *Geochimica et Cosmochimica Acta*, 173, 64–85.  
<https://doi.org/10.1016/j.gca.2015.10.021>
- Janecky, D. R., & Seyfried, W. E. (1984). Formation of massive sulfide deposits on oceanic ridge crests: Incremental reaction models for mixing between hydrothermal solutions and seawater. *Geochimica et Cosmochimica Acta*, 48(12), 2723–2738.  
[https://doi.org/10.1016/0016-7037\(84\)90319-3](https://doi.org/10.1016/0016-7037(84)90319-3)
- Jannasch, H. W. (1995). Microbial interactions with hydrothermal fluids. Seafloor Hydrothermal Systems: Physical, chemical, biological, and geological interactions. In *Geophysical Monograph Series* (Vol. 91, pp. 273–296).
- Janzen, M. P., Nicholson, R. V., & Scharer, J. M. (2000). Pyrrhotite reaction kinetics: Reaction rates for oxidation by oxygen, ferric iron, and for nonoxidative dissolution. *Geochimica et Cosmochimica Acta*, 64(9), 1511–1522.  
[https://doi.org/10.1016/S0016-7037\(99\)00421-4](https://doi.org/10.1016/S0016-7037(99)00421-4)
- Juniper, S. K. I. M., Fouquet, Y., Brest, C. De, & Cedex, B. (1988). Filamentous iron-silica deposits from modern and ancient hydrothermal sites. *Canadian Mineralogist*, 26, 859–869.

- Kappel, E. S., & Ryan, W. B. F. (1986). Volcanic episodicity and a non-steady-state rift valley along northeast Pacific spreading centers: Evidence from SeaMARC I. *Journal of Geophysical Research*, *91*(3), 13925–13940.
- Karsten, J. L., Hammond, S. R., Davis, E. E., & Currie, R. G. (1986). Detailed geomorphology and neotectonics of the Endeavour Segment, Juan de Fuca Ridge: New results from Seabeam swath mapping. *Geological Society of America Bulletin*, *97*(2), 213–221.
- Kelley, D. S., Delaney, J. R., & Yoerger, D. A. (2001). Geology and venting characteristics of the Mothra Hydrothermal Field, Endeavour Segment, Juan de Fuca Ridge. *Geology*, *29*, 959–962.
- Kelley, D. S., Delaney, J. R., Lilley, M., & Butterfield, D. A. (2001). Vent field distribution and evolution along the Endeavour Segment, Juan de Fuca Ridge. In *Eos, Transactions, American Geophysical Union* (p. (82)47).
- Kelley, D. S. D., Carbotte, S. M., Caress, D. W., Clague, D. A., Delaney, J. R., Gill, J. B., et al. (2012). Endeavour Segment of the Juan de Fuca Ridge: one of the most remarkable places on Earth. *Oceanography*, *25*(1), 44–61. <https://doi.org/10.5670/oceanog.2012.03>
- Kelley, Deborah S., Delaney, J. R., & Juniper, S. K. (2014). Establishing a new era of submarine volcanic observatories: Cabling Axial Seamount and the Endeavour Segment of the Juan de Fuca Ridge. *Marine Geology*, *352*, 426–450. <https://doi.org/10.1016/j.margeo.2014.03.010>
- Kellogg, J. P., & McDuff, R. E. (2010). A hydrographic transient above the Salty Dawg hydrothermal field, Endeavour segment, Juan de Fuca Ridge. *Geochemistry, Geophysics, Geosystems*, *11*(12). <https://doi.org/10.1029/2010GC003299>
- Kennedy, C. B., Scott, S. D., & Ferris, F. G. (2003). Characterization of bacteriogenic iron oxide deposits from Axial Volcano, Juan de Fuca Ridge, northeast Pacific ocean. *Geomicrobiology Journal*, *20*(3), 199–214. <https://doi.org/10.1080/01490450303873>
- Kimball, B. E., Rimstidt, J. D., & Brantley, S. L. (2010). Chalcopyrite dissolution rate laws. *Applied Geochemistry*, *25*(7), 972–983. <https://doi.org/10.1016/j.apgeochem.2010.03.010>
- Knight, R. D., Roberts, S., & Cooper, M. J. (2017). Investigating monomineralic and polymineralic reactions during the oxidation of sulphide minerals in seawater: Implications for mining seafloor massive sulphide deposits. *Applied Geochemistry*, *90*(August 2017), 63–74. <https://doi.org/10.1016/j.apgeochem.2017.12.027>
- Konhauser, K. O., Amskold, L., Lalonde, S. V., Posth, N. R., Kappler, A., & Anbar, A. (2007). Decoupling photochemical Fe(II) oxidation from shallow-water BIF deposition. *Earth and Planetary Science Letters*, *258*(1–2), 87–100. <https://doi.org/10.1016/j.epsl.2007.03.026>

- Koschinsky, A., & Halbach, P. (1995). Sequential leaching of marine ferromanganese precipitates: Genetic implications. *Geochimica et Cosmochimica Acta*, 59(24), 5113–5132. [https://doi.org/10.1016/0016-7037\(95\)00358-4](https://doi.org/10.1016/0016-7037(95)00358-4)
- Koski, R. A., Clague, D. A., & Oudin, E. (1984). Mineralogy and chemistry of massive sulfide deposits from the Juan de Fuca Ridge. *Geological Society of America Bulletin*, 95(8), 930–945. [https://doi.org/10.1130/0016-7606\(1984\)95<930:MACOMS>2.0.CO;2](https://doi.org/10.1130/0016-7606(1984)95<930:MACOMS>2.0.CO;2)
- Koski, R. A., Benninger, L. M., Zierenberg, R. A., & Jonasson, I. R. (1994). Composition and growth history of hydrothermal deposits in Escanaba Trough, southern Gorda Ridge. *US Geological Survey Bulletin*, 2022, 293–324.
- Kwong, Y. T. J., Swerhone, G. W., & Lawrence, J. R. (2005). Galvanic sulphide oxidation as a metal-leaching mechanism and its environmental implications. *Geochemistry: Exploration, Environment, Analysis*, 3(4), 337–343. <https://doi.org/10.1144/1467-7873/03/013>
- Lehrmann, B., Stobbs, I. J., Lusty, P. A. J., & Murton, B. J. (2018). minerals Insights into Extinct Seafloor Massive Sulfide Mounds at the TAG, Mid-Atlantic Ridge, 1–17. <https://doi.org/10.3390/min8070302>
- Léveillé, R. J., & Juniper, S. K. (2002). Microbial colonization and weathering of sulphide minerals at deep-sea hydrothermal vents: In situ exposure experiments. *Cahiers de Biologie Marine*, 43(3–4), 285–288.
- Li, L., Polanco, C., & Ghahreman, A. (2016). Fe(III)/Fe(II) reduction-oxidation mechanism and kinetics studies on pyrite surfaces. *Journal of Electroanalytical Chemistry*, 774, 66–75. <https://doi.org/10.1016/j.jelechem.2016.04.035>
- Lloyd, R. M. (1967). Oxygen-18 Composition of Oceanic Sulfate. *Science*, 156(3779), 1228–1231. <https://doi.org/10.1126/science.156.3779.1228>
- Lowson, R. T. (1982). Aqueous oxidation of pyrite by molecular oxygen. *Chemical Reviews*, 82(5), 461–497. <https://doi.org/10.1021/cr00051a001>
- Lundgren, D. G., & Silver, M. (1980). Ore Leaching by Bacteria. *Annual Review of Microbiology*, 34(1), 263–283. <https://doi.org/10.1146/annurev.mi.34.100180.001403>
- Lusty, P. A. J., Hein, J. R., & Josso, P. (2018). Formation and Occurrence of Ferromanganese Crusts: Earth's Storehouse for Critical Metals. *Elements*, 14(5), 313–318. <https://doi.org/10.2138/gselements.14.5.313>
- Lydon, J. W., Goodfellow, W. D., & Jonasson, I. R. (1985). A general genetic model for stratiform baritic deposits of the Selwyn Basin, Yukon Territory and district of Mackenzie. *Paper, Geological Survey of Canada*, 85–1 A(January), 651–660.
- Mehta, A. P., & Murr, L. E. (1983). Fundamental studies of the contribution of galvanic interaction to acid-bacterial leaching of mixed metal sulfides. *Hydrometallurgy*, 9(3),

235–256. [https://doi.org/10.1016/0304-386X\(83\)90025-7](https://doi.org/10.1016/0304-386X(83)90025-7)

- Meier, D. V., Pjevac, P., Bach, W., Markert, S., Schweder, T., Jamieson, J., et al. (2018). Microbial metal-sulfide oxidation in inactive hydrothermal vent chimneys suggested by metagenomic and metaproteomic analyses. *Environmental Microbiology*. <https://doi.org/10.1111/1462-2920.14514>
- Meysman, F. J. R. (2018). Cable Bacteria Take a New Breath Using Long-Distance Electricity. *Trends in Microbiology*, 26(5), 411–422. <https://doi.org/10.1016/j.tim.2017.10.011>
- Miki, H., & Nicol, M. J. (n.d.). The kinetics of the copper-catalysed oxidation of iron (II) in chloride solutions. In Young, C., C. Anderson, P. Taylor, & Y. Choi (Eds.), *Hydrometallurgy* (pp. 971–979). Warrendale, PA, USA: The Minerals, Metals and Materials Society.
- Moses, C. O., & Herman, J. S. (1991). Pyrite oxidation at circumneutral pH. *Geochimica et Cosmochimica Acta*, 55(2), 471–482. [https://doi.org/10.1016/0016-7037\(91\)90005-P](https://doi.org/10.1016/0016-7037(91)90005-P)
- Moses, C. O., Kirk Nordstrom, D., Herman, J. S., & Mills, A. L. (1987). Aqueous pyrite oxidation by dissolved oxygen and by ferric iron. *Geochimica et Cosmochimica Acta*, 51(6), 1561–1571. [https://doi.org/10.1016/0016-7037\(87\)90337-1](https://doi.org/10.1016/0016-7037(87)90337-1)
- Mozgova, N. N., Borodaev, Y. S., Gablina, I. F., Cherkashev, G. A., & Stepanova, T. V. (2005). Mineral assemblages as indicators of the maturity of oceanic hydrothermal sulfide mounds. *Lithology and Mineral Resources*, 40(4), 293–319. <https://doi.org/10.1007/s10987-005-0030-z>
- Murowchick, J. B., & Barnes, H. L. (1986). Marcasite precipitation from hydrothermal solutions. *Geochimica et Cosmochimica Acta*, 50(12), 2615–2629. [https://doi.org/10.1016/0016-7037\(86\)90214-0](https://doi.org/10.1016/0016-7037(86)90214-0)
- Nicholson, R. V., & Sharer, J. M. (1994). Laboratory studies of pyrrhotite oxidation kinetics. In C. N. Alpers & D. W. Blowes (Eds.), *Environmental Geochemistry of Sulfide Oxidation ACS Symposium Series, vol. 550* (pp. 1077–1085). Washington, DC.
- Nicol, M., Miki, H., & Zhang, S. (2017). The anodic behaviour of covalite in chloride solutions: Voltammetry. *Hydrometallurgy*, 171(June), 198–205. <https://doi.org/10.1016/j.hydromet.2017.05.016>
- Nordstrom, D. K., & Southam, G. (1997). Geomicrobiology of sulfide mineral reduction. *Reviews in Mineralogy*, 35(June), 361–390.
- Ohmoto, H. (1996). Formation of volcanogenic massive sulfide deposits: The Kuroko perspective. *Ore Geology Reviews*, 10, 135–177. [https://doi.org/10.1016/0169-1368\(95\)00021-6](https://doi.org/10.1016/0169-1368(95)00021-6)
- Olsen, L. (2016). *Weathering of Deep-Sea Hydrothermal Sulfide Deposits*. University of

Bergen, Norway.

- Opdyke, M. D., & Channell, J. E. T. (1996). *Magnetic stratigraphy* (64th ed.). Academic Press.
- Paradis, S., Jonasson, I. R., Le Cheminant, G. M., & Watkinson, D. H. (1988). Two zinc-rich chimneys from the Plume Site, Southern Juan de Fuca Ridge. *Canadian Mineralogist*, 26 pt 3, 637–654.
- Penn, R. L., Li, D., & Soltis, J. A. (2017). New Perspectives on Mineral Nucleation and Growth, 257–273. <https://doi.org/10.1007/978-3-319-45669-0>
- Percak-Dennett, E., He, S., Converse, B., Konishi, H., Xu, H., Corcoran, A., et al. (2017). Microbial acceleration of aerobic pyrite oxidation at circumneutral pH. *Geobiology*, 15(5), 690–703. <https://doi.org/10.1111/gbi.12241>
- Petersen, S., Krättschell, A., Augustin, N., Jamieson, J., Hein, J. R., & Hannington, M. D. (2016). News from the seabed – Geological characteristics and resource potential of deep-sea mineral resources. *Marine Policy*, 70, 175–187. <https://doi.org/10.1016/j.marpol.2016.03.012>
- Reed, M. H., & Palandri, J. (2006). Sulfide Mineral Precipitation from Hydrothermal Fluids. *Reviews in Mineralogy and Geochemistry*, 61(1), 609–631. <https://doi.org/10.2138/rmg.2006.61.11>
- Riddihough, R. (1984). Recent Movements of the Juan De Fuca Plate System. *Journal of Geophysical Research*, 89(B8), 6980–6994. <https://doi.org/10.1029/JB089iB08p06980>
- Ridley, B. W. I., & Survey, U. S. G. (2010). Volcanogenic Massive Sulfide Occurrence Model.
- Rimstidt, D. D., & Vaughan, D. J. (2003). Pyrite oxidation: A state-of-the-art assessment of the reaction mechanism. *Geochimica et Cosmochimica Acta*, 67(5), 873–880. [https://doi.org/10.1016/S0016-7037\(02\)01165-1](https://doi.org/10.1016/S0016-7037(02)01165-1)
- Rimstidt J. Donald, Chermak John A., & Gagen Patrick M. (1993). Rates of Reaction of Galena, Sphalerite, Chalcopyrite, and Arsenopyrite with Fe(III) in Acidic Solutions. *Environmental Geochemistry of Sulfide Oxidation*, 550(Iii), 2–13. <https://doi.org/10.1021/bk-1994-0550>
- Robigou, V., Delaney, J. R., & Stakes, D. S. (1993). LARGE MASSIVE SULFIDE DEPOSITS IN A NEWLY DISCOVERED ACTIVE HYDROTHERMAL SYSTEM, THE HIGH-RISE FIELD, ENDEAVOUR SEGMENT, JUAN DE FUCA RIDGE. *Geophysical Research Letters*, 20(17), 1887–1890.
- Ryan, W. B. F., Carbotte, S. M., Coplan, J. O., O’Hara, S., Melkonian, A., Arko, R., et al. (2009). Global multi-resolution topography synthesis. *Geochemistry, Geophysics, Geosystems*, 10(3). <https://doi.org/10.1029/2008GC002332>

- Dos Santos, E. C., de Mendonça Silva, J. C., & Duarte, H. A. (2016). Pyrite Oxidation Mechanism by Oxygen in Aqueous Medium. *The Journal of Physical Chemistry C*, 120(5), 2760–2768. <https://doi.org/10.1021/acs.jpcc.5b10949>
- Sato, M. (1960). Oxidation of sulfide ore bodies, II. Oxidation mechanisms of sulfide minerals at 25° C. *Economic Geology*, 55(6), 1202–1231. <https://doi.org/10.2113/gsecongeo.55.6.1202>
- Sato, M. (1992). Persistency-field Eh-pH diagrams for sulfides and their application to supergene oxidation and enrichment of sulfide ore bodies. *Geochimica et Cosmochimica Acta*, 56(8), 3133–3156. [https://doi.org/10.1016/0016-7037\(92\)90294-S](https://doi.org/10.1016/0016-7037(92)90294-S)
- Schwertmann, U. (1983). Effect of pH on the Formation of Goethite and Hematite from Ferrihydrite. *Clays and Clay Minerals*, 31(4), 277–284. <https://doi.org/10.1346/CCMN.1983.0310405>
- Scott, S. D., & Barnes, H. L. (1972). Sphalerite-wurtzite equilibria and stoichiometry. *Geochimica et Cosmochimica Acta*, 36(11), 1275–1295. [https://doi.org/10.1016/0016-7037\(72\)90049-X](https://doi.org/10.1016/0016-7037(72)90049-X)
- Seyfried, W. E., & Janecky, D. R. (1985). Heavy metal and sulfur transport during subcritical and supercritical hydrothermal alteration of basalt : Influence of fluid pressure and basalt composition and crystallinity. *Geochimica et Cosmochimica Acta*, 49, 2545–2560.
- Singer, P. C., & Stumm, W. (1970). Acidic Mine Drainage: The Rate-Determining Step. *Science*, 167(3921), 1121–1123. <https://doi.org/10.1126/science.167.3921.1121>
- Skirrow, R., & Coleman, M. L. (1982). Origin of sulphur and geothermometry of hydrothermal sulphides from the Galapagos Rift , 86 ° W. *Nature*, 299(September), 142–144.
- Spieß, F. N., Macdonald, K. C., Atwater, T., Ballard, R., Carranza, A., Cordoba, D., et al. (1980). East Pacific Rise: Hot Springs and Geophysical Experiment. *Geological Survey*, 207(4438), 1421–1433. Retrieved from <http://science.sciencemag.org/>
- Stakes, D., & Moore, W. S. (1991). Evolution of Hydrothermal Activity on the Juan de Fuca Ridge- Observations, Mineral Ages, and Ra Isotope Ratios. *Journal of Geophysical Research*, 96(91), 21, 739–721, 752.
- Steger, H. F. (1982). Oxidation of sulfide minerals. VII. Effect of temperature and relative humidity on the oxidation of pyrrhotite. *Chemical Geology*, 35(3–4), 281–295. [https://doi.org/10.1016/0009-2541\(82\)90006-7](https://doi.org/10.1016/0009-2541(82)90006-7)
- Steger, H. F., & Desjardins, L. E. (1978). Oxidation of sulfide minerals, 4. Pyrite, chalcopyrite and pyrrhotite. *Chemical Geology*, 23(1–4), 225–237. [https://doi.org/10.1016/0009-2541\(78\)90079-7](https://doi.org/10.1016/0009-2541(78)90079-7)
- Sullivan, E. A., Zajic, J. E., & Jack, T. R. (1980). The effect of chemical and biological

- redox reactions on the growth of *Thiobacillus thiooxidans*. In *Biochemistry of ancient and modern environments. Proc. 4th Int. Syrup. Environmental Biogeochem. (ISEB), Leaching Conf.*
- Suzuki, I. (1974). Mechanisms of Inorganic Oxidation and Energy Coupling. *Annual Review of Microbiology*, 28(1), 85–102.  
<https://doi.org/10.1146/annurev.mi.28.100174.000505>
- Suzuki, I., Chan, C. W., & Takeuchi, T. L. (1994). Oxidation of inorganic sulfur compounds by Thiobacilli. In *Alpers, C.N., Blowes, D.W. (Eds.), Environmental Geochemistry of Sulfide Oxidation ACS Symposium Series, vol. 550* (pp. 60–67). Washington, D.C.
- Sylvan, J. B., Toner, B. M., Edwards, K. J., Sylvan, J. B., Toner, B. M., & Edwards, K. J. (2012). Life and Death of Deep-Sea Vents: Bacterial Diversity and Ecosystem Succession on Inactive Hydrothermal Sulfides. *MBio*, 3(1), 1–10.  
<https://doi.org/10.1128/mBio.00279-11.Editor>
- Tivey, M. (2007). Generation of Seafloor Hydrothermal Vent Fluids and Associated Mineral Deposits. *Oceanography*, 20(1), 50–65.  
<https://doi.org/10.5670/oceanog.2007.80>
- Tivey, M K. (1995). Modeling Chimney Growth and Associated Fluid Flow at Seafloor Hydrothermal Vent Sites. *Geophysical Monograph Series*, 91, 158–177.
- Tivey, Margaret K., & Delaney, J. R. (1986). Growth of large sulfide structures on the endeavour segment of the Juan de Fuca ridge. *Earth and Planetary Science Letters*, 77(3–4), 303–317. [https://doi.org/10.1016/0012-821X\(86\)90142-1](https://doi.org/10.1016/0012-821X(86)90142-1)
- Tivey, Margaret K, & McDuff, R. E. (1990). Mineral Precipitation in the Walls of Black Smoker Chimneys: A Quantitative Model of Transport and Chemical Reaction. *J. Geophys. Res.*, 95(B8), 12617–12637. <https://doi.org/10.1029/JB095iB08p12617>
- Tivey, Margaret Kingston, Stakes, D. S., Cook, T. L., Hannington, M. D., & Petersen, S. (1999a). A model for growth of steep-sided vent structures on the Endeavour Segment of the Juan de Fuca Ridge: Results of a petrologic and geochemical study. *Journal of Geophysical Research: Solid Earth*, 104(B10), 22859–22883.  
<https://doi.org/10.1029/1999JB900107>
- Tivey, Margaret Kingston, Stakes, D. S., Cook, T. L., Hannington, M. D., & Petersen, S. (1999b). A model for growth of steep-sided vent structures on the Endeavour Segment of the Juan de Fuca Ridge: Results of a petrologic and geochemical study. *Journal of Geophysical Research*, 104(B10), 22859.  
<https://doi.org/10.1029/1999JB900107>
- Toner, B.M., Santelli, C.M., Marcus, M.A., Wirth, R., Chan, C.S., McCollom, T.M., Bach, W. and Edwards, K.J. (2009) Biogenic iron oxyhydroxide formation at Mid-Ocean Ridge hydrothermal vents: Juan de Fuca Ridge. *Geochim. Cosmochim. Acta* 73, 388-403.

Viravamurthy, M. A., & Zhou, W. (1995). Characterization of a Transient +2 Sulfur Oxidation State Intermediate from the Oxidation of Aqueous Sulfide. *ACS Symposium Series, Geochemica*(April).

Zierenberg, R. a., Shanks, W. C., & Bischoff, J. L. (1984). Massive sulfide deposits at 21°N, East Pacific Rise: Chemical composition, stable isotopes, and phase equilibria. *Geological Society of America Bulletin*, 95(8), 922.  
[https://doi.org/10.1130/0016-7606\(1984\)95<922:MSDANE>2.0.CO;2](https://doi.org/10.1130/0016-7606(1984)95<922:MSDANE>2.0.CO;2)

## **Chapter 3 Summary**

This study of mineralogical changes associated with oxidation of sulfide minerals within inactive hydrothermal vents from the Endeavour Segment of the Juan de Fuca Ridge has resulted in an increased understanding in the role of biotic and abiotic oxidation, and the importance of galvanic interactions. In the context of previous studies that have focused experimental results, this study highlights the disparity in available data regarding the in-situ geologic weathering and oxidation processes occurring on the seafloor (Bilenker et al., 2016; Fallon et al., 2017; Knight et al., 2017; Léveillé & Juniper, 2002; Olsen, 2016; Rimstidt & Vaughan, 2003). This project provides evidence that indicates that inactive seafloor massive sulphide deposits are subject to the constant effects of biologic, geochemical, mineralogic, and surrounding seawater factors, each of which impacts sulphide mineral assemblages at different rates.

### **3.1 Findings**

Results presented in chapter two demonstrate that there are chemical, biological, and geological factors with complex intermixed relationships that ultimately have observable effects on extinct seafloor massive sulphide deposits. Scanning electron microscopy provided evidence for secondary precipitation of Cu-sulphide minerals as previously shown in experiments, and also aided in identifying multiple Fe-oxyhydr(oxide) phases present within the exterior oxidized precipitates forming on massive sulphide samples, and provided Fe/Mn geochemical data confirming the hydrothermal origin of ferromanganese oxides within the sample suites. Radiometric

$^{226}\text{Ra}/\text{Ba}$  geochronological data were collected from a subset of four samples which increase in age moving away from the spreading center of the Juan de Fuca ridge, providing more supportive data to the relationship between distance from the spreading center and increasing age of seafloor massive sulphide deposits (Jamieson et al., 2013).

### **3.2 Recommendations**

There are several avenues of continued research to pursue based on these findings. Primarily, additional samples should be collected from other hydrothermal vent locations on the seafloor for a greater range of sample comparisons. This comparison would include incorporating samples collected from older venting fields such as on the Mid-Atlantic Ridge, which could provide greater insight into the long-term effects of ambient seafloor oxidation processes that were shown in this study to occur in relatively rapid rates. Furthermore, samples should be collected from hydrothermal vent fields located at greater depths to observe what impacts changes in the amount of dissolved oxygen may have on seafloor massive sulphide oxidation processes. A more detailed investigation using higher precision analytical techniques such as the scanning electron microscope – mineral liberation analysis (SEM-MLA) would be beneficial for determining the composition of the Fe-oxyhydr(oxides) with greater precision, leading to an improved understanding of the oxidation reactions occurring in ambient seawater conditions. Additionally, further study should be pursued in the determining the timing of SMS deposit oxidation reaction rates.

### **3.3 Future work**

Future work at the Endeavour Segment should support the current finding by conducting further sampling to solidify the observed features of this study. Also, it would be beneficial to collect multiple samples from individual venting sites to investigate how significant the heterogeneity of each vent site when studying SMS deposit mineralogy.

Active seafloor hydrothermal venting sites having been definitively documented as concentrated points of life on the seafloor (Juniper et al., 1988; Léveillé & Juniper, 2002). As technology has better allowed for the location and study of inactive seafloor hydrothermal vent sites, we believe that further investigation into the colonization of these inactive hydrothermal venting sites may provide some additional unknown information regarding seafloor processes associated with the evolution of inactive vent sites.

Isotopic studies of oxidation reaction are believed to be important indicators of source components. Sulphur isotopes can be used to determine if sulphur is dominantly derived from sulphides or sulphates, and oxygen isotopes can be used to establish if oxygen is obtained from molecular oxygen or water/sulphate sources (Heidel et al., 2013a; Lloyd, 1967).

### **3.4 Conclusions**

This study was done to assess the petrographic and lithochemical variations, which may occur at an inactive hydrothermal vents over time. We documented these changes based on sixteen seafloor samples, fourteen of which were determined to be massive sulphide samples, one a seafloor basalt, and one a seafloor sulphate sample. During our assessment, we observed that:

- Galvanic cells naturally generated within polymetallic massive sulphide deposits appear to limit the long-term existence of lower rest potential metal sulphide minerals and, therefore, the possible mineral assemblage diversity under oxidizing conditions. The limitation on the long-term presence of some metal sulphide minerals could significantly impact the abundances of sphalerite and chalcopyrite, both major ore minerals. As a result, galvanic interactions may have a significant impact on any polymetallic SMS deposit's economic potential.
- Iron-oxyhydr(oxide) production occurs dually from abiotic and biotic oxidation of inactive and low-temperature SMS deposits. We observed that abiotic oxidation results in amorphous surface precipitates and replacement of primary sulphide

minerals, while bacterial oxidation generates texturally distinctive microstructures that act as scaffolding and further development of oxidation rinds at the surface of SMS deposits.

- Heavily oxidized seafloor samples are commonly composed of primarily Fe-oxyhydr(oxides) relating to hydrothermal vent bacteria, providing further support to bacteria being a significant enhancing agent of oxidation reactions on the seafloor. These Fe-oxyhydr(oxide)-dominated deposits appear to adsorb elements that are relatively abundant in seawater (U, V, Al, Sr). Adsorption of these elements progressively enriches Fe-oxyhydr(oxide) precipitates found at older vent deposits.
- Ferromanganese coatings commonly associated with hydrogenetically formed manganese nodules on the seafloor can also be abundant on the surface of SMS deposit samples. They are not an indicator of deposit age; however, as ferromanganese crusts may be precipitated on sulphide and sulphate surfaces rapidly if near to active metal-rich hydrothermal venting.

### 3.5 References

- Heidel, C., Tichomirowa, M., & Junghans, M. (2013). Oxygen and sulfur isotope investigations of the oxidation of sulfide mixtures containing pyrite, Galena, And sphalerite. *Chemical Geology*, *342*, 29–43. <https://doi.org/10.1016/j.chemgeo.2013.01.016>
- Juniper, S. K., & Fouquet, Y. (1988). Filamentous Iron-Silica Deposits from Modern and Ancient Hydrothermal Sites. *Canadian Mineralogist*, *26*, 859–869.
- Léveillé, R. J., & Juniper, S. K. (2002). Microbial colonization and weathering of sulphide minerals at deep-sea hydrothermal vents: In situ exposure experiments. *Cahiers de Biologie Marine*, *43*(3–4), 285–288.
- Lloyd, R. M. (1967). Oxygen-18 Composition of Oceanic Sulfate. *Science*, *156*(3779), 1228–1231. <https://doi.org/10.1126/science.156.3779.122>

## Appendices

### Appendix 1 – Sample Site Coordinate List

Sample ID	Vent Field	Latitude	Longitude	Depth (mbsl)
R1938-Rck-16	Sasquatch	47.997005	-129.066782	2149
R1938-Rck-20	Sasquatch	47.995207	-129.065437	2154
R1938-Rck-21	Sasquatch	47.99523	-129.065452	2154
R1938-Rck-22	Sasquatch	47.995263	-129.064435	2151
R1939-Rck-13	Eastern Half Graben	47.940647	-129.091813	2130
R1939-Rck-14	Eastern Half Graben	47.938167	-129.092967	2145
R1940-Rck-1	Raven (N of MEF)	47.954902	-129.094518	2195
R1940-Rck-2	Raven (N of MEF)	47.955048	-129.09506	2184
R1940-Rck-3	Raven (N of MEF)	47.955237	-129.095697	2184
R1940-Rck-4	Raven (N of MEF)	47.955248	-129.095702	2184
R1940-Rck-5	Raven (N of MEF)	47.9555	-129.096393	2157
R1940-Rck-6	Raven (N of MEF)	47.955803	-129.097297	2137
R1940-Rck-7	Raven (N of MEF)	47.956117	-129.09739	2138
R1940-Rck-8	Raven (N of MEF)	47.956022	-129.098702	2125
R1940-Rck-9	Outside Axial Valley	47.955735	-129.100133	2074
R1941-Rck-12	High Rise	47.96446	-129.090573	2179
R1941-Rck-13	High Rise	47.96503	-129.088788	2156



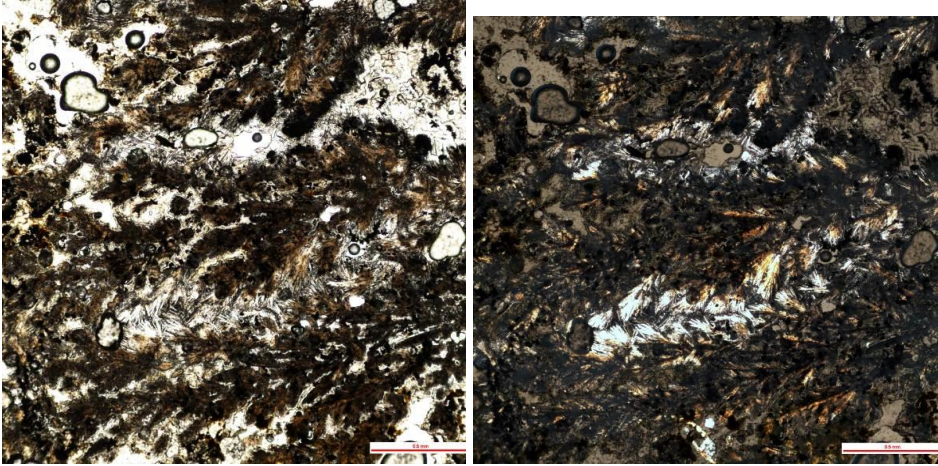
## Appendix 2 – Whole Rock Geochemical Results

Analyte Symbol	Au	Ag	As	Ba	Br	Co	Cr	Th	Zn	La	Ce	Nd	Sm	Yb	Lu	Fe	Na	Sb	Sc	Se
Unit Symbol	ppb	ppm	ppm	ppm	ppm	ppm	ppm	ppm	ppm	ppm	ppm	ppm	ppm	ppm	ppm	%	%	ppm	ppm	ppm
Detection Limit	2	2	1	20	0.5	0.1	0.5	0.1	10	0.05	1	1	0.01	0.05	0.01	0.01	0.001	0.1	0.01	0.5
Analysis Method	INAA	INAA	INAA	INAA	INAA	INAA	INAA	INAA	INAA	INAA	INAA	INAA	INAA	INAA	INAA	INAA	INAA	INAA	INAA	INAA
R1938-Rck-16	385	100	261	147000	12.8	30.8	< 0.5	< 0.1	16400	1.37	< 1	79	0.14	< 0.05	< 0.01	8.32	0.31	35.6	< 0.01	< 0.5
R1938-Rck-20	1230	108	200	1040	35.5	15.8	< 0.5	< 0.1	454000	< 0.05	< 1	< 1	0.16	< 0.05	< 0.01	6.25	0.55	73.1	< 0.01	< 0.5
R1938-Rck-21	240	38	201	3870	22.4	759	13.2	< 0.1	31600	1.18	< 1	< 1	0.23	< 0.05	< 0.01	37.2	0.18	12.5	< 0.01	163
R1938-Rck-22	127	< 2	373	270	51.9	726	13.4	< 0.1	2160	< 0.05	< 1	5	< 0.01	< 0.05	< 0.01	39.3	0.37	2.7	< 0.01	24.7
R1939-Rck-13	450	79	555	11700	27	199	17	< 0.1	36300	6.95	< 1	< 1	1.14	0.77	0.09	38.3	0.43	100	0.37	< 0.5
R1939-Rck-14	200	6	351	680	4.3	364	3.8	< 0.1	470	< 0.05	< 1	7	0.07	< 0.05	< 0.01	41.8	0.04	5.2	0.32	100
R1940-Rck-1	49	< 2	257	137000	57.4	18.5	56.3	0.1	1850	11.6	13	179	0.89	1.38	0.24	22.9	1.05	4	1.52	< 0.5
R1940-Rck-2	70	6	135	260	5.3	100	7.1	< 0.1	920	< 0.05	< 1	< 1	< 0.01	< 0.05	< 0.01	41.3	0.07	2.1	0.17	100
R1940-Rck-4	117	< 2	351	450	24	239	9.8	< 0.1	2290	< 0.05	< 1	< 1	< 0.01	< 0.05	< 0.01	43.5	0.17	3.5	0.16	185
R1940-Rck-5	111	< 2	291	94500	35.5	21.3	9.3	< 0.1	4740	7.27	5	150	0.48	0.7	0.1	29.4	0.8	13.6	0.63	< 0.5
R1940-Rck-6	63	< 2	150	190	14.9	39.7	9.3	< 0.1	2630	< 0.05	< 1	< 1	0.1	< 0.05	< 0.01	45.3	0.16	3.3	0.25	111
R1940-Rck-7	242	8	679	< 20	8.8	57.2	2.6	< 0.1	1890	< 0.05	< 1	< 1	< 0.01	< 0.05	< 0.01	53.3	0.13	8.6	0.28	65.4
R1940-Rck-8	65	7	110	< 20	5.9	43	11.8	0.4	3170	< 0.05	< 1	< 1	< 0.01	< 0.05	< 0.01	52.9	0.1	2	0.33	59.9
R1940-Rck-9	< 2	< 2	241	540	62	40.2	< 0.5	< 0.1	7940	3.2	< 1	< 1	0.38	0.67	0.07	26.6	2.53	13.1	0.66	< 0.5
R1941-Rck-12	38	13	46	< 20	7.2	51.4	< 0.5	< 0.1	3460	< 0.05	< 1	< 1	< 0.01	< 0.05	< 0.01	48.5	0.12	0.8	< 0.01	40.5
R1941-Rck-13	161	34	331	370	6.3	71.3	12.7	< 0.1	21900	< 0.05	< 1	< 1	< 0.01	< 0.05	< 0.01	50.9	0.08	10.3	< 0.01	66.6

Analyte Symbol	Sr	Ta	Al	B	Bi	Ca	Cd	Cs	Cu	Dy	Er	Eu	Ga	Gd	Ge	Ho	Hf
Unit Symbol	ppm	ppm	%	ppm	ppm	%	ppm										
Detection Limit	100	0.3	0.01	10	2	0.01	2	0.1	2	0.3	0.1	0.1	0.2	0.1	0.7	0.2	10
Analysis Method	INAA	INAA	FUS-MS-Na2O2														
R1938-Rck-16	8500	< 0.3	0.38	< 10	< 2	0.21	57	1	2480	< 0.3	< 0.1	< 0.1	18.2	0.2	6.7	< 0.2	< 10
R1938-Rck-20	< 100	< 0.3	0.29	< 10	< 2	0.06	1350	4.4	19700	< 0.3	< 0.1	< 0.1	131	< 0.1	57.3	< 0.2	20
R1938-Rck-21	< 100	< 0.3	0.03	20	3	0.07	95	1.1	105000	< 0.3	0.1	< 0.1	21.9	0.2	31.6	< 0.2	< 10
R1938-Rck-22	< 100	< 0.3	0.01	< 10	< 2	0.05	9	0.2	5420	< 0.3	< 0.1	< 0.1	1.1	< 0.1	6.4	< 0.2	< 10
R1939-Rck-13	< 100	< 0.3	0.21	50	< 2	0.2	194	2	13300	1.3	0.9	0.3	160	1.2	78.1	0.3	< 10
R1939-Rck-14	< 100	5.1	0.03	< 10	< 2	0.07	< 2	0.8	47800	< 0.3	< 0.1	< 0.1	1.9	< 0.1	6	< 0.2	< 10
R1940-Rck-1	18600	< 0.3	0.49	160	< 2	0.74	3	1.1	< 2	2	1.4	0.6	2.3	2.1	9.3	0.4	< 10
R1940-Rck-2	< 100	2.5	0.08	< 10	< 2	0.06	3	0.2	54900	< 0.3	< 0.1	< 0.1	0.9	< 0.1	6.2	< 0.2	< 10
R1940-Rck-4	< 100	2.8	0.05	< 10	< 2	0.08	7	0.4	30900	< 0.3	< 0.1	< 0.1	2	< 0.1	7.5	< 0.2	< 10
R1940-Rck-5	3700	< 0.3	0.33	150	< 2	0.36	3	0.7	2590	0.8	0.6	0.3	18.2	0.9	26.1	< 0.2	< 10
R1940-Rck-6	< 100	2.5	< 0.01	< 10	< 2	0.06	10	1	3160	< 0.3	< 0.1	< 0.1	7.5	< 0.1	6.6	< 0.2	< 10
R1940-Rck-7	< 100	2.8	0.07	< 10	3	0.09	7	0.8	664	< 0.3	< 0.1	< 0.1	2	< 0.1	5.9	< 0.2	< 10
R1940-Rck-8	< 100	1.9	0.03	< 10	< 2	0.08	8	0.9	10100	< 0.3	< 0.1	< 0.1	1.5	< 0.1	6.6	< 0.2	< 10
R1940-Rck-9	< 100	< 0.3	0.13	300	< 2	1.62	6	2.2	1480	0.8	0.6	0.1	5.1	0.6	7.1	< 0.2	10
R1941-Rck-12	< 100	2	0.07	< 10	< 2	0.08	10	1.3	69900	< 0.3	< 0.1	< 0.1	1.8	< 0.1	5.6	< 0.2	< 10
R1941-Rck-13	< 100	2	0.01	< 10	< 2	0.09	81	0.3	10400	< 0.3	< 0.1	< 0.1	6.1	< 0.1	5.9	< 0.2	< 10

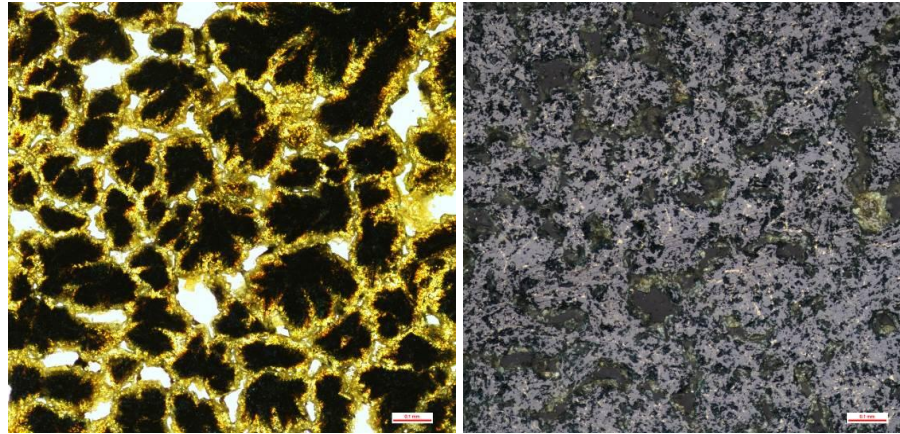
Analyte Symbol	Rb	S	Si	Sn	Tb	Tl	K	Li	Mg	Mn	Mo	Ni	Pb	V	Y	In	Pr	U
Unit Symbol	ppm	%	%	ppm	ppm	ppm	%	ppm	%	ppm								
Detection Limit	0.4	0.01	0.01	0.5	0.1	0.1	0.1	3	0.01	3	1	10	0.8	5	0.1	0.2	0.1	0.1
Analysis Method	FUS-MS-Na2O2																	
R1938-Rck-16	5.4	11.3	18.6	1.1	< 0.1	120	0.2	3	0.02	1040	122	20	1170	33	0.7	< 0.2	< 0.1	3.1
R1938-Rck-20	4.9	26.9	5.38	10.1	< 0.1	2.8	< 0.1	8	0.06	161	100	20	388	55	0.8	2.9	< 0.1	3.6
R1938-Rck-21	1.9	38.9	0.71	2	< 0.1	40	< 0.1	< 3	0.02	1430	255	20	327	42	1	12.1	0.1	3.9
R1938-Rck-22	1.1	46.3	0.82	1.3	< 0.1	14.6	< 0.1	< 3	0.05	28	207	270	102	< 5	0.1	0.9	< 0.1	0.7
R1939-Rck-13	1.7	33.8	2.47	1.5	0.2	34	< 0.1	11	0.08	5490	70	80	1380	139	6.6	16	1	2.6
R1939-Rck-14	1.8	50.9	0.09	2.7	< 0.1	8.8	< 0.1	< 3	0.01	36	513	20	115	16	0.4	2.8	< 0.1	6.5
R1940-Rck-1	6.3	8.58	3.53	1.3	0.3	15.7	0.3	15	0.33	8060	201	190	502	322	11.9	< 0.2	1.6	10.1
R1940-Rck-2	1	50.7	0.25	3.4	< 0.1	4	< 0.1	10	0.12	115	271	20	152	< 5	0.3	1.1	< 0.1	0.4
R1940-Rck-4	1.6	52.4	0.16	2.5	< 0.1	10.2	< 0.1	6	0.06	108	105	20	212	30	0.1	1.1	< 0.1	1.8
R1940-Rck-5	2.7	11.5	4.82	0.8	0.1	5.7	0.2	11	0.21	9680	144	50	1090	214	6	1	0.8	8.1
R1940-Rck-6	2.4	52.1	0.25	1.6	< 0.1	6.9	< 0.1	8	0.02	81	333	10	151	< 5	< 0.1	1.5	< 0.1	2.8
R1940-Rck-7	1.8	53.2	0.17	1.2	< 0.1	7.3	< 0.1	3	0.01	105	252	20	309	15	0.1	< 0.2	< 0.1	0.6
R1940-Rck-8	1.7	53	0.18	2.5	< 0.1	6.6	< 0.1	16	< 0.01	70	222	10	122	6	0.2	1.1	< 0.1	0.5
R1940-Rck-9	3.4	0.2	6.39	0.8	0.1	4	0.3	42	0.62	78600	142	80	225	82	7.1	< 0.2	0.4	2.6
R1941-Rck-12	1.5	49.4	0.16	1.6	< 0.1	3	< 0.1	< 3	0.01	47	276	10	22.1	12	< 0.1	3.2	< 0.1	0.6
R1941-Rck-13	0.6	53.1	0.04	1.2	< 0.1	11.4	< 0.1	< 3	< 0.01	224	357	20	542	< 5	< 0.1	0.5	< 0.1	0.3

### Appendix 3 – Detailed Petrographic Results

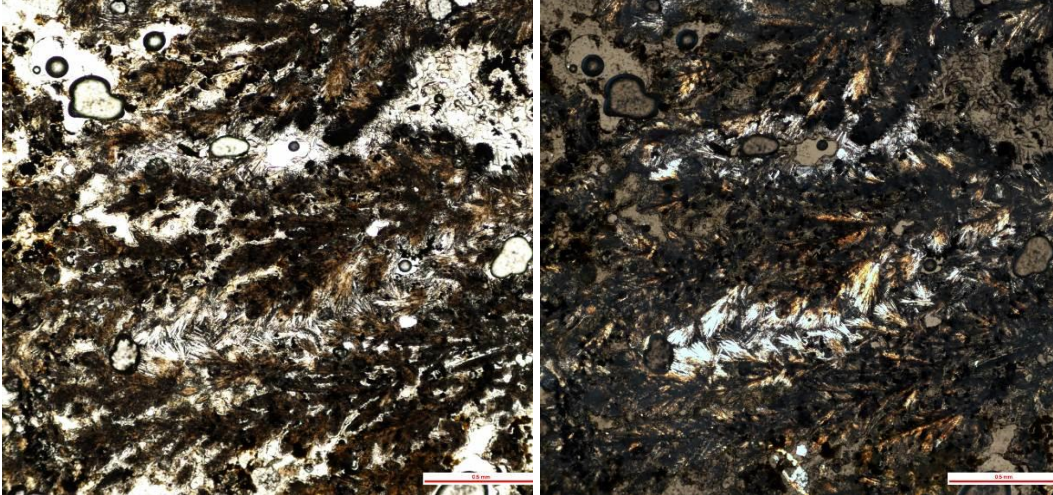
Sample Number	Sample Description
R1938-Rck-16	<p data-bbox="514 560 1856 813">There is a uniform in the distribution of mineralogy with fine-grained pyrite distributed throughout branching plumose barite developing outward towards the sample's exterior surface. Euhedral barite crystals are found as fine-grained fibers and at times coarser blades. The plumose barite texture indicates rapid precipitation. Subhedral to anhedral pyrite present usually as more of a groundmass. Oxidization at the exterior of the sample is most developed in the pore spaces around the anhydrite.</p> <div data-bbox="520 829 1451 1292">Two side-by-side photomicrographs of a rock sample. The left image shows a dense matrix of dark, fine-grained pyrite with scattered lighter-colored, branching plumose barite structures. The right image shows a similar texture but with more prominent, coarser blades of euhedral barite crystals. Both images include a small red scale bar in the bottom right corner.</div>

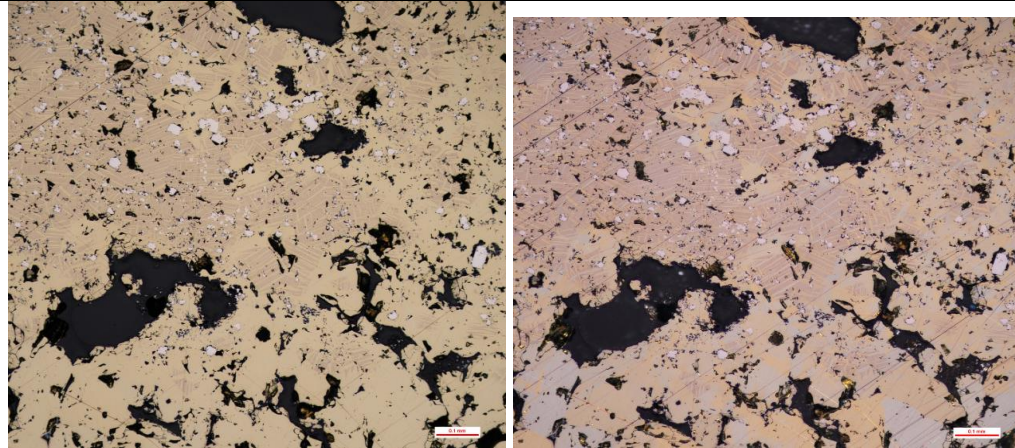
R1938-Rck-20

This sample contained an abundance of zinc sulphide and was highly porous. Chalcopyrite was disseminated throughout the massive sulphide as stringers within sphalerite.

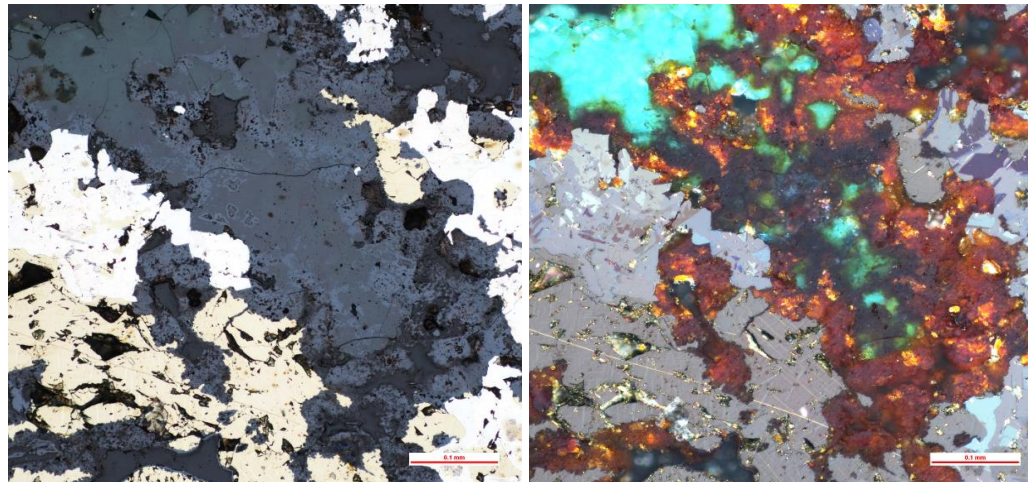


Regarding the oxidation of the overall sample, there is little overall oxidation which occurs beyond the exterior margin, but up to a depth of 3-5 mm there is near complete oxidation of the sulphide. This replacement is taking place in what appears to be a primarily replacement style of oxidation. Possible oxidation products that may be related to biogenic activity that is indicated by the circular light-dark variation patterns. Within the zone of oxidation was the sole place where trace amounts of covellite were mineralized. Amorphous Silica (15-20%) was precipitated as a late stage phase surrounding sulphide minerals.

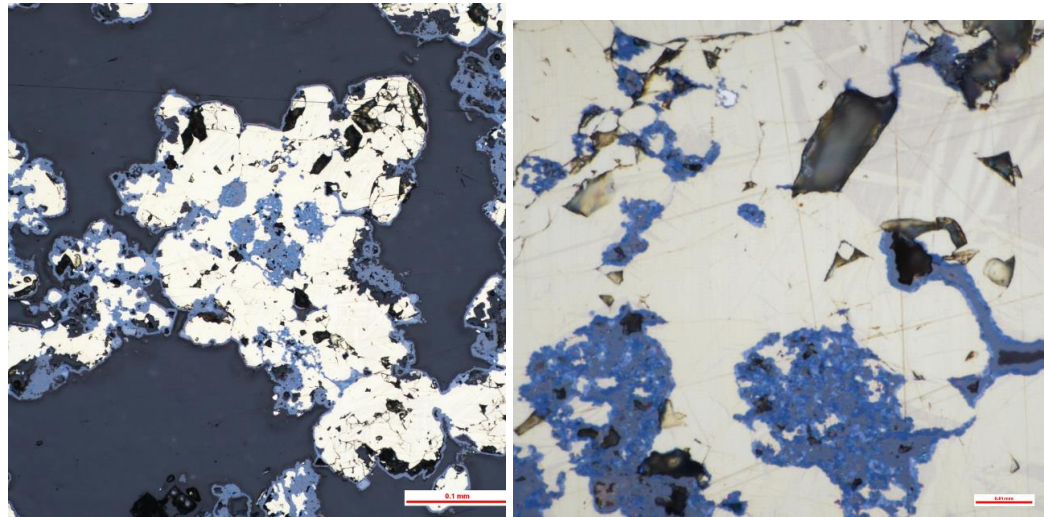
	
R1938-Rck-21	<p>Pyrite (30%) was mostly massive and is euhedral to anhedral depending on proximity to the oxidized zone. Present both on its own in zones and then as mixed sulphide as it transitions gradationally into chalcopyrite (30%) rich zones. Chalcopyrite commonly features intergrowths of isocubanite visible as striations. Marcasite was contained in minor (20%) abundance.</p>



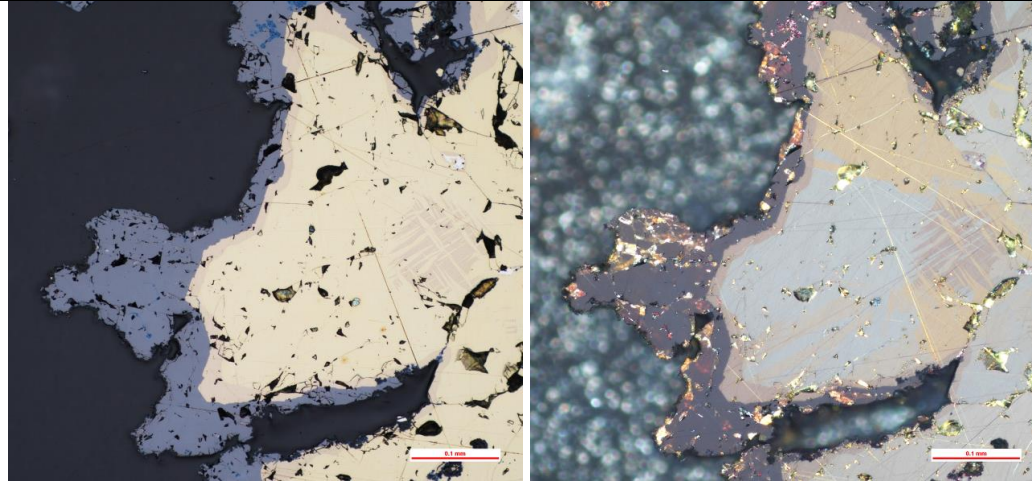
Oxidation material (15%) was commonly rimming sulphides with more pervasively oxidized areas having been replaced by amorphous oxidation material. Atacamite was contained in trace amounts as amorphous blebs, locally within the oxidation rims.



Barite and covellite were found in trace amounts, in outer margins of the sample. Fine intermixing of chalcocite with covellite in rare instances.

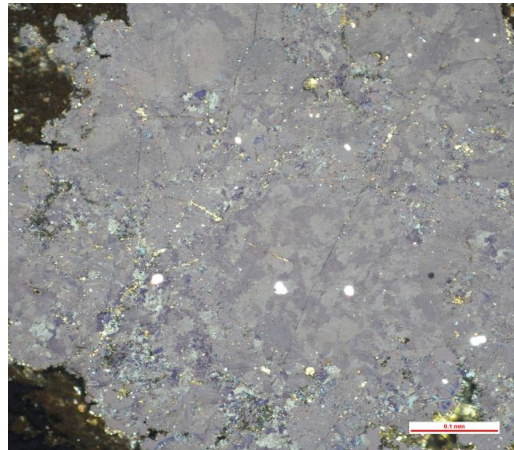


Overall, sulphides are generally massive and progress from subhedral to anhedral closer to the exterior margins. Marcasite was more often observed near portions of the sample subjected to oxidation. Significantly greater amounts of oxidation versus covellite.

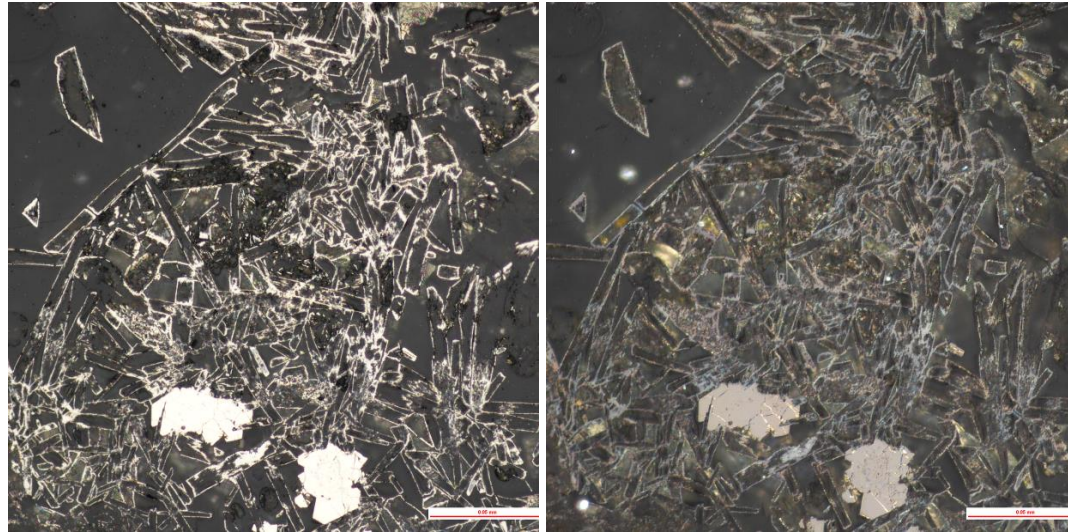


R1938-Rck-22

The section contained primarily massive, mostly subhedral with locally anhedral pyrite (40%); and massive marcasite (40%) which at times was observed forming colloform growth bands and branching dendrites which local rims of Fe-oxide. Marcasite and pyrite were often intermixed.



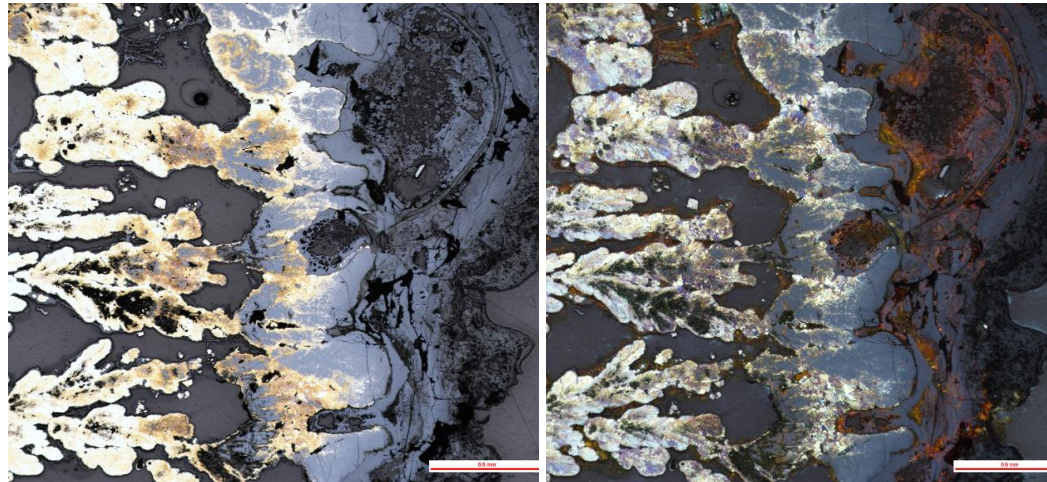
Marcasite infilling and surficial precipitation on pyrite indicate later growth. Skeletal marcasite rims a remnant Fe-oxide which was entirely replaced.



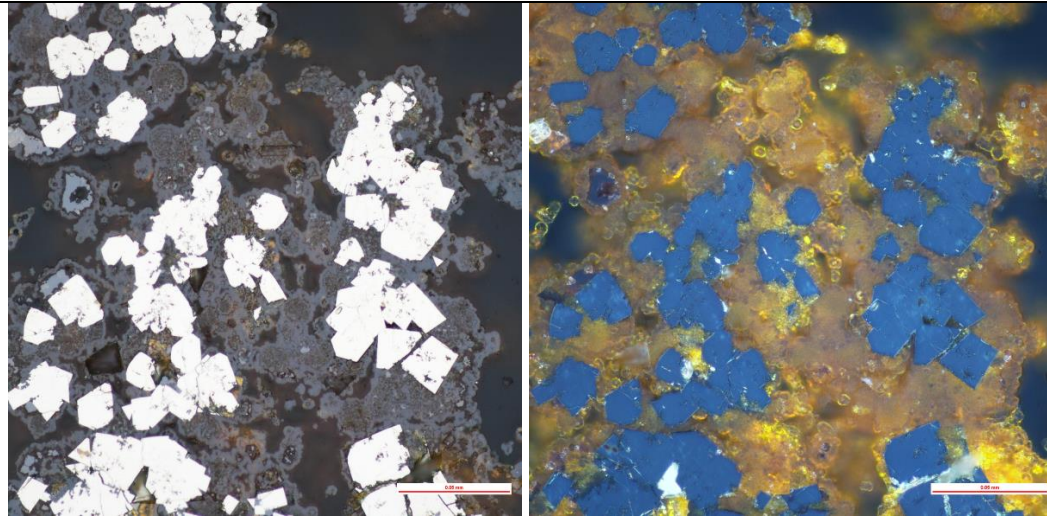
Goethite locally replaced primary massive sulphide minerals. Other oxidation commonly occurs as amorphous masses surrounding sulphide minerals. In plane-polarized reflected light it appears isotropic black-dark grey and with the cross-polarizer applied appears vibrant orange when rimming other minerals and a browner orange when replacing other minerals. Trace amounts of covellite were observed within the oxidized crust. Biologic void spaces present as indicated by large oval rims in section, likely from tube worms.

R1939-Rck-13

Marcasite was the major sulphide mineral phase present (50%), the colloform texture was common near the vent orifice, and plumose texture was present near the exterior margin due to rapid precipitation. It appeared white with yellow tarnish at times in reflected plane polarized light, in cross-polarized light, it has significant anisotropic features to distinguish it from the minor amounts of pyrite present. Goethite (40%) is featured in thin section as both vibrant amorphous orange colourless species and as darker more crystalline subhedral to anhedral pseudomorphs that in reflected cross-polarized light feature weak anisotropy (potentially remnant from replaced minerals).



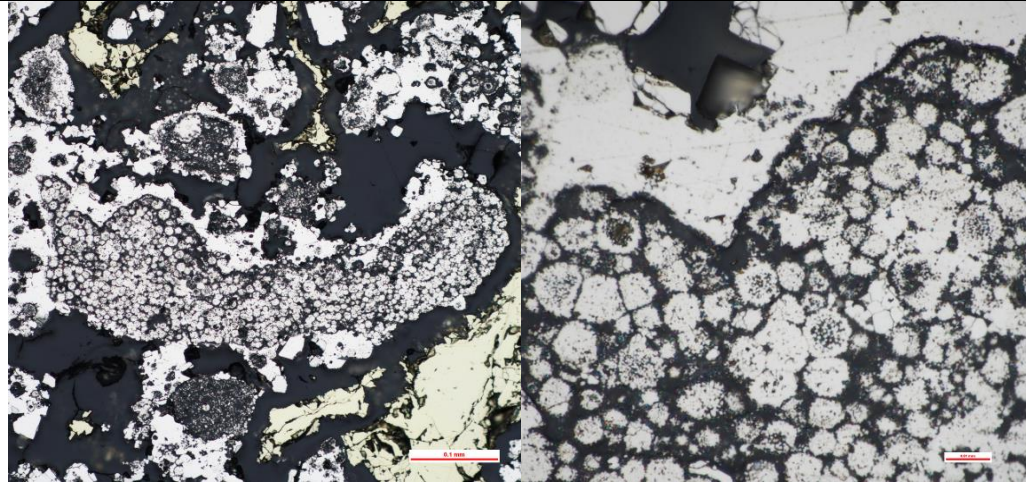
Pyrite was present in minor (5%) amounts as euhedral crystal grains despite its minor abundances overall.



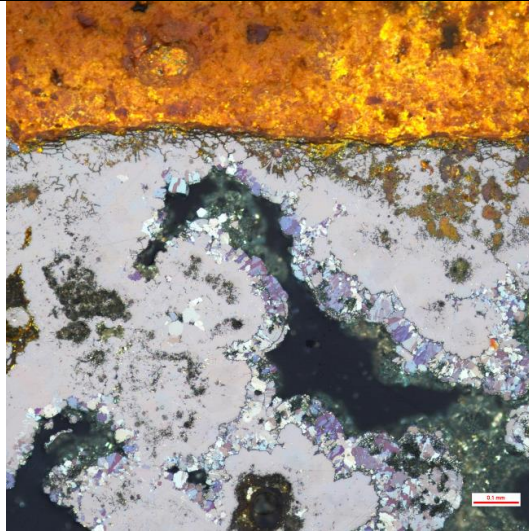
A thin ferromanganese crust could be seen in the section at the outer edge of the sample as an opaque precipitate. The other trace phase present was barite which formed elongated needle and blade crystals in the exterior margin, indicating boiling during formation. This sample is located a significant distance from the active ridgeline, implying old age, and explaining the degree of oxidation present.

R1939-Rck-14

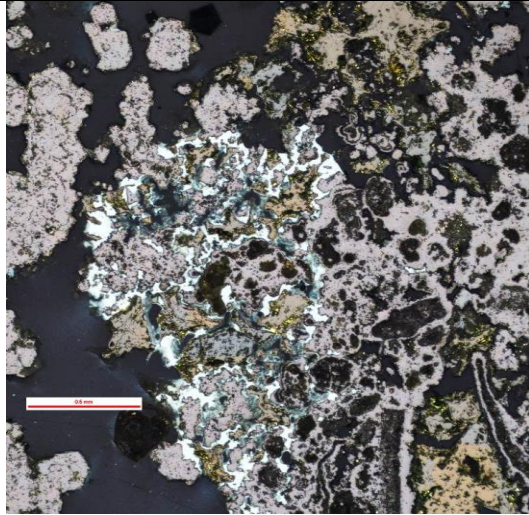
This section was made up primarily of Pyrite (70 %) ranging from euhedral to anhedral states and locally seems to be composed of fine-grained spheroids/framboids which could be related to biogenic activity.



Chalcopyrite was also abundant (20 - 25%) in subhedral to anhedral states. Minor (2-5%) amounts of marcasite were locally present. Amorphous Fe-oxide crust was overall only observed in minor abundance (5%) with a sharp contact with primary sulphide minerals.



Amorphous Fe-oxides were locally observed lining some larger pore spaces, which were abundant, and potential derived from biogenic influences. Trace amounts of amorphous silica infilling was also seen.

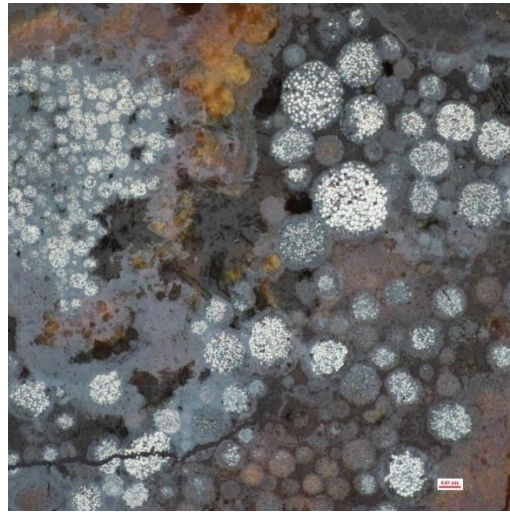


There appears to have been at least two stages of mineral growth during the active lifetime of this hydrothermal system with the initial higher temperature pyrite-chalcopyrite assemblage; a second fluid flow of lower pH resulted in the later stage marcasite rims locally at more porous portions of the sample. This sample was one of the furthest samples collected from the active venting axis of the Endeavour Segment. Despite this, this sample is not the most thoroughly oxidized even with a high degree of porosity via biologic activity. The lack of extensive oxidation is not explicitly clear, potentially indicating hydrothermal activity far off-axis or burial.

R1940-Rck-1

This section was composed nearly entirely of iron-oxyhydroxide precipitates (70%) formed due to oxidation of fine-grained sulphide minerals likely in the presence of bacteria which is discernable from

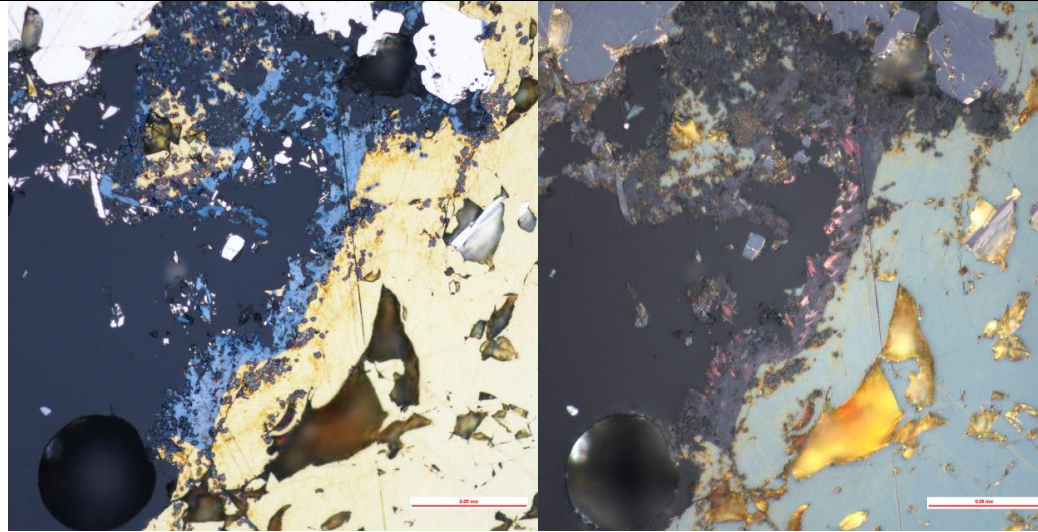
sheath and filament structures observed in thin section. It also contained minor amounts of fine to very fine-grained remnant anhedral pyrite. These pyrite grains were observed in radial framboids commonly, often with significant iron-oxide precipitates surrounding them.



This thin section was somewhat more porous than other massive sulphide samples.

R1940-Rck-2

This section contains an abundance of both massive pyrite (35-40%) which is observed from euhedral to subhedral states and massive chalcopyrite (30-35%) which was in anhedral to subhedral conditions. There was a moderate amount of pore space (10%). This sample also has minor amounts of chalcocite (10%), amorphous Fe-oxides (5%), and trace amounts of covellite.



Corrosion textures were common in chalcopyrite grains due to its tendency to preferentially oxidize. Oxidation of chalcopyrite released copper into seawater forming pale blue chalcocite, and darker blue covellite preferentially along fractures and outer grain boundaries. This appears to be an early stage massive sulphide as it was sampled near to the active vent axis. Agreeing with the little observable oxidation and the abundance of intermixed pyrite and chalcopyrite. Oxidation demonstrates its preference to occur along fractures and the outer boundaries of chalcopyrite grains.

R1940-Rck-3

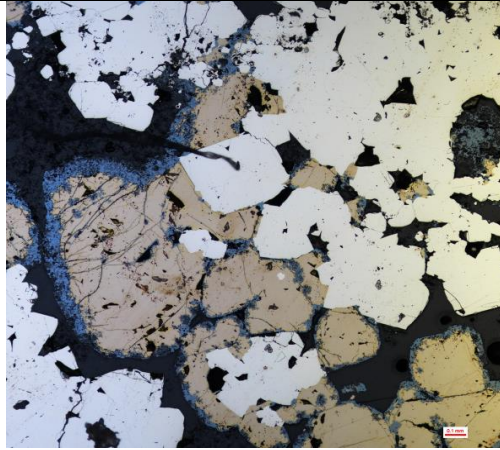
A thin section composed of fine to very fine-grained silicate minerals. Observed minerals were mostly anhedral and occasionally subhedral. Plagioclase is the dominant mineral phase (60%) with distinctive simple twinning, and pyroxene was also abundant (40%) with second order interference colours and some 90-degree cleavages.



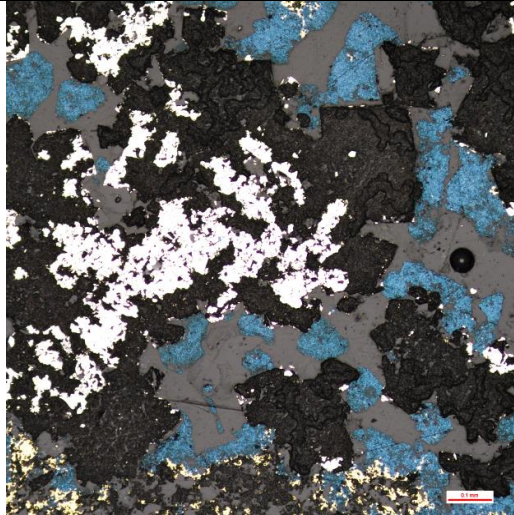
At the exterior edge of the thin section, there is an immediate textural change from fine to very fine-grained groundmass, likely due to weathering. The sample is an oceanic basalt with a thin weathering rind from seawater exposure.

R1940-Rck-4

Mineralogy is made up of predominantly massive pyrite aggregates and cubes (40-50%), anhedral covellite masses (15-20%) as determined by its blue colouration in reflected plane polarized light, and distinctive red in reflected cross-polarized light. Goethite (25-30%) replacement of pyrite during isolation and oxidation.



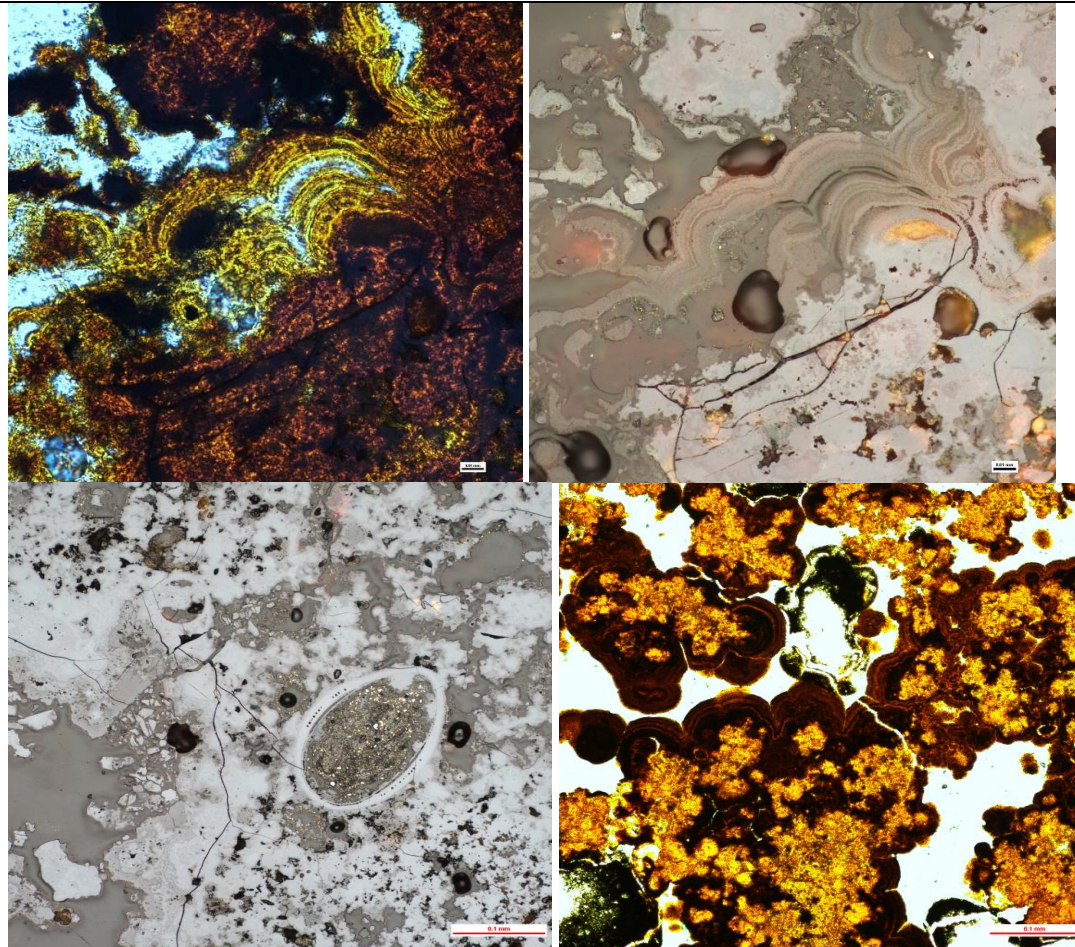
It is black in reflected light and clear-colourless in transmitted light with very high relief. Amorphous Fe-oxyhydroxide is present in minor abundance (10-15%) as a black mineral in plane polarized reflected light and translucent to red-orange mineral in plain polarized transmitted light. Other minor minerals present are chalcopyrite (< 5%) which has a characteristic yellow colouration differentiates is from pyrite as well as the more prominent birefringent colouration in cross-polarized reflected light, although most has been replaced by covellite. This section is pervasively distressed with corrosion and pitting throughout (potentially due to the cutting of the section).



Oxidation of the exterior of the sample leaves an abundance of amorphous, fine-grained Fe-oxides which incorporate trace amounts of atacamite. This thin section is an excellent example of the galvanic protection of pyrite when in contact with chalcopyrite. It was preferentially oxidized, and the Cu was subsequently incorporated into the formation of an abundance of covellite.

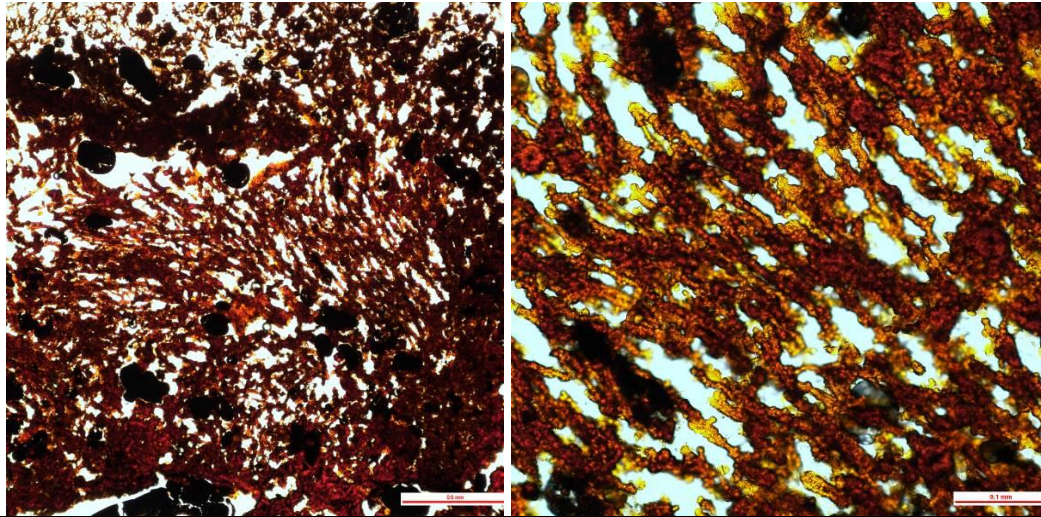
R1940-Rck-5

Most of the thin section is composed of fine-grained massive, coliform, and amorphous Fe-oxyhydroxide material (80-90%), with some pore space (10-20%), and trace amounts of the original sulphide.



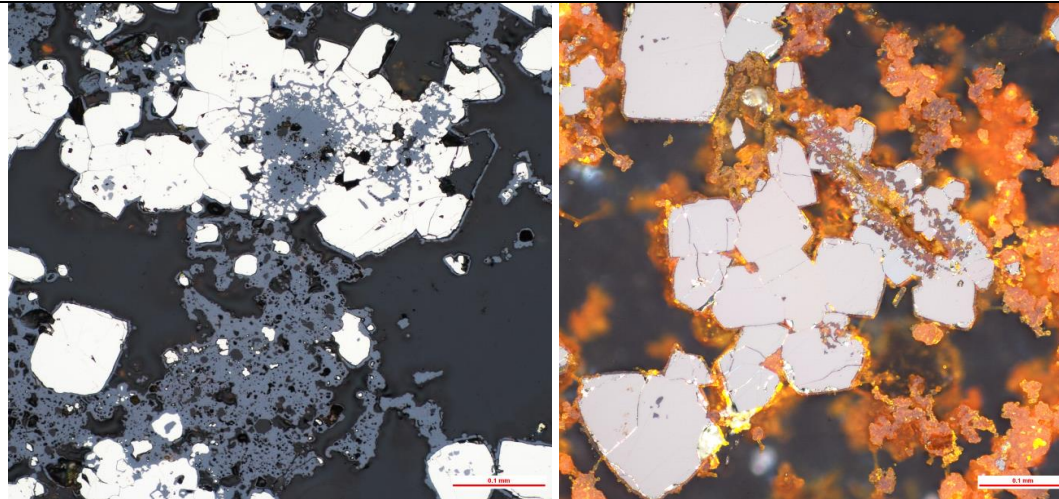
There is some variation in porosity which may be potentially due to the cut of the thin section. Local amounts of subhedral to euhedral bladed barite crystals. I have observed fossilized tube worms which allowed for the precipitation of barite and oxidised sulphide minerals along its inner lining. The sample

has undergone significant amounts of oxidation due to extended periods of seawater exposure. As a result, little of the original sulphide is present, and it is difficult at this stage to discern clear relationships between minerals. Oxidation was observed in differing precipitation processes, forming coliform banded masses as well as a network of iron-oxyhydroxides.



R1940-Rck-6

This section is uniformly fine grained and massive. Distinctive transition from outer to inner sulphide portion mostly composed of pyrite (40%) observed as euhedral to anhedral crystals depending on proximity to the exterior of sample. The other major component being Fe-oxides (40% abundance) which increases in abundance from non-existent to abundant towards the exterior of the sample.



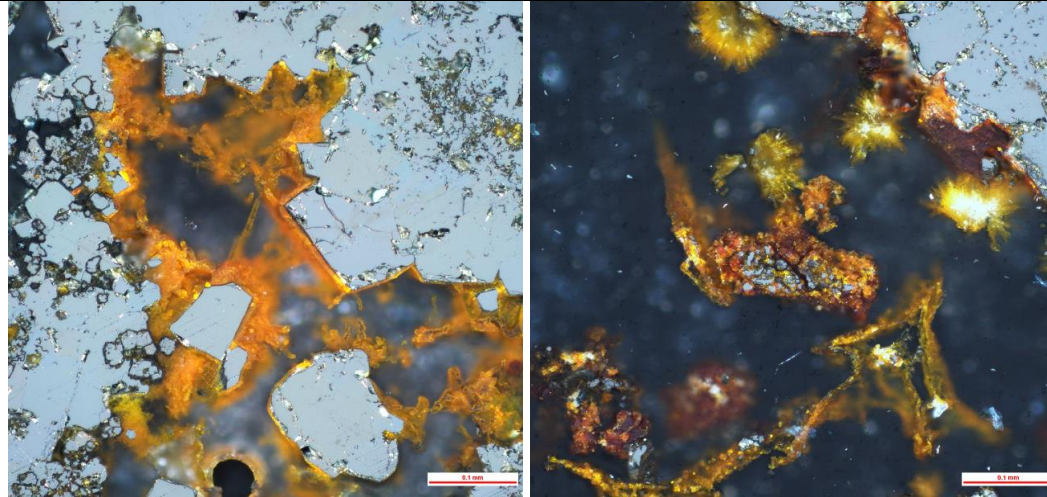
Oxide components include both amorphous Fe-oxide precipitates and replacement of primary sulphide minerals by goethite. Portions of the section with greater porosity were associated with more oxidation deeper within the sample. There was also trace amounts of chalcopyrite and rare local occurrences of amorphous silica in-filling.

R1940-Rck-7

Most of this sample is pyrite (90%) with it being characteristically massive, and generally euhedral to subhedral. Porosity was limited (5-10%) and there were no major organic related pore spaces. Other minor mineralogy observed in this sample includes trace amounts of marcasite, chalcopyrite, and sphalerite. These minor phases were found to commonly be subhedral to anhedral, found most often in pore spaces, chalcopyrite and sphalerite occurring together in some instances. There is some observable variation in colouration of sphalerite indicative of the variations in iron content.



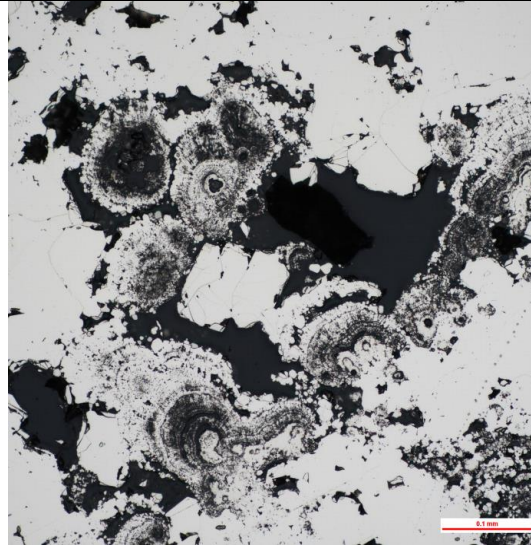
The oxidation material abundance was characteristically low within the massive sulphide (5%), potentially due to the lack of pore spaces available to support oxidation of a more surface area. Oxidation can be observed both rimming and replacing the sulphide minerals at the exterior boundary of the section.



This sample overall appears to be a monomineralic massive sulphide sample made up primarily of pyrite, collected away from the base of a chimney to infer that it would be an older, more oxidized sample. As there was a very shallow amount of oxidation occurring which was not overly friable suggested that it was not heavily oxidized. This all together supports a massive sulphide deposit composed primarily of a single sulphide resulted in a steady but generally slow oxidation of the exterior.

R1940-Rck-8

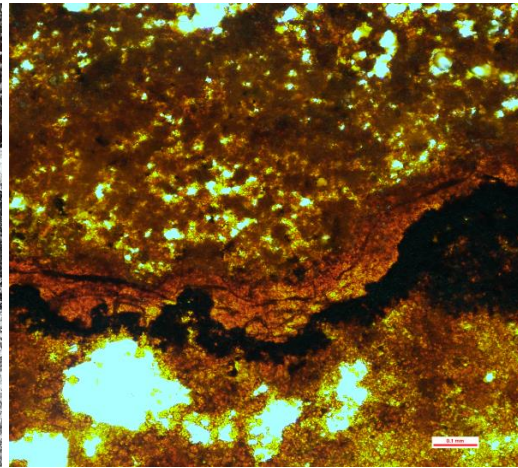
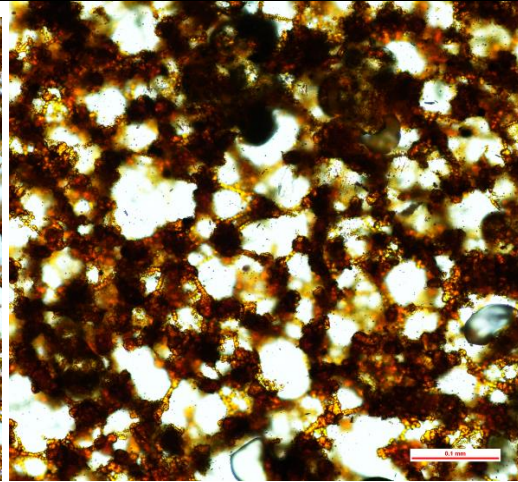
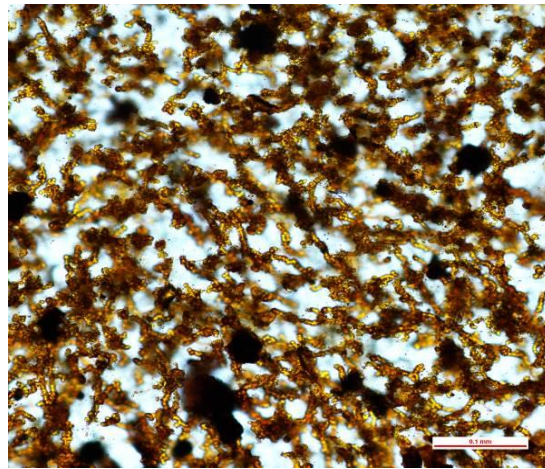
This section mineralogy was composed of almost entirely pyrite, which was in states ranging from subhedral to euhedral, and texturally varied from massive to coliform. Pyrite growths appear to have multiple generations of coarser grained cubic crystal aggregates, coliform banding of finer grained pyrite, and finer grained massive crystalline aggregates.



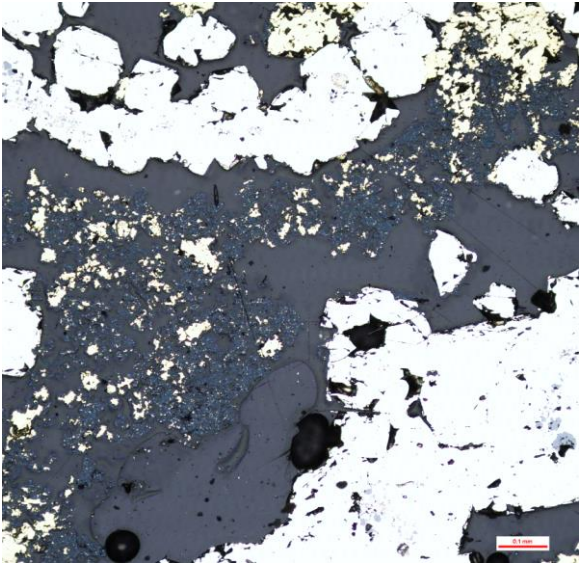
At the thin section scale porosity was a major feature making up approximately a third of the visible surface. Amorphous Fe-oxides were a minor featured primarily along the exterior of sample. Trace amounts of marcasite were also present along exterior margin of the section rimming pyrite.

R1940-Rck-9

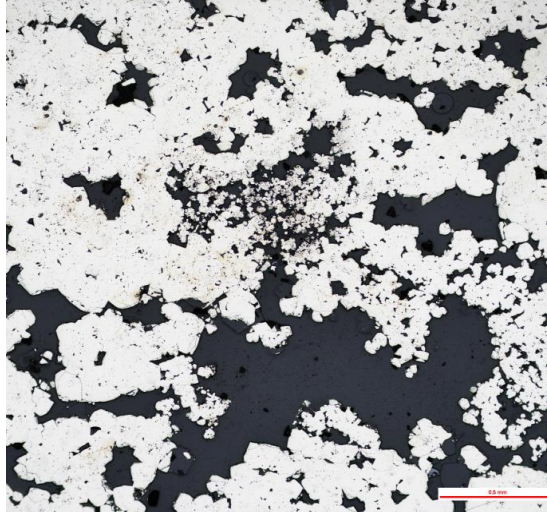
This section was cut from a heavily oxidized, highly friable fragment of nearly entirely iron-oxyhydroxide (95-99%). The Fe-oxyhydroxide composition was texturally related to biogenic activity due to the presence of bacterial filaments, and concretions which form dense networks rather than masses of amorphous Fe-oxide precipitates.



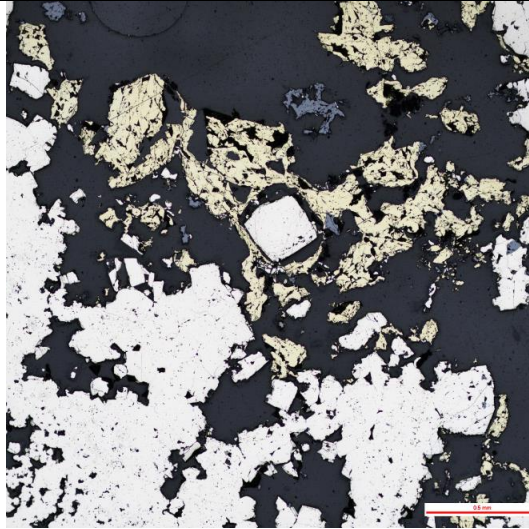
Further biologic features included fossilized tube worm structures present which seemed to have preserved the trace amounts of pyrite remaining. This sample may have originally been a massive

	<p>sulphide sample which was oxidized to near completion. This could be explained by the extensive bacterial presence having accelerated oxidation.</p>
R1941-Rck-12	<p>This section was composed primarily of subhedral to (mostly) euhedral pyrite (60%). This was likely due to galvanic protection afforded at the expense of nearby chalcopyrite which is the other prominent mineral phase (30%). Chalcopyrite was in a subhedral to anhedral state most often as it appeared to commonly be subject to preferential oxidation. The other minor phase observed in this section was covellite (5%) as a very fine grained to fine grained crystalline aggregate often rimming and replacing chalcopyrite.</p>  <p>The micrograph shows a complex mineral assemblage. Large, bright, angular grains of pyrite are visible, some with smaller, darker grains of chalcopyrite within or adjacent to them. A fine-grained, dark aggregate of covellite is also present, often rimming or replacing the chalcopyrite. A scale bar in the bottom right corner indicates 0.1 mm.</p>

	<p>Goethite was a minor (5%) phase in this section, occurring as a crystalline replacement mineral and occasionally as a light orange amorphous iron oxide precipitate. These dual oxidation styles resulted in both replacement and amorphous precipitation styles of oxidation processes being demonstrated near the outer margin of the sample. Due to the preferential oxidation of chalcopyrite, chalcopyrite rich margin segments have undergone further oxidation and produced much greater amounts of iron-oxide precipitates. This sample contained relatively little pore space (2-5%) apart from a few fluid pathways. Atacamite is present in trace amounts along the exterior margin of sample, always within the oxidation layer. Over the mineralogy of this section appears to be very similar to R1940-Rck-4 although there is significantly less covellite. The given assemblage seems to imply that this is another example of a mixed massive sulphide deposit which generated a galvanic cell and as a result there is a large contrast in the appearance of the pyrite and chalcopyrite. The difference between this sample of R1940-Rck-4 is that there is significantly less covellite, and significantly more chalcopyrite present. This could be due to there being significantly more chalcopyrite present in this sample, or that this sample has been exposed and oxidized for a shorter period and as such has not progressed as far along the oxidation reaction chain.</p>
R1941-Rck-13	<p>This section was composed of predominantly coarse-grained sulphide minerals. Of which, pyrite precipitated over two generations of coarse-grained euhedral crystals and fine-grained dendritic aggregates was the most abundant (50%).</p>



Chalcopyrite was abundant to a lesser degree than pyrite (20%) and appeared to be unreactive with either pyrite or sphalerite, which often were in proximity. Chalcopyrite ranges from subhedral to anhedral but is most often subhedral. Sphalerite was roughly equally abundant as chalcopyrite (20%) generally composed of dark (Fe rich) cores and light (Fe poor) rims.

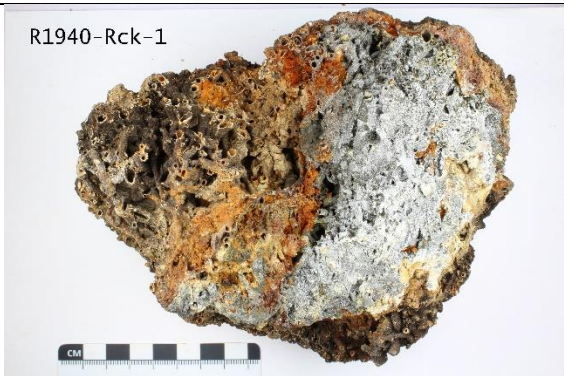


Sphalerite was subhedral and commonly occurs in proximity or is intergrown with chalcopyrite, but it did not appear that sphalerite and chalcopyrite interactions resulted in any preferential oxidation. However, there were several examples of chalcopyrite disease observed in this section. This sample was relatively low in porosity.

## Appendix 4 – Hand sample Descriptions

Sample ID	Hand sample Description	Image
R1938-Rck-16	<p>This hand sample was composed of two pieces of fine-grained massive sulphide ranging in size from 19 to 13 cm and 11 to 8 cm. Both sample fragments appear light to dark grey on fresh surfaces and black to light orange on weathered and oxidized surfaces. Oxidation surface rinds were approximately 1mm thick. Both fragments demonstrated a limited amount of porosity.</p>	 <p>R1938-Rck-16</p>
R1938-Rck-20	<p>A single large hand sample (24 by 10 cm) with fresh surfaces appearing light to dark grey in colour, with an oxidation rind of approximately 2mm thickness along the outer margin in some instances. This sample was massive and appeared to primarily be composed of very fine-grained sulphide minerals.</p>	 <p>R1938-Rck-20</p>

R1938-Rck-21	Composed of 3 sample samples of approximately 9 by 4.5 cm size which broke down into many small fragments. The interior fresh surface of these samples was black with light orange exterior surface coatings ranging from 1 to 2 mm in thickness. This sample was composed primarily of massive sulphide minerals, and an abundance of vesicles.	
R1938-Rck-22	This sample was composed of four large pieces ranging in size from 24 by 18 cm to 10 by 7.5 cm. All samples fragments were generally dark grey in colour with sporadic oxidation patches on some exterior surfaces. Mineralogy was generally fine-grained massive sulphides with local grain size coarsening adjacent to pore spaces inferred to be hydrothermal fluid conduits.	
R1939-Rck-13	This hand sample is made up of two pieces measuring 9 by 5 cm and 6 by 5 cm, respectively. Both are composed of very fine-grained massive sulphide, appearing dark grey to black on fresh surfaces. Both sample fragments feature little to surficial oxidation.	

R1939-Rck-14	A single large hand sample (25 by 18 cm) composed of fine-grained massive sulphide minerals. The exterior surface is encrusted by both a thin (1 mm) oxidation rind in addition to an abundance of tubeworm remains. These tubeworms are also observed within the interior of the hand sample, although, in less abundance.	 <p>R1939-Rck-14</p>
R1940-Rck-1	Multiple medium to small samples (11 by 14, 11 by 9, 7 by 7, and 5 by 4 cm) composed of a cemented aggregate of fossilized tubeworms. This sample is mostly light grey fine-grained sulphide particles and extremely porous due to the empty space within the tubes. The external oxidization crust is approximately 1mm thick and ranges from dark brown to light orange.	 <p>R1940-Rck-1</p>
R1940-Rck-2	Single fine-grained massive sulphide sample (11 by 9.5 cm). It has a dark grey exterior and orange oxidized surfaces which are approximately 1mm thick.	 <p>R1940-Rck-2</p>

R1940-Rck-3	<p>Two basaltic samples composed of fine-grained minerals. The outer rind of these samples is generally unoxidized but do display some colouration changes due to weathering.</p>	
R1940-Rck-4	<p>Single large (21 by 15 cm) massive sulphide sample composed of very fine-grained light grey minerals. The exterior surface of the sample is mostly oxidized and ranges in colouration from brown, red-orange, to deep red and ranges from 1 to 2 mm in thickness.</p>	
R1940-Rck-5	<p>Several pervasively oxidized sample fragments (6.5x5.5, 5x4, and 4.5x3cm). These samples are dark orange to black, with some patches of light grey. Some textural features are visible in the hand sample, this includes some tubeworms and glassy veinlets.</p>	

<p>R1940-Rck-6</p>	<p>A single fine-grained massive sulphide sample (11 by 6 cm). This sample appears to be dark grey on fresh surfaces and features an orange oxidized exterior of 1 to 2 mm in thickness.</p>	<p>R1940-Rck-6</p> 
<p>R1940-Rck-7</p>	<p>A single fine-grained massive sulphide sample (12 x 6.5 cm). Well oxidized with an oxidation rind of approximately 1mm thickness, oxidation is of a red-orange colouration.</p>	<p>R1940-Rck-7</p> 
<p>R1940-Rck-8</p>	<p>Composed of two large fine to very fine massive sulphide samples (17 x 14 and 30 x 17 cm). Both samples are encrusted by millimetre thick red-range oxidation crust. Fresh sulphide surfaces appear light grey to black. Some remnant tubeworm structures are observed.</p>	<p>R1940-Rck-8</p> 

R1940-Rck-9	A single friable sample (7 x 4 cm) which appears light orange to dark brown. The sample appears to be entirely oxidized and no distinctive mineralogy is observable.	
R1941-Rck-12	Composed of two large fine to very fine massive sulphide samples (15 x 10 and 14 x 11 cm). Both samples are encrusted by thick red-range oxidation crusts of approximately two millimeters in thickness. Sample contains void spaces typically with a diameter of three millimetres.	
R1941-Rck-13	Single massive sulphide sample (9 x 7 cm) with a red-orange oxidized crust one millimetre thick.	